Differential requirements for mitochondrial electron transport chain components in the adult murine liver.

Nicholas P. Lesner[1], Xun Wang[1], Zhenkang Chen[1], Anderson Frank[2], Cameron Menezes[1], Sara House[1], Spencer D. Shelton[1], David G. McFadden[2,3], Janaka Wansapura[4], Ralph J. DeBerardinis[1,3,5,6], Prashant Mishra[1,3,5]

[1]Children's Medical Center Research Institute, University of Texas Southwestern Medical Center, Dallas, TX 75390.

[2]Department of Biochemistry, University of Texas Southwestern Medical Center, Dallas, TX 75390.

[3]Harold C. Simmons Comprehensive Cancer Center, University of Texas Southwestern Medical Center, Dallas, TX 75390.

[4]Advanced Imaging Research Center, University of Texas Southwestern Medical Center, Dallas, TX 75390.

[5]Department of Pediatrics, University of Texas Southwestern Medical Center, Dallas, TX 75390.

[6]Howard Hughes Medical Institute, University of Texas Southwestern Medical Center, Dallas, TX 75390.

*Correspondence to: prashant.mishra@utsouthwestern.edu

Summary

Mitochondrial electron transport chain (ETC) dysfunction due to mutations in the nuclear or mitochondrial genome is a common cause of metabolic disease in humans, and displays striking tissue specificity depending on the affected gene. The mechanisms underlying tissue specific phenotypes are not understood. Complex I (cI) is classically considered the entry point for electrons into the ETC, and *in vitro* experiments indicate that cI is required for basal respiration and maintenance of the NAD^+/NADH ratio, an indicator of cellular redox status. This finding has largely not been tested *in vivo.* Here, we report that mitochondrial complex I (cI) is dispensable for homeostasis of the adult mouse liver; animals with hepatocyte-specific loss of cI function display no overt phenotypes or signs of liver damage, and maintain liver function, redox and oxygen status. Further analysis of cI-deficient livers did not reveal significant proteomic or metabolic changes, indicating little to no compensation is required in the setting of complex I loss. In contrast, complex IV (cIV) dysfunction in adult hepatocytes results in decreased liver function, impaired oxygen handling, steatosis, and liver damage, accompanied by significant metabolomic and proteomic perturbations. Metabolomic analysis suggests that the electron transfer flavoprotein complex constitutes a major route for electron entry into the hepatic ETC. Our results support a model whereby complex I loss is tolerated in the mouse liver because hepatocytes use alternative electron donors to fuel the mitochondrial ETC.

53 **Introduction**

54 Mitochondrial ETC disease in humans exhibits a striking tissue specificity, whereby
55 mutations in distinct ETC components are causative for specific and non-overlapping
56 syndromes (*1*). As an example, genetic dysfunction of mitochondrial complex I (cI) is
57 associated with neurological disease including Leigh syndrome (characterized by severe
58 loss of motor abilities, necrotizing brain lesions and early death), and Leber Hereditary
59 Optic Neuropathy (characterized by bilateral loss of vision in early adulthood due to
60 degeneration of the optic nerve) (*2-4*). The mechanisms underlying sensitivity of the
61 nervous system, with sparing of other organ systems, in the setting of complex I loss is
62 not understood. In contrast, mutations in other mitochondrial ETC components have been
63 associated with multi-organ diseases, and the basis for tissue specificity in those diseases
64 is also unclear (*5*).

65 Liver involvement is a common component of mitochondrial diseases, present in
66 approximately 20% of patients (*6, 7*), as well as being associated with specific syndromes
67 caused by mutations in distinct ETC-related components (*8-12*). Common findings in
68 affected patients include hepatomegaly, steatosis, cholestasis and additional metabolic
69 abnormalities associated with liver failure (*12-15*). Genetic analysis of patients has
70 revealed mutations in genes which influence multiple components of the ETC (e.g.,
71 *POLG*, *LARS*, *DGUOK*) (*10*). With respect to single-complex diseases, mutations in
72 *SCO1*, an assembly protein for mitochondrial complex IV (cIV), and mutations in *BCS1L*,
73 a chaperone protein for mitochondrial complex III, have been associated with liver failure
74 (*8, 16, 17*). Interestingly, single-complex diseases associated with other components of

75 the ETC (complex I and complex II) do not typically present with liver failure, despite their
76 placement directly upstream of cIV.

77 The ETC functions to transfer electrons (from the oxidation of nutrients) to O_2, as
78 a final electron acceptor; this process is coupled to the formation of an electrochemical
79 gradient across the mitochondrial inner membrane and the production of ATP.
80 Mitochondrial complex I is the largest protein complex of the ETC, and is commonly
81 considered the primary entry point for electrons into the ETC: In cultured cells, cI is
82 required for maintenance of cellular redox status (assessed by the NAD^+/NADH ratio) via
83 its role in NADH oxidation, and subsequent electron transfer to ubiquinone (CoQ) (*18*).
84 Complex I is composed of 14 core subunits, plus an additional 31 accessory subunits
85 (*19*). Published mouse models of complex I deficiency have largely focused on accessory
86 subunits, including deletion of *Ndufs4*, *Ndufs6*, and *Ndufa5*, which result in neurological
87 and cardiac phenotypes associated with partial loss of complex I function (*20-22*); no liver
88 phenotypes or metabolic perturbations were reported in these mice (*23*). A recent report
89 conditionally deleted *Ndufs3*, a core subunit of cI, in skeletal muscle, resulting in
90 progressive myopathy associated with significant reduction of cI activity (*24*). Thus, to
91 date, mouse models have supported an essential role for cI *in vivo* in the central nervous
92 system and muscle.

93 Here, we report that deletion of the core subunit, *Ndufa9*, results in complete loss
94 of cI function, but is well-tolerated in the adult mouse liver. Further analysis reveals intact
95 liver function and oxygen status in *ndufa9*$^{-/-}$ animals, which is not accompanied by
96 significant metabolic alterations or changes in redox status. This is in contrast with
97 hepatocyte-specific deletion of the complex IV assembly factor *cox10,* which results in

altered redox status and impaired liver function. In complex IV-depleted livers, we observe the accumulation of long chain acyl-carnitine species, without significant alterations in other potential electron donors, suggesting that fatty acids are a major electron donor to the hepatic ETC. These results support a model in which cI is not an essential upstream component of the ETC in adult mammalian liver, in contrast to the conventional view of cI function.

122 **Results**

123 **Mitochondrial complex I function is dispensable for homeostasis of adult murine**
124 **hepatocytes**

125 To understand how liver cells respond to loss of complex I, we made use of a conditional
126 allele of the core subunit *Ndufa9*. *ndufa9* deletion in cultured mouse embryonic fibroblasts
127 results in loss of mitochondrial respiratory function, as well as a significant drop in the
128 NAD^+/NADH ratio (Figure 1 – figure supplement 1A,B), indicating that Ndufa9 is critical
129 for redox status in these cultured cells. We depleted *Ndufa9* in livers of adult mice, making
130 use of adeno-associated virus 8 (AAV8)-mediated Cre recombination driven by the liver
131 specific TBG promoter in *ndufa9*$^{flox/flox}$ animals (see Methods). *ndufa9*$^{flox/flox}$ adult animals
132 were injected with control AAV8-GFP virus (hereafter "*ndufa9*$^{f/f}$") or AAV8-Cre virus
133 (hereafter "*ndufa9*$^{-/-}$"). At 4 weeks post-AAV administration, AAV-Cre injected animals
134 exhibited loss of Ndufa9 mRNA and protein in hepatocytes (Figure 1A,B), as well as loss
135 of complex I activity in mitochondrial lysates (Figure 1C). Thus, our experimental model
136 results in severe inhibition of complex I function.

137 At 4 weeks post-AAV administration, *ndufa9*$^{-/-}$ livers displayed no differences in
138 gross physiology (Figure 1D) or liver/body weight ratio (Figure 1F). Histological analysis
139 of liver sections revealed no significant pathology (H&E), including no evidence of
140 steatosis (Oil Red O staining) or glycogen loss (PAS staining) (Figure 1E). Liver function
141 was maintained in *ndufa9*$^{-/-}$ livers as indicated by unaltered levels of fasting blood glucose
142 (Figure 1G) and circulating indicators of liver function and damage (Figure 1H,I). Similar
143 results were observed in mice at two weeks post-AAV injection (Figure 1 – figure
144 supplement 2) and eight weeks post-AAV injection (Figure 1 – figure supplement 3). Thus,

145 complex I loss is well-tolerated in adult mouse hepatocytes under homeostatic conditions,
146 with no discernable effects on tissue function, or evidence of tissue damage.

147 Measurement of steady-state ATP levels did not reveal any changes in complex I
148 deficient livers (Figure 2A). Complex I inhibition is often associated with elevated reactive
149 oxygen species (*25, 26*). In *ndufa9*$^{-/-}$ livers, we observed a small, but not statistically
150 significant, decrease in the reduced to oxidized glutathione (GSH / GSSG) ratio, indicating
151 that oxidative stress is not significantly induced in the setting of cI loss (Figure 2B).
152 Surprisingly, we did not observe altered NAD^+/NADH or NADPH/$NADP^+$ ratios in *ndufa9*$^{-}$
153 $^{/-}$ liver (Figure 2C). We additionally examined compartment specific redox status by
154 calculating pyruvate / lactate and acetoacetate / β-hydroxybutyrate ratios, which are
155 indicative of cytosolic and mitochondrial redox status respectively; neither compartment
156 display evidence of altered redox status (Figure 2D). A recent report suggests that
157 circulating α-hydroxybutyrate levels serves as a marker of hepatic redox stress (*27*).
158 *ndufa9*$^{-/-}$ animals did not display alterations in tissue or plasma α-hydroxybutyrate levels
159 (Figure 2E). Thus, complex I function is not required for maintenance of hepatic redox
160 status, in contrast to its well-established role in cultured cells (Figure 1 – figure
161 supplement 1A,B) (*18*).

162 To examine potential compensatory mechanisms that may be enabled in the
163 setting of complex I inhibition, we assessed changes in the proteome and metabolome,
164 comparing *ndufa9*$^{f/f}$ and *ndufa9*$^{-/-}$ whole livers. At four weeks post-AAV, our proteomics
165 analysis detected 3001 proteins with high confidence; however, only 11 proteins were
166 significantly upregulated ($\log_2$(fold change) > 1, p-val < 0.05), and 23 proteins were
167 significantly downregulated ($\log_2$(fold change) < -1; p-val < 0.05) (Table S1).

168 Unsupervised hierarchical clustering was unable to distinguish proteomes from *ndufa9*$^{f/f}$
169 and *ndufa9*$^{-/-}$ livers (Figure 2F). Of the downregulated proteins, the majority were
170 components of complex I (Figure 2G,H; Table S1), consistent with destabilization of cI in
171 the setting of *Ndufa9* subunit loss. We did not observe loss of components from other
172 ETC complexes (Figure 2H). Among upregulated proteins, there were a small number of
173 mitochondrial proteins impacting translation (Mrpl52, Mrpl42), electron transport
174 (Cox6a1) and metabolism (Shmt2, Ldhd, Dlat) (Figure 2G; Table S1). The small number
175 of abundance changes (outside of complex I components) suggests that the proteome is
176 not drastically changing in response to complex I loss; however, our analysis is only
177 sampling a portion of the total cellular proteome, and it is possible that we are missing
178 some key regulatory proteins in reaction to complex I loss. To further profile the response
179 in *ndufa9*$^{-/-}$ livers, we enriched liver lysates for mitochondrial fractions followed by
180 proteomics (Figure 2 – figure supplement 1). With this method, we were able to detect
181 738 mitochondrial proteins, which accounts for ~64% of the total mitochondrial proteome
182 (Table S1). We observed significant changes ($|\log_2(\text{fold change})| > 1$, Adjusted p-val <
183 0.05) in only a small fraction of the mitochondrial proteome (46 proteins; ~6% of detected
184 mitochondrial proteins) (Figure 2 – figure supplement 1A). Complex I subunits tended to
185 be decreased in abundance, and we did not observe significant changes in most subunits
186 of the other complexes (Figure 2 – figure supplement 1B). We observed statistically
187 significant upregulation of some select components of mitochondrial protein import
188 (TOMM5, TIMM9, TIMM10B) and transcription/translation (MRPS33, MTRES1) (Figure 2
189 – figure supplement 1A). In addition, we did not detect significant changes in total
190 mitochondrial content in *ndufa9*$^{-/-}$ livers, as indicated by measurement of mitochondrial

191 genome and protein content or immunofluorescence (Figure 2I-K, Figure 2 – figure
192 supplement 2).

193 We next assessed whether complex I – deficient livers maintained functionality via
194 metabolic compensatory mechanisms, and therefore quantitated the liver metabolome of
195 fasted mice, using LC/Q-TOF mass spectrometry based metabolomics to measure
196 steady-state levels of >150 tissue (liver) metabolites at four weeks post-AAV (Table S1).
197 Unsupervised hierarchical clustering was unable to distinguish metabolomes between
198 *ndufa9*$^{f/f}$ and *ndufa9*$^{-/-}$ livers (Figure 2L), and statistical analysis revealed only a single
199 significant metabolite difference (TMP, thiamine monophosphate) (Figure 2M, Table S1),
200 and no significant changes in mitochondrial TCA cycle metabolites (Figure 2N). The
201 rationale for the observed increase in TMP is currently unclear, but may be related to a
202 reduced need for thiamine pyrophosphate which is a cofactor for NAD(H)-linked
203 dehydrogenases.

204 In culture, complex I is required for recycling of NADH to NAD^+ in order to maintain
205 glycolytic and TCA cycle activity (*28*). We therefore assessed glucose contribution to
206 glycolytic and TCA cycle metabolites via steady-state euglycemic infusions of [U-
207 ^{13}C]glucose (Figure 3A,B). A schematic of the expected labeling pattern is shown in
208 Figure 3A. We observed no significant differences in the hepatic enrichment of labeled
209 glucose between wild-type and *ndufa9*$^{-/-}$ livers (Figure 3C). In addition, contribution of
210 glucose-derived carbons to glycolytic and TCA cycle intermediates were unaltered
211 (Figure 3 – figure supplement 1A), indicating no substantial changes in glucose handling.
212 As labeling from glucose can be significantly scrambled *in vivo* and livers exhibit low PDH

213 (pyruvate dehydrogenase) activity (*29, 30*), we also assessed total enrichment (e.g., 1-
214 (m+0)), which revealed no significant differences (Figure 3D).

215 In the conventional view of the mitochondrial ETC, electrons from NADH are
216 transferred via complex I to drive coenzyme Q reduction and O_2 consumption via
217 complexes III and IV (Figure 3A). In cultured cells, complex I is the major route of electron
218 entry into the ETC, and inhibition of complex I dramatically lowers cellular oxygen
219 consumption (Figure 1 – figure supplement 1A). Our above results suggest this scenario
220 may not be true during hepatic homeostasis. We therefore made use of magnetic
221 resonance imaging (MRI) to assess blood and tissue oxygenation *in vivo*. *ndufa9*$^{f/f}$ and
222 *ndufa9*$^{-/-}$ littermates were challenged with room air, followed by 100% oxygen, and T1 and
223 T2* relaxation parameters were sequentially assessed (Figure 3E). Based on arterial spin
224 labeling (*31*), we did not observe changes in liver perfusion between the two genotypes
225 (Figure 3F). BOLD (Blood-oxygen-level dependent) measurements (T2*) are dependent
226 on the concentration of deoxyhemoglobin (*32, 33*), and we observed significant increases
227 in T2* in both *ndufa9*$^{f/f}$ and *ndufa9*$^{-/-}$ animals, indicating increased blood oxygen in the
228 setting of 100% O_2 (Figure 3G). TOLD (Tissue-oxygen-level dependent) measurements
229 (based on T1 relaxation) are dependent on the dissolved oxygen concentration; with
230 increased tissue oxygen content, T1 parameters are expected to decrease (*34*). In wild-
231 type livers, we observed no significant decreases in the average hepatic T1 in response
232 to 100% O_2 (Figure 3H,I,J), consistent with previous measurements in human livers (*35*).
233 This suggests that when challenged with increased blood O_2 delivery, wild-type mouse
234 liver is able to compensate and maintain steady O_2 levels, potentially through increased
235 tissue oxygen consumption. Similar to *ndufa9*$^{f/f}$ livers, *ndufa9*$^{-/-}$ livers also did not exhibit

236 significant decreases in the average T1 parameter, indicating that tissue oxygen levels
237 are maintained in the absence of complex I function (Figure 3H-J). We also assessed T1
238 changes locally by aligning images (ΔT1); as above, we did not observe significant
239 decreases in the average ΔT1 in either *ndufa9*$^{f/f}$ or *ndufa9*$^{-/-}$ livers (Figure 3K). Thus,
240 based on tissue oxygen levels in response to a hyperoxic challenge, *ndufa9*$^{-/-}$ livers do
241 not have a measurable change in oxygen consumption as compared with wild-type livers.
242 Altogether, the above results indicate that complex I is largely dispensable for oxygen
243 status and homeostatic function in the adult mouse liver, without signs of significant
244 metabolic or proteomic compensation.
245
246 **Mitochondrial complex IV is required in adult hepatocytes.**
247 To further explore a role for the mitochondrial ETC, we examined the requirement for
248 complex IV, making use of a *cox10*^{flox} allele (*36*). *Cox10* is an assembly factor of complex
249 IV, and *cox10* deletion in skeletal muscle is associated with diminished cIV activity
250 accompanied by myopathy (*36*). A previous report utilizing this allele in combination with
251 the liver-specific Albumin-Cre transgenic reporter revealed partially penetrant phenotypes
252 dependent on the transgene dosage (*37*), suggesting that the mitochondrial ETC is
253 required for liver development. Thus, we made use of AAV-delivery of Cre recombinase
254 to *cox10*$^{f/f}$ animals to investigate its role in the adult liver. Similar to above, we injected
255 *cox10*$^{f/f}$ animals with AAV-GFP or AAV-Cre and characterized liver physiology at 4 and 8
256 weeks post-injection. At 4 weeks post-injection, AAV-Cre injected animals (hereafter,
257 "*cox10*$^{-/-}$") demonstrated significant reductions in Cox10 mRNA and protein (Figure 4A,B)
258 and complex IV activity (Figure 4C). By 8 weeks post-AAV administration, *cox10*$^{-/-}$ livers

259 were grossly enlarged and pale in color, as compared with wild-type livers (Figure 4D,F).
260 Histological analysis of liver sections revealed signs of lipid accumulation indicating
261 hepatic steatosis (Oil Red O staining), as well as decreased glycogen accumulation (PAS
262 staining) (Figure 4E). Fasting glucose levels were decreased in animals with *cox10*$^{-/-}$
263 livers (Figure 4G). To directly probe gluconeogenesis, fasted mice were challenged with
264 a [U-^{13}C]-lactate/pyruvate tolerance test; animals with *cox10*$^{-/-}$ livers were unresponsive
265 as compared with wild-type animals (Figure 4H,I, Figure 4 – figure supplement 1A).
266 Additional plasma indicators of liver function were diminished in *cox10*$^{-/-}$ animals,
267 including decreased plasma total protein and increased plasma bilirubin (Figure 4J). We
268 also observed significant elevations in ALT and AST, indicators of liver damage (Figure
269 4K). Thus, in contrast to loss of complex I, the loss of complex IV in adult hepatocytes is
270 associated with hepatic steatosis, diminished liver function and evidence of liver damage.
271 Despite the fatty livers and diminished function, *cox10*$^{-/-}$ animals exhibited no
272 survival deficits even 8 weeks after AAV administration, and we did not detect changes
273 in steady state ATP levels in liver tissue (Figure 5A). *cox10*$^{-/-}$ livers exhibited a small,
274 but not statistically significant, trend towards increased oxidative stress (lowering of the
275 GSH / GSSG ratio) (Figure 5B). In contrast to cI-deficient livers, cIV deficiency
276 significantly impacted the redox status of the cell, as measured by the NAD^+ / NADH ratio
277 (Figure 5C). We observed altered ratios of both pyruvate / lactate and acetoacetate / β-
278 hydroxybutyrate, indicating impaired redox status in both the cytosol and mitochondrial
279 compartments (Figure 5D). Interestingly, tissue α-hydroxybutyrate levels were decreased
280 in *cox10*$^{-/-}$ livers, and plasma α-hydoxybutyrate levels were not significantly affected
281 (Figure 5E). Thus, impairment of mitochondrial complex IV has both biochemical and

282 functional consequences in the adult liver, and is required for maintenance of cellular
283 redox status.

284 To probe the effects of complex IV loss in mammalian liver, we assessed proteome
285 changes by label-free proteomics (Figure 5F, Table S2). Unsupervised hierarchical
286 clustering was able to separate proteomes between *cox10*$^{f/f}$ and *cox10*$^{-/-}$ livers (Figure
287 5F). A large number of proteins were significantly up-regulated ($\log_2$(Fold Change) > 1;
288 p-value < 0.05), and this group was enriched (209 out of 319) for proteins that localize to
289 mitochondria (Figure 5G (red dots), Table S2). Gene ontology analysis of upregulated
290 proteins revealed enrichment of a large number of mitochondrial pathways in all three
291 categories (Biological Processes (BP), Cellular Components (CC), and Molecular
292 Functions (MF)) (Table S2, Figure 5 – figure supplement 1A (red arrows)). Consistent
293 with this, there were significant increases in total mitochondrial content in *cox10*$^{-/-}$ livers,
294 as measured by both mitochondrial genome and protein content (Figure 5I-K; Figure 5 –
295 figure supplement 5). A separate analysis focused on non-mitochondrial proteins that
296 were upregulated did not reveal many pathways that were significantly enriched
297 (FDR<0.05), with the single exception of the cornified envelope cellular component
298 pathway, which included various genes implicated in cell damage and death processes
299 (e.g., S100A9 (*38, 39*), LGALS3 (*40*), NCL (*41-43*), HSPB1 (*44*)) (Table S2, Figure 5 –
300 figure supplement 1B) and may potentially be related to the hepatic damage observed in
301 this animal model (Figure 4K).

302 Only a small number of mitochondrial proteins were present among the down-
303 regulated proteins (16 of 214), among which we identified a number of complex IV
304 components (Figure 5G,H), consistent with destabilization of intact complex IV due to loss

305 of an assembly subunit. We did not observe significant decreases in components from
306 other ETC complexes, suggesting an isolated effect of cox10 loss on complex IV (Figure
307 5H). Consistent with this, gene ontology analysis identified complex IV as the only Cellular
308 Components pathway enriched among the down-regulated genes (Table S2). Several
309 biological processes related to metabolism were enriched among the down-regulated
310 genes which included lipid metabolic and biosynthetic pathways (Figure 5 – figure
311 supplement 2A,B (blue arrows)). Thus, proteomic changes in response to hepatic
312 complex IV deficiency largely center around increased mitochondrial constituents, as well
313 as decreased enzyme abundance for a number of metabolic pathways.

314 Steady-state metabolomic analysis of hepatic tissue revealed a number of
315 metabolites altered in response to complex IV loss, and unsupervised hierarchical
316 clustering was sufficient to separate *cox10*$^{f/f}$ and *cox10*$^{-/-}$ livers (Figure 5L,M).
317 Mitochondrial TCA cycle metabolites were largely maintained, although we observed a
318 significant increase in 2-hydroxyglutarate levels, which has been previously observed in
319 the setting of mitochondrial dysfunction (Figure 5N) (*45*). We observed significant
320 upregulation in a number of cholate species, consistent with cholestasis and
321 hepatomegaly in these animals (Figure 5M, Figure 5 – figure supplement 3A).
322 Upregulated metabolites were also highly enriched for long-chain acylcarnitine fatty acid
323 species, consistent with a fatty acid oxidation defect (Figure 5M). We therefore assessed
324 proteomic changes in annotated GO pathways related to fatty acid and bile acid
325 metabolism (Figure 5 – figure supplement 4). A number of enzymes related to fatty acid
326 synthesis exhibited statistically significant changes in *cox10*$^{-/-}$ livers, including
327 downregulation of FASN, the key fatty acid synthesis enzyme (Figure 5 – figure

328 supplement 4A). However, we did not observe overall enrichment or depletion of this
329 pathway by gene set enrichment analysis (GSEA) (Figure 5 – figure supplement 4A).
330 Fatty acid oxidation enzymes tended to be enriched in *cox10*$^{-/-}$ livers, which was perhaps
331 driven by the accumulation of mitochondrial proteins in this setting (Figure 5 – figure
332 supplement 4B). In contrast, abundance of bile acid metabolic enzymes tended to be
333 decreased in *cox10*$^{-/-}$ livers, although the overall pathway depletion did not reach
334 statistical significance (Figure 5 – figure supplement 4C).

335 Downregulated metabolites were enriched for several electron carriers, including
336 pyruvate, ascorbate and tetrahydrobiopterin (Figure 5M, Figure 5 – figure supplement
337 3B). Pyruvate can exchange electrons with NAD(H), while ascorbate and THBP are
338 potent antioxidants which can exchange electrons with metal ions and hydroxyradical
339 species (*46, 47*). Thus, inhibition of the mitochondrial ETC via Cox10 removal may
340 influence redox balance in multiple species. To assess related proteomic changes, we
341 investigated alterations in genes of the oxidoreductase family, a large family related to
342 transfer of electrons between many potential substrates (GO: 0016491; 787 members).
343 Overall, oxidoreductase enzymes trended to be upregulated in *cox10*$^{-/-}$ livers, largely
344 driven by mitochondrial-localized proteins, and we did identify a small number of enzymes
345 related to pyruvate, ascorbate and THBP metabolism as significantly altered in response
346 to hepatic complex IV loss (Figure 5 – figure supplement 4D).

347

348 **Complex IV inhibition blocks electron entry from the electron transfer flavoprotein**
349 **(ETF) complex.**

350 In cultured cells, Complex IV is the major source of oxygen consumption. To
351 examine this *in vivo*, we performed magnetic resonance imaging in *cox10*$^{f/f}$ and *cox10*$^{-/-}$
352 animals as described above (Figure 3E). Based on arterial spin labeling measurements,
353 we observed no alterations in perfusion of *cox10*$^{-/-}$ livers (Figure 6A). In addition, BOLD
354 (T2*) measurements indicated significant increases in blood oxygen content in both
355 genotypes in response to 100% O_2, based on increases in the T2* relaxation time (Figure
356 6B). Similar to above results, *cox10*$^{f/f}$ (wild-type) livers did not display increases in tissue
357 oxygen levels, based on TOLD imaging and average T1 parameters (Figure 6C-E). In
358 contrast, *cox10*$^{-/-}$ livers displayed significant decreases in average T1 relaxation times in
359 response to a 100% O_2 challenge, indicating increased dissolved oxygen levels in
360 affected liver tissue (Figure 6C-E). A regional assessment of changes in T1 (ΔT1) also
361 indicated decreased T1 parameters in *cox10*$^{-/-}$, but not *cox10*$^{f/f}$ livers (Figure 6F). Thus,
362 *cox10*$^{-/-}$ livers are deficient in maintaining oxygen levels in response to increased blood
363 O_2 delivery, consistent with decreased oxygen consumption in the setting of cIV
364 deficiency.

365 The contrast in the tissue oxygen status between *ndufa9*$^{-/-}$ and *cox10*$^{-/-}$ livers
366 suggests that complex I is not a significant electron donor to the hepatic ETC, at least
367 under homeostatic conditions. If complex I was a major electron source, we would expect
368 that depletion of complex IV might result in altered glucose utilization in the mitochondria.
369 We therefore performed steady-state euglycemic infusions of [U-^{13}C]glucose in *cox10*$^{f/f}$
370 and *cox10*$^{-/-}$ animals (Figure 6G). Similar to *ndufa9*$^{-/-}$ animals, we did not observe altered
371 glucose handling in *cox10*$^{-/-}$ animals (Figure 6H,I; Figure 6 – figure supplement 1A),

372 suggesting that complex I activity is low and glucose utilization in the mitochondria is not
373 sensitive to ETC function.

374 In principle, there are several paths of electron entry (Figure 6J) independent of
375 complex I, including complex II (which receives electron from succinate), DHODH (which
376 receives electrons from dihydroorotate), GPD2 (which receives electrons from glycerol 3-
377 phosphate), and the electron transfer flavoprotein (ETF) complex (which receives
378 electrons from $FADH_2$). These alternate routes bypass complex I by donating electrons
379 directly to ubiquinone. Complex IV dysfunction is expected to impact all of these routes;
380 however, we would only expect to see significant metabolic alterations in pathways with
381 high flux. In culture, ETC inhibition is commonly associated with elevated succinate levels;
382 however, we did not observe this result in *cox10*$^{-/-}$ livers (Figure 6K). Similarly, we did not
383 observed elevations in glycerol 3-phosphate or dihydroorotate (Figure 6K), suggesting
384 that GPD2 and DHODH activities are not a major electron source in murine livers.

385 Lastly, we examined whether the ETF complex constitutes a significant electron
386 source to the hepatic ETC. The ETF complex is made up of three proteins (ETFA, ETFB
387 and ETFDH), which transfers electrons from $FADH_2$ to ubiquinone. Significant sources of
388 $FADH_2$ are thought to include fatty acids (via beta-oxidation), as well as amino acid
389 metabolism (Figure 6J). In *cox10*$^{-/-}$ livers, we observed significant elevations in
390 medium/long chain acyl-carnitines (Figure 6L), as well as a decreased in β-
391 hydroxybutyrate levels (Figure 6M), consistent with a fatty acid oxidation defect. In
392 addition, we observed a striking increase in glutarate levels (Figure 6N), consistent with
393 a selective defect in amino acid metabolism linked to $FADH_2$. Thus, the metabolic

394 abnormalities observed in *cox10*$^{-/-}$ livers are most consistent with a buildup of ETFDH
395 substrates.
396
397
398
399
400
401
402
403
404
405
406
407
408
409
410
411
412
413
414
415
416

417 **Discussion**

418 The dispensability of complex I for homeostatic function in the adult murine liver is not
419 consistent with a key role for cI in electron entry to the ETC in this tissue; in particular, we
420 observed no alterations in mitochondrial or cytosolic redox status in cI-deficient liver, or
421 evidence of significant metabolic, histologic or functional alterations. It is possible that cI-
422 related defects are minor and not detectable by our assays. The mouse liver is known to
423 have relatively low flux through PDH, the major entry point of carbons to the TCA cycle
424 which generates NADH for cI function (*29, 30*); thus, our data is consistent with a model
425 in which the hepatic TCA cycle does not play a prominent role in nutrient oxidation via the
426 generation of mitochondrial NADH under homeostatic conditions. The impact of cIV
427 deficiency on cellular redox status indicates that the mitochondrial ETC is critical for
428 removing electrons via transfer to oxygen, and thus, alternative electron donors are likely
429 to fuel the ETC. However, the lack of a survival deficit in *cox10*$^{-/-}$ animals in this study
430 calls into question the absolute requirement for an intact mitochondrial ETC in mouse
431 liver.

432 A precise measurement of the source of electrons for the ETC is challenging due
433 to an inability to directly track electrons after incorporation into the redox-sensitive
434 cofactors used by the mitochondrial ETC complexes. Our results from complex IV
435 dysfunctional livers reveal a buildup of substrates that normally feed into the ETF
436 complex, including elevations in multiple acyl-carnitine species, as well as glutarate, a by-
437 product of lysine and tryptophan metabolism. In principle, the buildup of acyl-carnitines
438 could be due to increased rates of fatty acid synthesis (FAS); however, we did not observe
439 elevated levels of FAS enzymes. In addition, the reduction in β-hydroxybutyrate (a

440 terminal product of fatty acid oxidation) levels combined with the large increases in fatty
441 acid species is most consistent with a defect in fatty acid oxidation (FAO), although these
442 steady state measurements do not directly inform on flux through FAO pathways, and
443 experiment to directly trace flux through the ETF complex will be necessary.

444 In humans, mutations in proteins of the ETF complex are causative for glutaric
445 acidemia type II disease (also known as multiply acyl-CoA dehydrogenase deficiency),
446 which has similar biochemical abnormalities (*48, 49*). The clinical progression of these
447 patients can be variable; however, patients with hepatic involvement exhibit hepatic
448 steatosis, elevated ALT/AST levels and periodic hypoglycemia (*50*). In addition, mice
449 carrying a knock-in ETFDH mutation displayed diet-dependent phenotypes, including
450 hepatic steatosis and elevated levels of acyl-carnitine species (*51*). Lastly, patients with
451 SCO1 mutations (impacting complex IV assembly) display hepatic steatosis and elevated
452 acyl-carnitines (*8, 52*), suggesting a clinical overlap between mitochondrial ETC inhibition
453 and ETF complex deficiency.

454 Our results therefore indicate the complex I is dispensable in the adult murine liver,
455 and suggest that the ETF complex may instead constitute a significant electron source
456 for the hepatic ETC. A limitation of our study is that we have focused on steady state
457 analysis of homeostatic functions in the mouse liver of the C57BL/6J background, and it
458 is possible that complex I does have a required role in alternative genetic backgrounds,
459 or in the setting of hepatic stressors or alternative diets. Indeed, it has been reported that
460 C57BL/6J animals contain a mutation which prevents the incorporation of multimeric
461 complex IV into supercomplexes, and so the major contributing sources of electrons for
462 the ETC may be different in this background (*53, 54*). Thus, it is possible that cI is required

463 in other genetic backgrounds and it will be important to assess these scenarios in future
464 work. Indeed, the relevant and high flux modes of electron entry into the ETC may be
465 different among distinct tissues and backgrounds, and this provides a plausible
466 hypothesis for the non-overlapping syndromes present in mitochondrial ETC diseases
467 affecting different components. As an upstream component of the ETC, cI mutations from
468 the mitochondrial or nuclear genome may manifest in a narrow set of tissues systems
469 which rely on mitochondrial NADH to fuel respiration. In contrast, complex IV, the terminal
470 component of the ETC which feeds electrons to oxygen as a final electron acceptor, might
471 be predicted to have effects in a wider variety of tissues, particularly those which do not
472 have alternative pathways to remove excess electrons. Understanding the key ETC fuel
473 sources in both normal and stressed tissue systems will therefore provide insight into the
474 pathophysiological processes which occur downstream of specific mitochondrial
475 mutations.
476
477
478
479
480
481
482
483
484
485

486 **Acknowledgments**

487 We thank the Hao Zhu lab for assistance with liver experiments, the UT Southwestern
488 Metabolic Phenotyping Core for plasma analysis, the UT Southwestern Proteomics Core,
489 the CRI Metabolomics Facility, the Biochemistry Metabolomics Core, the UT
490 Southwestern Small Animal Imaging Resource and members of the Mishra and
491 DeBerardinis laboratories for helpful discussions and suggestions during this project.
492 Diagrams were created with BioRender.com. **Funding:** This work was supported by
493 funding from the United Mitochondrial Disease Foundation (Research Grant to P.M.), the
494 National Institutes of Health (1DP2ES030449-01 from NIEHS to P.M., 1R01AR073217-
495 01 from NIAMS to P.M., 1F31-DK122676 from NIDDK to N.P.L.), the Moody Medical
496 Research Institute (Research Grant to P.M.), and the National Science Foundation
497 (GRFP 2019281210 award to S.D.S.). **Author Contributions: N.P.L.:** Conceptualization,
498 Methodology, Validation, Formal analysis, Investigation, Data curation, Writing – Original
499 Draft, Writing – Review & Editing, Visualization. **X.W.:** Investigation. **Z.C.**: Investigation.
500 **C.M.**: Investigation. **S.H.:** Investigation. **A.F.:** Investigation. **S.D.S:** Investigation. **D.G.M.:**
501 Resources. **J.W.**: Resources, Methodology, Formal Analysis, Investigation, Data
502 curation, Writing – Review & Editing, Visualization. **R.J.D.:** Resources, Writing – Review
503 & Editing. **P.M.:** Conceptualization, Methodology, Formal analysis, Resources, Data
504 curation, Writing – Original Draft, Writing – Review & Editing, Visualization, Supervision,
505 Funding acquisition. **Competing Interests:** R.J.D. is an advisor to Agios
506 Pharmaceuticals. **Data and material availability:** All data and materials are provided
507 within the manuscript and supplementary materials, or available upon reasonable
508 request. Proteomics datasets have been deposited into the PRIDE database (identifier

509 PXD031716; reviewer account details: Username: reviewer_pxd031716@ebi.ac.uk;

510 Password: yHS3ofKF).

511

512

513

514

515

516

517

518

519

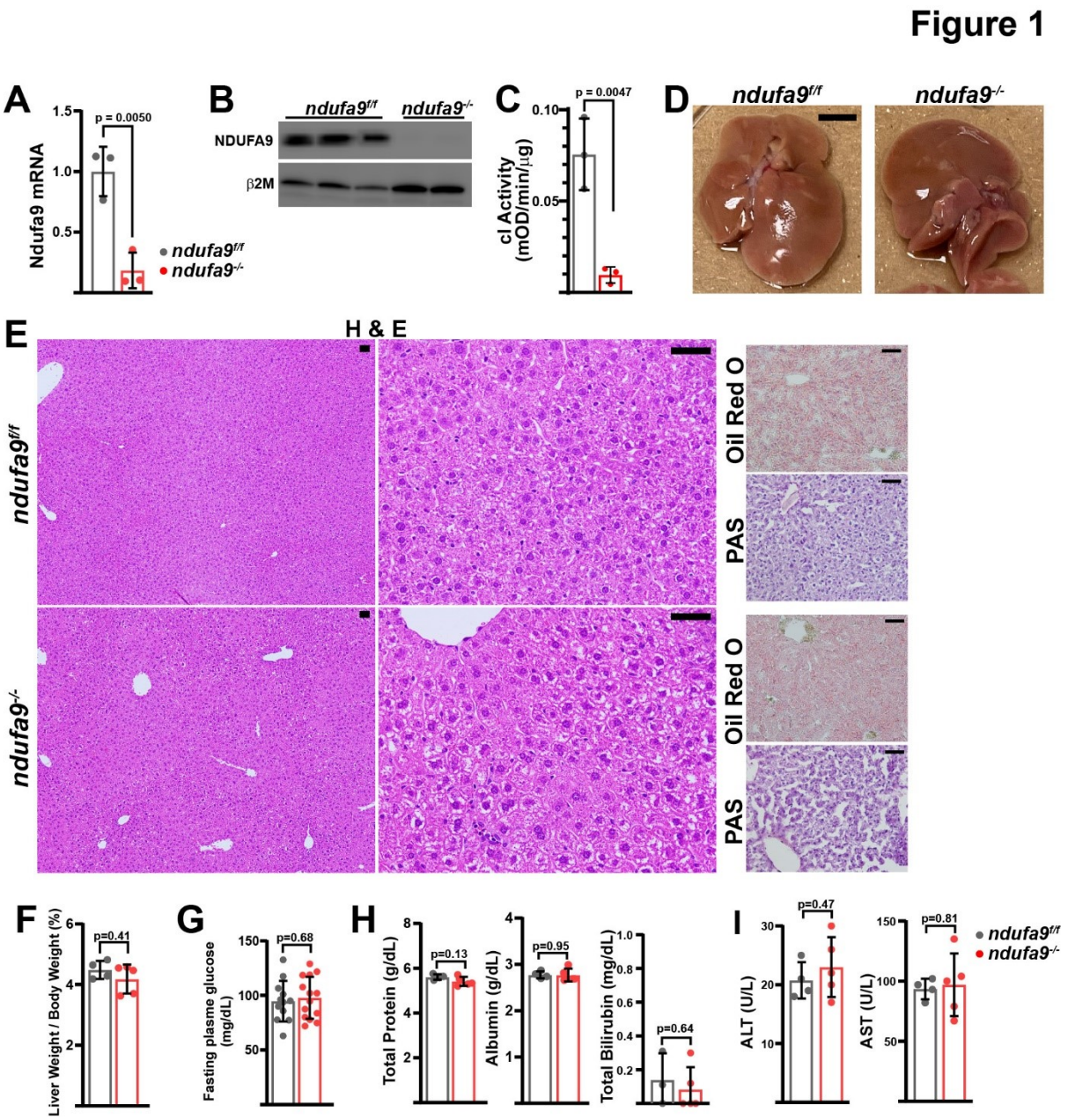

Figure 1. Mitochondrial complex I is dispensable in adult murine hepatocytes. (A) *ndufa9* mRNA levels (relative to β2-microglobulin; normalized) in isolated hepatocytes of the indicated genotype, assessed by qRT-PCR. n=3 animals per group. The same color scheme is used throughout this figure. **(B)** *Ndufa9* protein levels in isolated hepatocytes of the indicated genotype, assessed by Western blot. β2-microglobulin levels are shown

526 as a loading control. **(C)** Complex I activity measurements from livers of the indicated
527 genotype. n=3 animals per group. **(D)** Representative images of gross liver anatomy in
528 animals of the indicated genotype. Scale bar: 0.5cm. **(E)** Representative histology (H&E,
529 Oil Red O, PAS staining) images of liver cross sections from animals of the indicated
530 genotype. Scale bar: 50μm. **(F)** Liver weight (normalized to body weight) from mice of the
531 indicated genotype. n=4-5 animals per group. **(G)** Fasting plasma glucose levels in mice
532 of the indicated genotype. n=12-14 animals per group. **(H)** Circulating plasma markers
533 (total protein, albumin, and total bilirubin) of liver function in mice of the indicated
534 genotype. n=3-5 animals per group. **(I)** Plasma markers (ALT and AST) of liver damage
535 in mice of the indicated genotype. n=4-5 mice per group. All data were collected at 4
536 weeks post AAV-administration. Statistical significance was assessed using two-tailed t-
537 test (A,C,G,H,I) or Mann-Whitney (F,H) tests with adjustments for multiple comparisons.
538 All data represent mean +/- standard deviation from biological replicates.
539
540
541
542
543
544
545
546
547
548

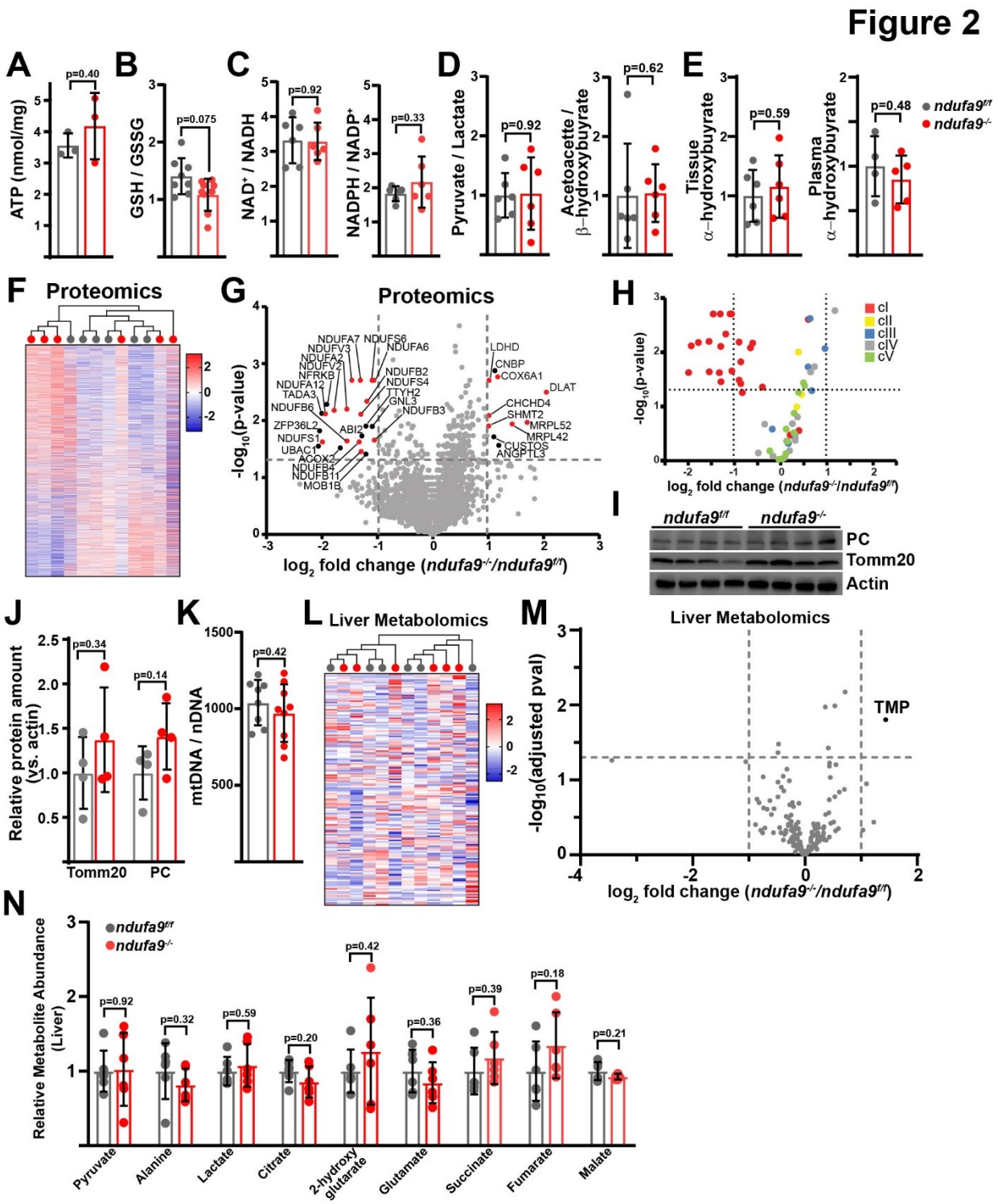

Figure 2. Complex I deficiency in adult liver does not impact redox status. (A) ATP levels from livers of the indicated genotype. n=3 mice per group. The same color scheme is used throughout this figure. **(B)** Reduced glutathione to oxidized glutathione ratio

552 (GSH/GSSG) in livers of the indicated genotype, as a proxy of oxidative stress. n=8-9
553 mice per group. **(C)** NAD^+/NADH and NADPH/$NADP^+$ ratios in livers of the indicated
554 genotype. n=6 mice per group. **(D)** Normalized cytosolic (pyruvate / lactate) and
555 mitochondrial (acetoacetate / β–hydroxybutyrate) redox ratios in livers of the indicated
556 genotype. n=6 mice per group. **(E)** Tissue and plasma α–hydroxybutyrate levels in
557 animals of the indicated genotype. n=4-6 mice per group. **(F)** Unsupervised hierarchical
558 clustering of protein abundances in *ndufa9*$^{f/f}$ and *ndufa9*$^{-/-}$ livers, depicted as a heatmap
559 of z-scores. **(G)** Volcano plot of protein abundances changes in *ndufa9*$^{-/-}$ vs. *ndufa9*$^{f/f}$
560 livers, based on proteomics analysis. Log_2(Fold change) is plotted against the –
561 log_{10}(adjusted p-value) for each protein. Significantly changing proteins (log_2(Fold
562 change) >1 or < -1; Adjusted p-val<0.05) are colored black, and mitochondrial proteins
563 are colored red. n=6 mice per group. **(H)** Volcano plot of abundances for mitochondrial
564 ETC proteins in *ndufa9*$^{-/-}$ vs. *ndufa9*$^{f/f}$ livers, based on proteomics analysis. **(I)** Levels of
565 mitochondrial proteins (PC, pyruvate carboxylase, and Tomm20) in livers of the indicated
566 genotype, as assessed by Western blot. Actin levels are shown as a loading control. **(J)**
567 Relative amounts of Tomm20 and PC in livers of the indicated genotype, relative to actin
568 levels. n=4 animals per group. **(K)** Mitochondrial genome (mtDNA) to nuclear genome
569 (nDNA) ratios in livers of the indicated genotype. n=8-9 mice per group. **(L)** Unsupervised
570 hierarchical clustering of liver metabolite abundances in *ndufa9*$^{f/f}$ and *ndufa9*$^{-/-}$ livers,
571 depicted as a heatmap of z-scores. **(M)** Volcano plot of metabolite abundance changes
572 in *ndufa9*$^{-/-}$ vs. *ndufa9*$^{f/f}$ livers, based on metabolomics analysis. Log_2(Fold change) is
573 potted against the –log_{10}(adjusted p-value) for each metabolite. Significantly changing
574 metabolites (log_2(Fold change) >1 or < -1; Adjusted p-val<0.05) are colored black. TMP,

575 Thiamine monophosphate. n=6 mice per group. **(N)** Relative abundances of mitochondrial
576 TCA cycle and related metabolites from livers of the indicated genotype. n=6 mice per
577 group. All data were collected at 4 weeks post AAV-administration. Statistical significance
578 was assessed using two-tailed t-test (A,C,D,E,J,K,N) or Mann-Whitney (B) with
579 adjustments for multiple comparisons. All data represent mean +/- standard deviation
580 from biological replicates.
581
582
583

Figure 3

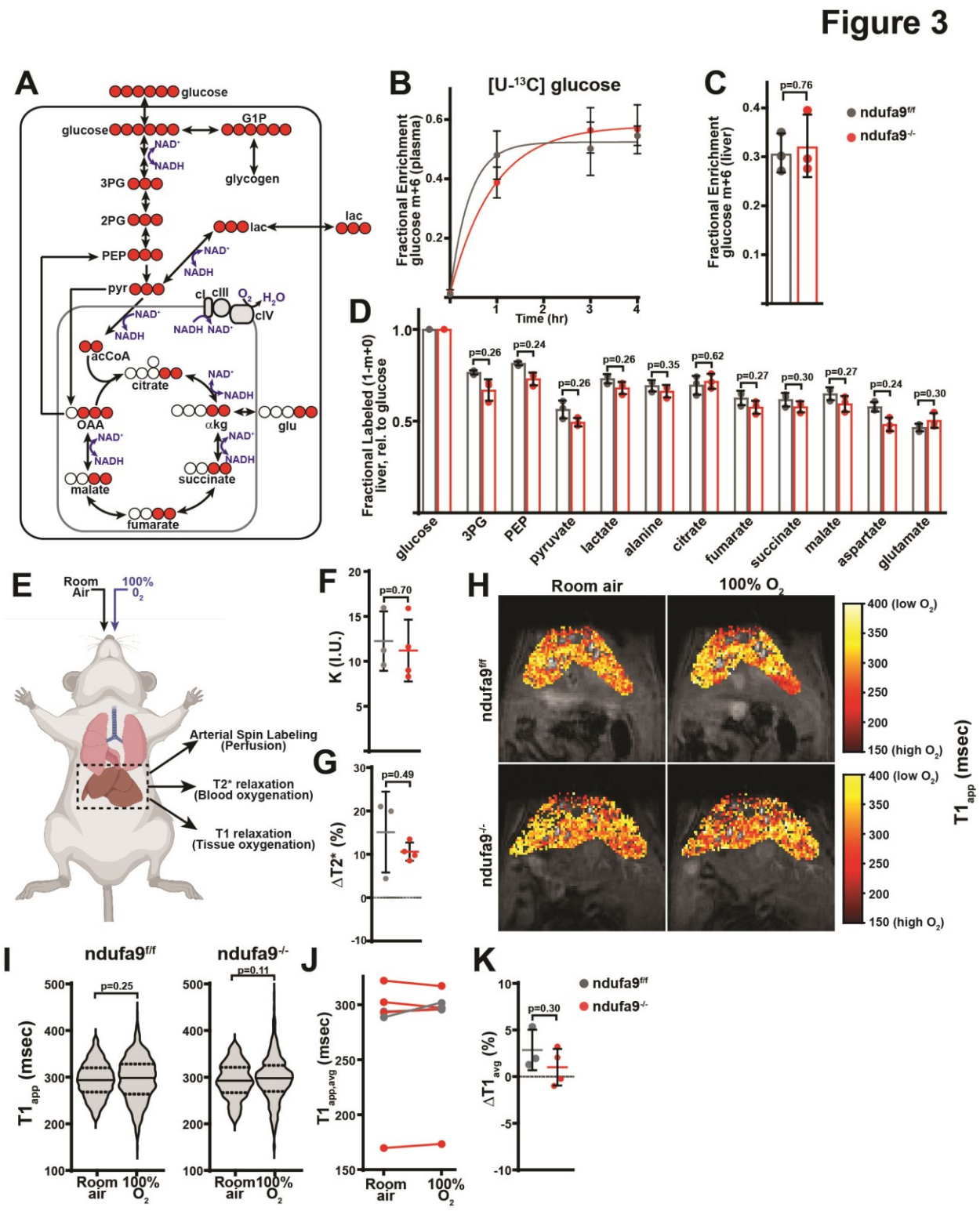

Figure 3. Complex I deficiency in adult liver does not impact glucose utilization or oxygen status. (A) Schematic of expected labeling patterns from [U-^{13}C]glucose

587 infusions. ^{13}C atoms are indicated with red circles. G1P, glucose-1-phosphate; 3PG, 3-
588 phosphoglycerate; 2PG, 2-phosphoglycerate; PEP, phosphoenolpyruvate; pyr, pyruvate;
589 lac, lactate; acCoA, acetyl-CoA; OAA, oxaloacetate; glu, glutamate; αkg, αketoglutarate.
590 **(B)** Plasma enrichment of m+6 glucose during steady-state infusions of [U-^{13}C]glucose.
591 n=3 animals per group. The same color scheme is used throughout this figure. **(C)**
592 Steady-state liver enrichment of m+6 glucose in animals of the indicated genotype. n=3
593 animals per group. **(D)** Labeled fractions (1-(m+0)) of the indicated metabolites, relative
594 to liver glucose m+6 enrichment. n=3 animals per group. **(E)** Schematic of MRI
595 experiments. Anesthetized animals were challenged to breath room air, followed by 100%
596 O_2, followed by MR imaging to measure perfusion (in room air), and blood and tissue
597 oxygenation in each condition. **(F)** Perfusion values (reported as institutional units (I.U.))
598 based on arterial spin labeling in animals of the indicated genotype. n=3-4 animals per
599 group. **(G)** Relative (%) changes in hepatic T2* following exposure to 100% O_2 in animals
600 of the indicated genotype. n=3-4 animals per group. **(H)** Representative heatmaps of T1
601 apparent values ($T1_{app}$) in livers, overlaid on T1-weighted MR images. **(I)** Representative
602 distribution of $T1_{app}$ values in an animal of each genotype breathing room air, followed by
603 100% O_2. **(J)** Average hepatic $T1_{app}$ values in animals of the indicated genotype,
604 breathing room air followed by 100% O2. n=3-4 animals per group. **(K)** Average regional
605 changes in T1 (ΔT1) in animals of the indicated genotype. n=3-4 animals per group. All
606 data were collected at 4 weeks post AAV-administration. Statistical significance was
607 assessed using two-tailed t-test (C,D,F,G,K) or Mann-Whitney (I) with adjustments for
608 multiple comparisons. All data represent mean +/- standard deviation from biological
609 replicates.

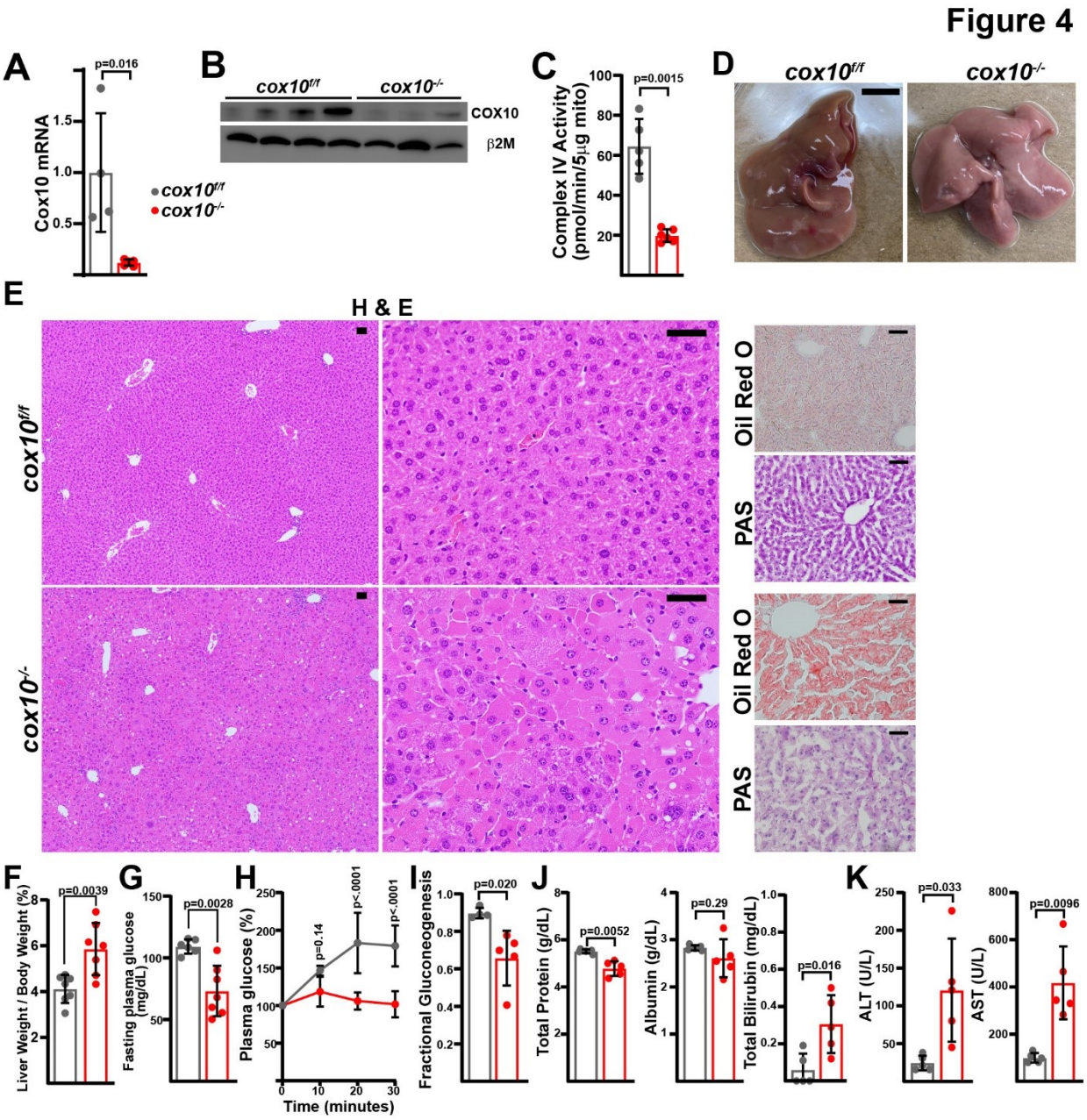

Figure 4. Complex IV deficiency in adult hepatocytes induces liver dysfunction. (A) Cox10 mRNA levels (relative to β2-microglobulin; normalized) in livers of the indicated genotype, assessed by qRT-PCR at 4 weeks post-AAV administration. n=4-5 animals per group. The same color scheme is used throughout this figure. **(B)** Cox10 protein levels in livers of the indicated genotype, assessed by Western blot at 4 weeks post AAV-administration. β2-microglobulin levels are shown as a loading control. **(C)** Complex IV

616 activity (pmol O_2 consumed / min) in isolated mitochondria supplemented with
617 ascorbate/TMPD substrates from livers of the indicated genotype, assessed at 4 weeks
618 post AAV-administration. n=5-6 animals per group. **(D)** Representative images of gross
619 liver anatomy in animals of the indicated genotype at 8 weeks post AAV-administration.
620 Scale bar: 0.5cm. **(E)** Representative histology (H&E, Oil Red O, PAS staining) images
621 of liver cross sections from animals of the indicated genotype at 8 weeks post-AAV
622 administration. Scale bar: 50μm. **(F)** Liver weight (normalized to body weight) from mice
623 of the indicated genotype at 8 weeks post-AAV administration. n=7 animals per group.
624 **(G)** Fasting plasma glucose levels in mice of the indicated genotype at 8 weeks post-AAV
625 administration. n=6-7 animals per group. **(H)** Relative changes in plasma glucose
626 following a lactate/pyruvate tolerance test in mice of the indicated genotype at 8 weeks
627 post-AAV administration. n=4-5 mice per group. **(I)** Fractional gluconeogenesis (plasma)
628 in animals of the indicated genotype, measured via pyruvate/lactate tolerance test at 8
629 weeks post-AAV administration. n=4-5 animals per group. **(J)** Circulating plasma markers
630 (total protein, albumin, and total bilirubin) of liver function in mice of the indicated genotype
631 at 8 weeks post-AAV administration. n=5 animals per group. **(K)** Plasma markers (ALT
632 and AST) of liver damage in mice of the indicated genotype at 8 weeks post-AAV
633 administration. n=5 mice per group. Statistical significance was assessed using two-way
634 ANOVA (H), t-test (C,F,G,I,J,K) or Mann-Whitney (A,K) tests with adjustments for multiple
635 comparisons. All data represent mean +/- standard deviation from biological replicates.
636
637

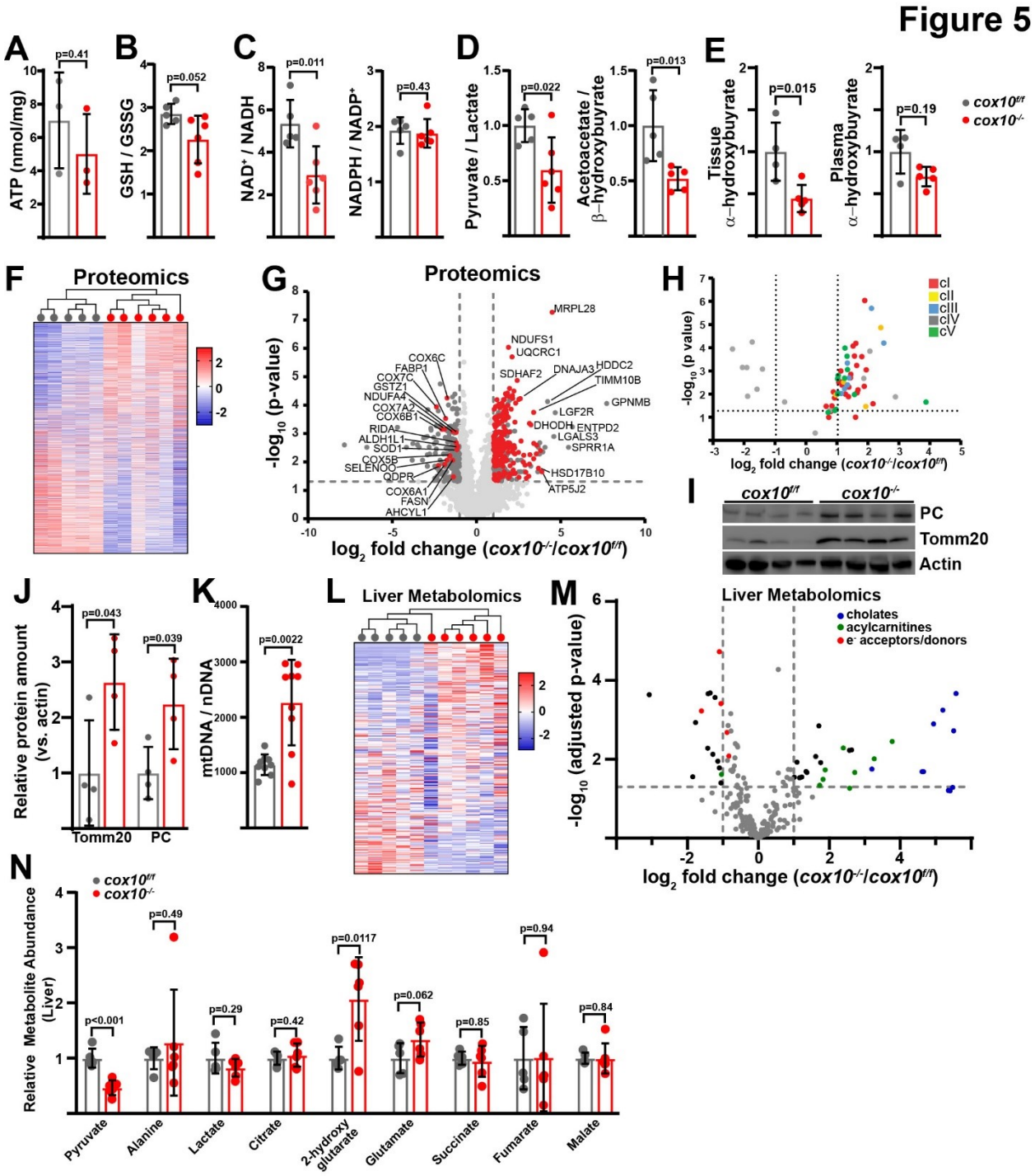

Figure 5. Complex IV deficiency alters metabolism and cellular redox status in adult liver. (A) ATP levels in livers of the indicated genotype. n=3 animals per group. The same color scheme is used throughout this figure. **(B)** Reduced glutathionine to oxidized glutathionine ratio (GSH:GSSG) in livers of the indicated genotype, as a proxy of oxidative

642 stress. n=5-6 mice per group. **(C)** NAD^+/NADH and NADPH/$NADP^+$ ratios in livers of the
643 indicated genotype. n=5-6 mice per group. **(D)** Normalized cytosolic (pyruvate / lactate)
644 and mitochondrial (acetoacetate / β–hydroxybutyrate) redox ratios in livers of the
645 indicated genotype. n=5-6 mice per group. **(E)** Normalized tissue and plasma
646 α–hydroxybutyrate levels in animals of the indicated genotype. n=4-5 mice per group. **(F)**
647 Unsupervised hierarchical clustering of protein abundances in *cox10*$^{f/f}$ and *cox10*$^{-/-}$ livers,
648 depicted as a heatmap of z-scores. **(G)** Volcano plot of protein abundances changes in
649 *cox10*$^{-/-}$ vs. *cox10*$^{f/f}$ livers, based on proteomics analysis. Log_2(Fold change) is plotted
650 against the $-log_{10}$(adjusted p-value) for each protein. Significantly changing proteins
651 (log_2(Fold change) >1 or < -1; Adjusted p-val<0.05) are colored black; of these,
652 mitochondria-localized proteins are colored red. n=5-6 mice per group. **(H)** Volcano plot
653 of abundances for mitochondrial ETC proteins in *cox10*$^{-/-}$ vs. *cox10*$^{f/f}$ livers, based on
654 proteomics analysis. **(I)** Levels of mitochondrial proteins (PC, pyruvate carboxylase, and
655 Tomm20) in livers of the indicated genotype, as assessed by Western blot. Actin levels
656 are shown as a loading control. **(J)** Relative amounts of Tomm20 and PC in livers of the
657 indicated genotype, relative to actin levels. n=4 animals per group. **(K)** Mitochondrial
658 genome (mtDNA) to nuclear genome (nDNA) ratios in livers of the indicated genotype.
659 n=9 mice per group. **(L)** Unsupervised hierarchical clustering of metabolite abundances
660 in *cox10*$^{f/f}$ and *cox10*$^{-/-}$ livers, depicted as a heatmap of z-scores. **(M)** Volcano plot of
661 metabolite abundance changes in *cox10*$^{-/-}$ vs. *cox10*$^{f/f}$ livers, based on metabolomics
662 analysis. Log_2(Fold change) is potted against the $-log_{10}$(adjusted p-value) for each
663 metabolite. Significantly changing metabolites (log_2(Fold change) >1 or < -1; Adjusted p-
664 val<0.05) are colored black. n=5-6 mice per group. **(N)** Relative abundances of

665 mitochondrial TCA cycle and related metabolites from livers of the indicated genotype.
666 n=5-6 mice per group. All data in this figure were collected at 8 weeks post AAV-
667 administration. Statistical significance was assessed using t-test (A,B,C,D,E,J,K,N), or
668 Mann-Whitney (C,E) tests with adjustments for multiple comparisons. All data represent
669 mean +/- standard deviation from biological replicates.
670

Figure 6

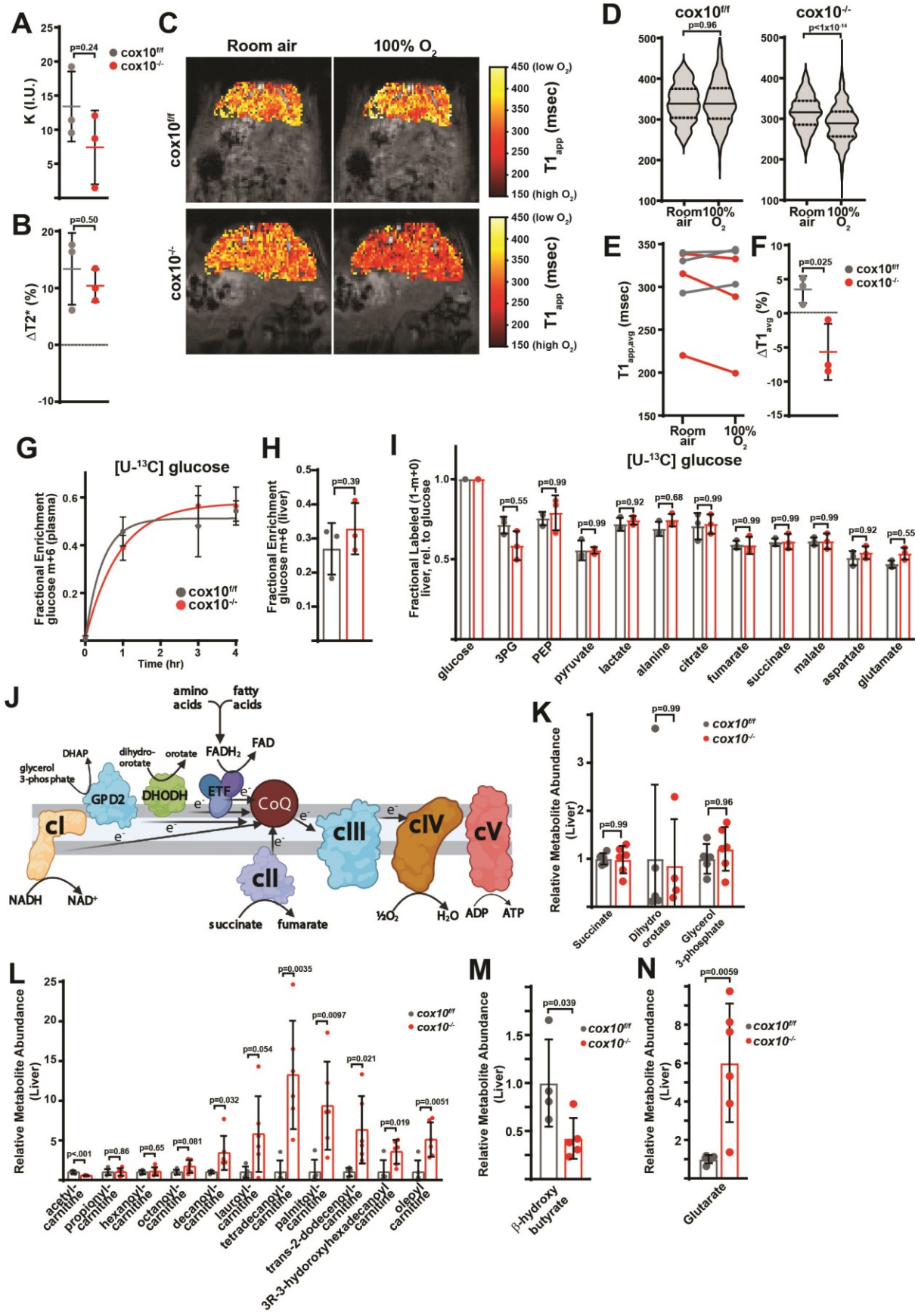
A
K (I.U.)
p=0.24
cox10f/f
cox10-/-
B
ΔT2* (%)
p=0.50
C
Room air
100% O2
cox10f/f
cox10-/-
450 (low O2)
150 (high O2)
T1app (msec)
D
cox10f/f
cox10-/-
p=0.96
p<1x10-14
Room air
100% O2
E
T1app,avg (msec)
F
ΔT1avg (%)
p=0.025
G
[U-13C] glucose
Fractional Enrichment glucose m+6 (plasma)
Time (hr)
H
Fractional Enrichment glucose m+6 (liver)
p=0.39
I
[U-13C] glucose
Fractional Labeled (1-m+0) liver, rel. to glucose
glucose
3PG
PEP
pyruvate
lactate
alanine
citrate
fumarate
succinate
malate
aspartate
glutamate
J
amino acids
fatty acids
FADH2
FAD
DHAP
glycerol 3-phosphate
dihydro-orotate
orotate
GPD2
DHODH
ETF
CoQ
cI
cII
cIII
cIV
cV
NADH
NAD+
succinate
fumarate
½O2
H2O
ADP
ATP
K
Relative Metabolite Abundance (Liver)
p=0.99
p=0.96
Succinate
Dihydro orotate
Glycerol 3-phosphate
L
Relative Metabolite Abundance (Liver)
p<.001
p=0.86
p=0.65
p=0.081
p=0.032
p=0.054
p=0.0035
p=0.0097
p=0.021
p=0.019
p=0.0051
acetyl-carnitine
propionyl-carnitine
hexanoyl-carnitine
octanoyl-carnitine
decanoyl-carnitine
lauroyl-carnitine
tetradecanoyl-carnitine
palmitoyl-carnitine
trans-2-dodecenoyl-carnitine
3R-3-hydoroxyhexadecanoyl carnitine
oleoyl carnitine
M
Relative Metabolite Abundance (Liver)
p=0.039
β-hydroxy butyrate
N
Relative Metabolite Abundance (Liver)
p=0.0059
Glutarate

672 **Figure 6. Complex IV deficiency impairs electron transport chain function and**
673 **oxygen status in the adult liver. (A)** Perfusion values (reported as institutional units
674 (I.U.)) based on arterial spin labeling in animals of the indicated genotype at 4 weeks
675 post-AAV administration. n=3 animals per group. The same color scheme is used
676 throughout this figure. **(B)** Relative (%) changes in hepatic T2* following exposure to
677 100% O_2 in animals of the indicated genotype at 4 weeks post-AAV administration. n=3
678 animals per group. **(C)** Representative heatmaps of T1 apparent values ($T1_{app}$) in livers,
679 overlaid on T1-weighted MR images. **(D)** Representative distribution of $T1_{app}$ values in an
680 animal of each genotype breathing room air, followed by 100% O_2. **(E)** Average hepatic
681 $T1_{app}$ values in animals of the indicated genotype, breathing room air followed by 100%
682 O_2. n=3 animals per group; 4 weeks post-AAV administration. **(F)** Average regional
683 changes in T1 (ΔT1) in animals of the indicated genotype. n=3 animals per group; 4 weeks
684 post-AAV administration. **(G)** Plasma enrichment of m+6 glucose during steady-state
685 infusions of [U-^{13}C]glucose. n=3 animals per group; 4-weeks post-AAV administration.
686 **(H)** Steady-state liver enrichment of m+6 glucose in animals of the indicated genotype.
687 n=3 animals per group; 4 weeks post-AAV administration. **(I)** Labeled fractions (1-(m+0))
688 of the indicated metabolites, relative to liver glucose m+6 enrichment. n=3 animals per
689 group; 4 weeks post-AAV administration. **(J)** Schematic of potential electron sources for
690 mitochondrial ETC. CoQ, ubiquinone; GPD2, mitochondrial glycerol-3-phosphate
691 dehydrogenase; DHODH, dihydroorotate dehydrogenase. ETF, electron transfer
692 flavoprotein complex. DHAP, dihydroxyacetone phosphate. **(K)** Relative abundance of
693 electron donors in livers of the indicated genotype at 8 weeks post-AAV administration.
694 n=4-6 mice per group. **(L)** Relative abundance of acylcarnitine metabolites in livers of the

695 indicated genotype. n=5-6 mice per group at 8 weeks post-AAV administration. **(M)**
696 Relative β-hydroxybutyrate levels in livers of the indicated genotype at 8 weeks post-AAV
697 administration. n=4-5 mice per group. **(N)** Relative glutarate levels in livers of the indicated
698 genotype at 8 weeks post-AAV administration. n=5-6 mice per group. Statistical
699 significance was assessed using t-test (A,B,E,F,H,I,K,L,M,N) or Mann-Whitney (D) tests
700 with adjustments for multiple comparisons. All data represent mean +/- standard deviation
701 from biological replicates.
702
703
704
705
706
707
708
709
710
711
712
713
714
715
716
717

718 **MATERIALS AND METHODS**

719 **Reagents**

720 Most chemicals and reagents including antimycin A (A8674), carbonyl cyanide 3-
721 chlorophenylhydrazone [CCCP (C2759)], EGTA (E3889), glutamate (49621), glycerol
722 (G5516), hematoxylin (GHS132), HEPES (H4034), magnesium chloride (208337), malate
723 (240176), D-mannitol (M4125), NAD^+ (N8285), $NADP^+$ (N8160), NADH (N6785), NADPH
724 (N9960),$^{15}N_5$-AMP (900382), Orotic acid (O2750), L-Dihydroorotic acid (D7128), Oil Red
725 O (O0625), periodic acid (P7875), PEG 400 (91893), potassium chloride (P9541),
726 rotenone (R8875), sodium chloride (S9888), sodium lactate (L7022), sodium phosphate
727 monobasic (RDD007), sodium pyruvate (P2256), sucrose (S0389), N,N,N′,N′-
728 Tetramethyl-p-phenylenediamine [TMPD (T7394)] were purchased from Sigma-Aldrich.
729 HPLC-grade acetonitrile (A955), formic acid (A117), methanol (A456), and water (W6)
730 were purchased from Fisher Scientific. Eosin Y (SE23) and Tris base (BP301) was
731 purchased from Fisher Scientific. GSH (G597951), GSSG (G597970), $^{13}C_2$;^{15}N GSH
732 (G597952), and $^{13}C_4$;$^{15}N_2$ GSSG (G597972) were purchased from Toronto Research
733 Chemicals. [U-^{13}C] lactate (CLM-1579) and [U-^{13}C] pyruvate (CLM-2440) were purchased
734 from Cambridge Isotope Laboratories. Schiff's Reagent was purchased from Electron
735 Microscopy Sciences (26052-06). pAAV.TBG.PI.eGFP.WPRE.bGH (AAV-GFP) and
736 pAAV.TBG.PI.Cre.rBG (AAV-Cre) were a gift from James M. Wilson (Addgene viral prep
737 #105535-AAV8 and #107787-AAV8). Antibodies used: Tom20 (Proteintech, 11802),
738 Pyruvate carboxylase (Proteintech, 16588), Actin (Proteintech, 66009), Ndufa9
739 (ThermoScientific, 459100), β2-microgobulin (ThermoScientific, 701250).

740

741 **Mice**

742 The *cox10*$^{f/f}$ mice (strain 024697) were purchased from The Jackson Laboratory and were
743 maintained on a C57BL6 background. The *ndufa9*$^{f/f}$ mice were obtained from David
744 McFadden (UT Southwestern) and were on a C57BL6 background; generation of these
745 mice are described here (*55*). All mice were housed in the Animal Resource Center at
746 University of Texas Southwestern Medical Center under a 12-hour light-dark cycle and
747 fed ad libitum. Prior to all experiments, mice were fasted for 16-18 hours over night
748 (unless otherwise indicated). All mouse experiments were performed according to
749 protocols approved by the Institutional Animal Care and Use Committee (IACUC) at
750 University of Texas Southwestern Medical Center. Both male and female mice were used
751 in all experiments; if sex differences were not present, both male and female mice were
752 analyzed together. For genotyping, the following primers were used:

753 *Cox10* Forward: GAGAGGAGTCAAGGGGACCT

754 *Cox10* Reverse: GGCCTGCAGCTCAAAGTGTA

755 *Ndufa9* Forward: TTGATTGCCTGTGAGCTTTG

756 *Ndufa9* Reverse: TGCTAGGAAAGAGGCAGGTC

757 For AAV injections, virus was prepared in dilution buffer [NaCl (136mM), KCl (5mM),
758 MgCl2 (1mM), Tris (10mM, pH 7.4), and glycerol (10%)] and injected into the retroorbital
759 vein at $5x10^{10}$ GC per mouse.

760

761 **Mitochondrial ETC Activity Measurements**

762 Oxygen consumption rates (OCR) were measured using a Seahorse XFe96 Analyzer
763 (Agilent Technologies) based on a previously published protocol (*56*). Liver tissue was

764 homogenized with 40 strokes of a dounce homogenizer in mitochondrial isolation buffer
765 [HEPES (5mM), sucrose (70mM), mannitol (220mM), MgCl2 (5mM), KH2PO4 (10mM),
766 and EGTA (1mM), pH 7.2]. Mitochondria were isolated via differential centrifugation: First
767 nuclei and cell debris were removed by isolating supernatant after five spins at 600g; and
768 enriched mitochondria were then pelleted with a 10000g spin. 5μg of mitochondria were
769 plated in an XFe96 well plate on ice, spun at 4700 RPM (Beckman Coulter S6096) for 2
770 minutes at 4°C. Mitochondria were then supplemented with media containing isolation
771 buffer with complex IV substrates to probe respiration. At the times indicated, ADP (final
772 concentration 4mM), oligomycin (2uM), CCCP (2uM), and either antimycin A (4uM) or
773 sodium azide (40mM) was injected.

No substrate	Isolation buffer (IB)
Complex IV	IB with ascorbate (10mM) + TMPD (100uM) + antimycin A (2uM)

774

775 For mouse embryonic fibroblast experiments, *ndufa9*$^{f/f}$ and *ndufa9*$^{-/-}$ MEFS were obtained
776 as previously described (*55*). Briefly, E13.5 embryos were collected from *ndufa9*$^{f/f}$
777 pregnant females, minced and digested with trypsin for 45 min at 37C. Digested embryos
778 were cultured in DMEM (Sigma-Aldrich, D6429) supplemented with 10%FBS, 1%
779 penicillin/streptomycin, and immortalized with a lentiCRISPRv2 lentivirus expressing
780 sgRNA targeting Trp53. Immortalized MEFs were subsequently transduced with Ad5-
781 CMV-EGFP or Ad5-CMV-CreEGP adenovirus (University of Iowa Viral Vector Core),
782 followed by culturing in the above media supplemented with 1mM sodium pyruvate and
783 100 μg/ml uridine. GFP+ cells were sorted by flow-cytometry to obtain purified *ndufa9*$^{f/f}$
784 and *ndufa9*$^{-/-}$ cells, which were then verified by genotyping and Western blot analysis, as

785 previously reported (*55*). For oxygen consumption measurements, *ndufa9*$^{f/f}$ and *ndufa9*$^{-/-}$
786 cells were plated overnight and exchanged into Seahorse assay buffer and
787 measurements started. Mitochondrial oxygen consumption rates (mito-OCR) were
788 calculated by subtracting non-mitochondrial respiration from baseline respiration.
789 Complex I activity measurements were performed using an immunocapture absorbance
790 assay (ab109721; Abcam) following manufacturer's instructions. Approximately 100 mg
791 of tissue were isolated from snap frozen mouse livers that had been stored at -80˚C.
792 Tissue was homogenized in 500 ul PBS and protein concentrations were quantitated (DC
793 Protein assay, Biorad). Samples were diluted with PBS to a concentration of 5.5 mg/ml
794 and 90 ul were mixed with 10 ul of detergent (Abcam) and incubated on ice for 30 minutes.
795 Samples were then spun down at 17,000 x g and 4˚C and the supernatants were collected
796 and diluted to 250 ug/mL of protein. 50 ug of each sample were loaded in duplicate onto
797 the immunocapture plate and incubated for 3 hours. Experimental wells were then
798 washed three times before adding 200 uL of reaction mixture. The OD450 was monitored
799 over 30 minutes (SpectraMax), and the resulting reaction curves were fit by linear
800 regression (Prism Graphpad) and slopes reflecting Complex I activity are reported by as
801 mOD 450/ug protein/min.
802 ATP measurements were carried out with an ATP Colorimetric/Fluorometric assay kit (K-
803 354, BioVision Inc.). Approximately 10 mg of tissue were isolated from snap frozen mouse
804 livers that had been stored at -80˚C. Tissues were homogenized in 100 ul of ATP assay
805 buffer and were rapidly deproteinized by PCA precipitation (K-808, BioVision Inc.). 10 ul
806 of deproteinized sample were diluted with 40 ul of ATP assay buffer and loaded in
807 duplicate into a clear bottom 96 well plate. 50 ul of developer solution was added to each

808 well and the plate was incubated for 30 minutes at room temperature protected from light.
809 The endpoint OD570 of sample wells was measured on a Spectramax iD3 spectrometer
810 (SpectraMax, Molecular Devices) and the total amount of ATP was determined from a
811 standard curve constructed with 0–10 nmol ATP. Reported values are normalized by
812 tissue weight.
813

814 **qRT-PCR and qPCR measurements.**

815 Genomic DNA was isolated by ethanol precipitation and RNA was isolated from tissue
816 using RNeasy Mini kits (Qiagen). Samples were run using the Luna Universal One-Step
817 RT-qPCR Kit (New England Biolabs) on a CFX384 (Bio-Rad).

Target	Primer Sequence
cox10	F: AGGGTCAGCATCACCAATAC
	R: GGAGACACTTACCAGCATCAA
ndufa9	F: GGAGACACTTACCAGCATCAA
	R: CCTCCTTTCCCGTGAGGTA
mtDNA (*ND2* mtDNA)	F: CCTATCACCCTTGCCATCAT
	R: GAGGCTGTTGCTTGTGTGAC
nDNA (*pecam1*)	F: ATGGAAAGCCTGCCATCATG
	R: TCCTTGTTGTTCAGCATCAC

818

819 **Histology of liver tissue**

820 Fresh tissue was fixed overnight in 10% neutral buffered formalin, rinsed with 30%
821 sucrose in PBS, and paraffin embedded. 10 micron sections were cut and placed on

822 slides at -20°C until staining. Sections were stained by either haemotoxylin and eosin, Oil
823 Red O), or periodic acid Schiff base (PAS) and visualized under 20X magnification on an
824 Olympus IX83 microscope and processed with ImageJ (NIH).
825
826 **Plasma Analysis**
827 Blood was collected on ice with heparin and centrifuged at 5000xg for 10 minutes to obtain
828 plasma. Plasma levels of alanine aminotransferase, albumin, aspartate
829 aminotransferase, glucose, lactate, total bilirubin, and total protein were measured using
830 a VITROS 250 Microslide at the UT Southwestern Metabolic Phenotyping Core.
831
832 **GSH/GSSG and NAD(P)(H) Quantitation**
833 For glutathione quantitation, 20mg of frozen tissue was treated with 300uL of 80%
834 methanol with 0.1% formic acid and homogenized on ice. The samples were freeze-
835 thawed, centrifuged to remove protein, and the supernatant was dried. Dried samples
836 were reconstituted in 1mL water with 0.1% formic acid, diluted, spiked with internal
837 labeled standards, and analyzed as previously described (*57, 58*).
838 NAD(P)+/NAD(P)H was measured as previously described (*59*). Briefly, ~20 mg of tissue
839 was homogenized on ice in cold 40:40:20 (acetonitrile: methanol: water) with 0.1M formic
840 acid buffer. Tissue was vortexed, chilled, quenched with 15% ammonium bicarbonate,
841 and centrifuged to pellet protein. Supernatant was diluted in 10mM ammonium
842 bicarbonate and $^{15}N_5$-AMP was added as an internal standard and injected onto a Sciex
843 6500 Qtrap using a reverse-phase ion pairing method**.** Pelleted protein was lysed and
844 quantified using the DC protein assay (Bio-Rad).

845 For MEFs, cells were plated in 6-well dishes and allowed to adhere overnight; the
846 following day cells were at ~80% confluence. Media was removed, cells were rinsed with
847 ice cold saline, and metabolites were collected by scraping cells in dry ice-cold 80%
848 methanol / 20% water with an internal standard (series of 13C, 15N-labeled amino acids).
849 Metabolite extracts were stored at -80°C overnight and centrifuged the following day to
850 remove debris. Raw AUC values were obtained using MultiQuant and TIC values for
851 normalization were obtained using Analyst (SCIEX software for MS analysis).
852
853 **Proteomics analysis of liver tissue**
854 50 μg per sample of protein homogenate from livers or enriched mitochondria (prepared
855 as described above) was solubilized in 1% SDS, 50mM Tris pH 8.0, loaded onto a 4-20%
856 Mini-PROTEAN TGX precast protein gel (BioRad), stained with Coomassie Blue, and
857 destained. Samples were analyzed at the UT Southwestern Proteomics Core. Gel slices
858 were cut into 1mm3 cubes, and digested overnight with trypsin (Pierce 90058) following
859 reduction and alkylation with DTT and iodoacetamide (Sigma–Aldrich I6125). The
860 samples then underwent solid-phase extraction cleanup with an Oasis HLB plate (Waters)
861 and the resulting samples were injected onto an Orbitrap Fusion Lumos mass
862 spectrometer coupled to an Ultimate 3000 RSLC-Nano liquid chromatography system.
863 Samples were injected onto a 75 μm i.d., 75-cm long EasySpray column (Thermo) and
864 eluted with a gradient from 0-28% buffer B over 90 min. Buffer A contained 2% (v/v) ACN
865 and 0.1% formic acid in water, and buffer B contained 80% (v/v) ACN, 10% (v/v)
866 trifluoroethanol, and 0.1% formic acid in water. The mass spectrometer operated in
867 positive ion mode with a source voltage of 1.8 kV and an ion transfer tube temperature of

868 275 °C. MS scans were acquired at 120,000 resolution in the Orbitrap and up to 10
869 MS/MS spectra were obtained in the ion trap for each full spectrum acquired using higher-
870 energy collisional dissociation (HCD) for ions with charges 2-7. Dynamic exclusion was
871 set for 25 s after an ion was selected for fragmentation.
872 Raw MS data files were analyzed using Proteome Discoverer v2.4 SP1 (Thermo), with
873 peptide identification performed using Sequest HT searching against the mouse protein
874 database from UniProt (downloaded January 2022; 17,062 sequences). Fragment and
875 precursor tolerances of 10 ppm and 0.6 Da were specified, and three missed cleavages
876 were allowed. Carbamidomethylation of Cys was set as a fixed modification, with
877 oxidation of Met set as a variable modification. The false-discovery rate (FDR) cutoff was
878 1% for all peptides. PSMs found in only a subset of samples were re-searched to identify
879 peptides based on retention time and mass. Protein abundance was quantitated based
880 on the total ion count for all identified peptides in each sample, and normalized after log
881 transform according to previously published protocols (*60*). Unsupervised hierartchical
882 clustering was performed on z-score transformed values in MATLAB (Mathworks, Inc.).
883 Mitochondrial-localized proteins were classified based on their presence in MitoCarta3.0
884 (*61*). Significantly up and downregulated proteins were identified based on $\log_2$(fold
885 change) <1 or <1 (respectively) and p-value<0.05. Gene ontology analysis on up or
886 downregulated proteins was performed using DAVID (https://david-
887 d.ncifcrf.gov/home.jsp); for each analysis, the complete list of detected proteins was used
888 as a background, and pathways from Biological Processes, Cellular Components and
889 Molecular Function (All and Direct) were assessed. Pathways with a FDR<0.05 are
890 reported in Table S2. Gene set enrichment analysis was performed using GSEA software

891 (*62, 63*) using the following gene-ontology pathways: GO:0006633 (Fatty Acid Synthesis),
892 GO:0019395 (Fatty Acid Oxidation), GO:0008206 (Bile Acid Metabolic Process),
893 GO:0016491 (Oxidoreductase Activity).
894
895 **In vivo isotope tracing**
896 All *in vivo* isotope tracing experiments were performed in conscious mice after overnight
897 fasting, based on previously published protocols (*64, 65*). On the morning of the
898 experiment, catheters (Braintree Scientific MRE-KIT 025) were surgically implanted into
899 the right external jugular vein of mice. For steady state euglycemic infusion of [U-
900 ^{13}C]glucose, a total dose of 8g/kg body mass (dissolved in 1000 μl saline) was
901 continuously infused at 2.5 μl min^{-1} (total infusion time of 3 hr). At the end of the infusion,
902 mice were euthanized and tissue was immediately harvested, snap frozen in liquid N2,
903 and stored at -80°C prior to GC-MS analysis.
904
905 **Metabolomics analysis**
906 Flash frozen liver tissue (20 mg) was pulverized with a mortar and pestle on liquid nitrogen
907 (H37260-0100, Bel-Art Products), 80% methanol was added, and samples subjected to
908 three freeze-thaw cycles. For plasma, 20 μL was extracted with 0.2 mL cold acetone.
909 Protein was removed by centrifugation and supernatant dried (SpeedVac,
910 ThermoFisher).
911 Data acquisition was performed by reverse-phase chromatography on a 1290 UHPLC
912 liquid chromatography (LC) system interfaced to a high-resolution mass spectrometry
913 (HRMS) 6550 iFunnel Q-TOF mass spectrometer (MS) (Agilent Technologies, CA). The

914 MS was operated in both positive and negative (ESI+ and ESI-) modes. Analytes were
915 separated on an Acquity UPLC® HSS T3 column (1.8 µm, 2.1 x 150 mm, Waters, MA).
916 The column was kept at room temperature. Mobile phase A composition was 0.1% formic
917 acid in water and mobile phase B composition was 0.1% formic acid in 100% ACN. The
918 LC gradient was 0 min: 1% B; 5 min: 5% B; 15 min: 99% B; 23 min: 99% B; 24 min: 1%
919 B; 25 min: 1% B. The flow rate was 250 µL min-1. The sample injection volume was 5 µL.
920 ESI source conditions were set as follows: dry gas temperature 225 °C and flow 18 L min-
921 1, fragmentor voltage 175 V, sheath gas temperature 350 °C and flow 12 L min-1, nozzle
922 voltage 500 V, and capillary voltage +3500 V in positive mode and −3500 V in negative.
923 The instrument was set to acquire over the full m/z range of 40–1700 in both modes, with
924 the MS acquisition rate of 1 spectrum s-1 in profile format. Raw data files were processed
925 using Profinder B.08.00 SP3 software (Agilent Technologies, CA) with an in-house
926 database containing retention time and accurate mass information on 600 standards from
927 Mass Spectrometry Metabolite Library (IROA Technologies, MA) which was created
928 under the same analysis conditions. The in-house database matching parameters were
929 mass tolerance 10 ppm; retention time tolerance 0.5 min. Peak integration result was
930 manually curated in Profinder for improved consistency. Metabolite abundances were
931 normalized based on the total ion count for all identified metabolites. Unsupervised
932 hierartchical clustering was performed on z-score transformed values in MATLAB
933 (Mathworks, Inc.), and adjusted p-values were calculated using multiple t-test with adjust
934 for multiple comparisons in Graphpad Prism.
935 GC-MS analysis was used to quantitate α-hydroxybutyrate and α-ketobutyrate, as well
936 as measure mass isotopomer distributions for the lactate/pyruvate tolerance test and [U-

937 ^{13}C]glucose infusions. Dried metabolites were derivatized to form methoxime-TBDMS
938 adducts by incubating with 1% methoxyamine hydrochloride (Sigma-Aldrich) in pyridine
939 at 70°C for 15 min followed by addition of *N-tert*-Butyldimethylsiyl-*N*-
940 methyltrifluoroacetamide (MTBSTFA, Sigma-Aldrich) for 1 hour. Derivatized samples
941 were analyzed using an Agilent Technologies 7890B gas chromatographer with a HP-
942 5MS 5% phenyl methyl Silox column (Agilent) coupled to an Agilent Technologies 5977A
943 mass spectrometer. The observed distributions of mass isotopologues were corrected for
944 natural abundance (*66*).
945

946 **Lactate/Pyruvate Tolerance Test**

947 Lactate/Pyruvate tolerance tests were performed as previously described (*29*). Briefly,
948 mice were fasted for 16 hours overnight and given an IP injection of a 1.5mg/g of a 10:1
949 sodium lactate: sodium pyruvate solution. 40% of the sodium lactate and sodium pyruvate
950 were [U-^{13}C] sodium lactate and [U-^{13}C] sodium pyruvate. Blood glucose was measured
951 0, 10, 20, and 30 minutes post injection using a blood glucometer (Contour Next) and
952 lactate was measured using a lactate meter (Nova Biomedical Lactate Plus). Fractional
953 gluconeogenesis (GNG) was determined as previously described (*67*), using the following
954 formula:

955 $$GNG = (M1_{glucose} + M2_{glucose} + M3_{glucose})/(2*M0_{lactate}*(M1_{lactate} + M2_{lactate} + M3_{lactate}))$$

956 where Mx represents the fractional enrichment of the m+x species for the indicated
957 metabolite.
958

959 **Magnetic Resonance Imaging experiments**

960 Experiments were performed on mice at 4 weeks post-AAV administration. MR imaging
961 was performed on a 7T pre-clinical scanner (Bruker Biospec, Germany) using a 40 mm
962 Millipede radio frequency coil for transmitting and receiving. Mice were anesthetized with
963 1.5-2.5% Isoflurane. Mice breathed medical air (21% O2) delivered via a nose cone, in
964 the baseline acquisition and then the gas was switched to 100% O2 (Airgas, Radnor
965 Township, PA, USA). The gas flow rate was set to 400 ml/min. A pneumonic sensor
966 placed on the abdomen was used for respiratory monitoring and prospective triggering
967 (SA Instruments, Stony Brook, NY). The animal's ambient temperature was maintained
968 at 28 °C using an MR Compatible Small Rodent Air Heater System (SA Instruments,
969 Stony Brook, NY). For a given animal, the breathing rate was maintained at 40 $\pm$ 5 bpm
970 by varying the Isoflurane levels by $\pm$ 0.5%. At each breathing challenge, images were
971 acquired to generate T1 and T2* maps of the liver in the coronal plane.
972 **T1 method**: A respiratory triggered, radio frequency spoiled, flow compensated cine
973 gradient echo method (FLASH) was used. To suppress the motion artifacts from cardiac
974 motion, a saturation pulse was applied to the thoracic region. Two cines (number of
975 frames = 65) were acquired with two different flip angles (α = 5° and 20°). A steady state
976 signal was achieved after 55 frames. Frames 55 to 65 were averaged to improve the
977 signal-to-noise ratio. Pixel-by-pixel apparent (uncorrected for B1 inhomogeneity) T1
978 maps were calculated using the averaged signal intensities (S) according to (*68*), $S\alpha =$
979 $-2\frac{TR}{T1}\left(\frac{S}{\alpha}\right) + const$. Cine FLASH parameters were: TR/TE=10ms/2.3ms, FOV = 40 x 40
980 mm^2, matrix = 128 x 128, NEX = 1, slice thickness = 1 mm, number of segments = 1,
981 number of frames = 65, in-plane resolution = 0.3 mm x 0.3 mm.

982 Using the apparent T1 maps, and noting that any spatial dependencies due to B1
983 inhomogeneity are canceled out in relative measures, a map of the actual T1 difference
984 between the gas challenges (Air vs. 100 %O2) was calculated as: $\Delta T1 = 100 * (T1_{O2} -$
985 $T1_{air})/T1_{air}$. The mean relative $\Delta T1$ of the liver was calculated in a manually segmented
986 liver region. Pixels representing blood vessels were automatically excluded from this
987 region by thresholding to mean of liver T1 tissue ± 2× standard deviations. The mean of
988 liver T1 was calculated from a region of interest that did not include blood vessels.
989 **T2* method**: A respiratory triggered, bipolar-multi gradient echo (MGE) sequence was
990 used. Sixteen echoes from positive gradients were acquired at 2.5ms intervals. The scan
991 plane geometry and the orientation was identical to that of the T1 method. MGE
992 parameters were: TR = 300 ms, TE = 2.5 ms – 47.5 ms, NEX = 4. T2* maps were
993 generated by non-linear least square fitting the echo signals (s) to an exponential model:
994 $A * e^{-B*TE} + C$. The mean relative $\Delta T2^*$ was calculated as similar to $\Delta T1$.
995 **Perfusion Method:** FAIR arterial spin labeling technique was used to calculate the liver
996 perfusion in a single-slice in the axial plane during the session where mice breathed
997 medical air (21% O2). The FAIR sequence was a multi-echo spin-echo with a 13.6 ms
998 inversion pulse. A slice select inversion with an inversion slab of 4 mm was followed by a
999 global inversion. The inversion time was set to 2000 ms. A reference image was acquired
1000 without the inversion pulse. Other imaging parameter were: TR = 10 s, FOV = 30 x 25
1001 mm^2, matrix = 128 x 64, NEX = 1, slice thickness = 1 mm, echo train length = 8. A pixel
1002 wise perfusion map was constructed as described previously (*31*).
1003
1004 **Statistical analyses**

1005 All data represent mean and standard deviations from biological replicates. No statistical
1006 tests were used to predetermine sample size. Animals were randomly allocated into
1007 experimental groups. No blinding or masking of samples was performed. Data sets for
1008 each group of measurement was tested for normality using the Shapiro-Wilk test. If the
1009 data was not normally distributed, the data was log-transformed and retested for
1010 normality. For normally-distributed data, groups were compared using the two-tailed
1011 Student's t-test (for 2 groups), or one-way ANOVA or two-way ANOVA (> 2 groups),
1012 followed by Tukey's or Dunnett's test for multiple comparisons. For data that was not
1013 normally distributed, we used non-parametric testing (Mann-Whitney or Kolmogorov-
1014 Smirnov tests for two groups and Kruskal-Wallis test for multiple groups), followed by
1015 Dunn's multiple comparisons adjustment. For metabolomics and proteomics data sets,
1016 abundances were compared by multiple t-tests, followed by Bonferroni correction of p-
1017 values. Proteomics and metabolomics analysis were performed once using biological
1018 replicates (individual mice); for other experiments, multiple (two to four) independent
1019 experiments with biological replicates (individual mice) were performed for reported data,
1020 and the number of biological replicates are indicated in the figures. No data were
1021 excluded.
1022
1023
1024
1025
1026
1027

1028 **Captions for Supplementary Tables:**

1029

1030 **Table S1**

1031 Excel spreadsheet containing raw data and statistical analysis of proteomics and

1032 metabolomics data for *ndufa9*$^{-/-}$ vs. *ndufa9*$^{f/f}$ livers at 4 weeks post-AAV administration.

1033

1034 **Table S2**

1035 Excel spreadsheet containing raw data and statistical analysis of proteomics and

1036 metabolomics data for *cox10*$^{-/-}$ vs. *cox10*$^{f/f}$ livers at 8 weeks post-AAV administration.

1037

1038

1039

1040

1041

1042

1043

1044

1045

1046

1047

1048

1049

1050

Figure 1 - figure supplement 1

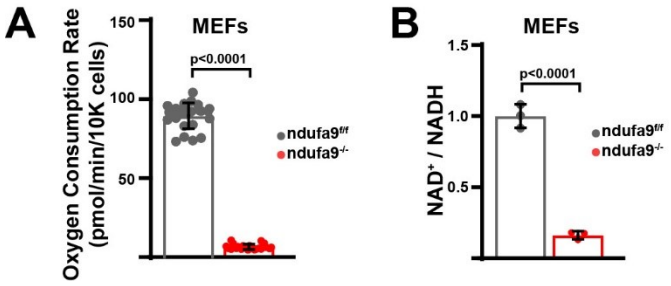

1051 **Figure 1 – figure supplement 1. Metabolic Flux Analysis of *ndufa9$^{f/f}$* and *ndufa9$^{-/-}$***

1052 **MEFs. (A)** Oxygen consumption rates in *ndufa9$^{f/f}$* and *ndufa9$^{-/-}$* mouse embryonic

1053 fibroblasts (MEFs). n = 22-24 wells per group. The same color scheme is used throughout

1054 this figure. **(B)** Normalized NAD^+ / NADH ratios in MEFs of the indicated genotype. n=3

1055 wells per group.

1056

1057

1058

1059

1060

1061

1062

1063

1064

1065

1066

1067

1068

1069

Figure 1 - figure supplement 2

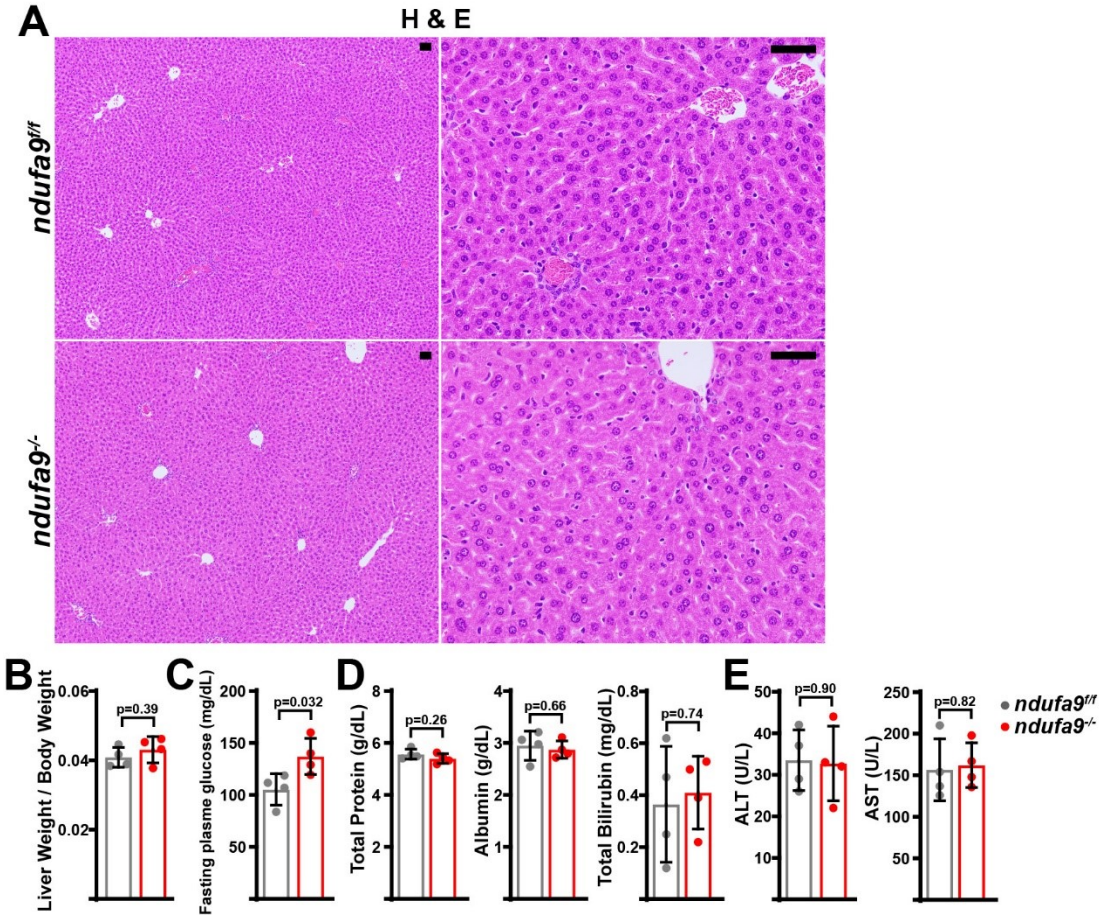

Figure 1 – figure supplement 2. Analysis of *ndufa9*$^{-/-}$ livers at 2 weeks post-AAV administration. (A) Representative histology (H&E, Oil Red O, PAS staining) images of liver cross sections from animals of the indicated genotype at two weeks post-AAV administration. Scale bar: 50μm. **(B)** Liver weight / body weight ratios in animals of the indicated genotype. n=4 mice per group. The same color scheme is used throughout this figure. **(C)** Fasting plasma glucose levels in mice of the indicated genotype. n=4 mice per group. **(D)** Circulating plasma markers (total protein, albumin, and total bilirubin) of liver function in mice of the indicated genotype. n=4 animals per group. **(E)** Plasma markers (ALT and AST levels) of liver damage in mice of the indicated genotype. n=4 mice per

1080 group. Statistical significance was assessed using two-tailed t-test (B,C,D,E). All data in
1081 this figure were collected at 2 weeks post AAV-administration. All data represent mean
1082 +/- standard deviation from biological replicates, unless noted otherwise.
1083
1084
1085
1086
1087
1088
1089
1090
1091
1092
1093
1094
1095
1096
1097
1098
1099
1100
1101
1102

Figure 1 - figure supplement 3

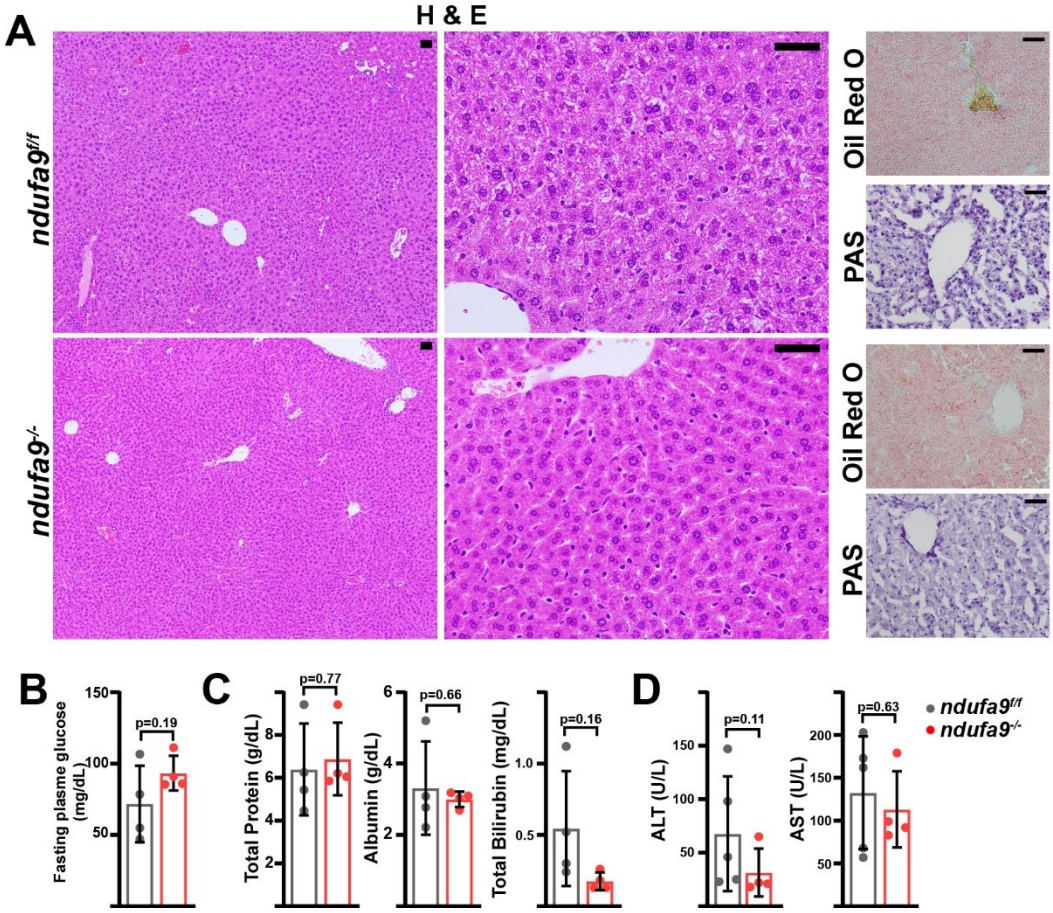

Figure 1 – figure supplement 3. Analysis of ndufa9-/- livers at 8 weeks post-AAV administration. (A) Representative histology (H&E, Oil Red O, PAS staining) images of liver cross sections from animals of the indicated genotype at eight weeks post-AAV administration. Scale bar: 50μm. **(B)** Fasting plasma glucose levels in mice of the indicated genotype. n=4 mice per group. The same color scheme is used throughout this figure. **(C)** Circulating plasma markers (total protein, albumin, and total bilirubin) of liver function in mice of the indicated genotype. n=4 animals per group. **(D)** Plasma markers (ALT and AST levels) of liver damage in mice of the indicated genotype. n=4 mice per group. All data in this figure were collected at 8 weeks post AAV-administration. Statistical

1113 significance was assessed using two-tailed t-test (B,C,D). All data represent mean +/-
1114 standard deviation from biological replicates.
1115
1116
1117
1118
1119
1120
1121
1122
1123
1124
1125
1126
1127
1128
1129
1130
1131
1132
1133
1134
1135

Figure 2 - figure supplement 1

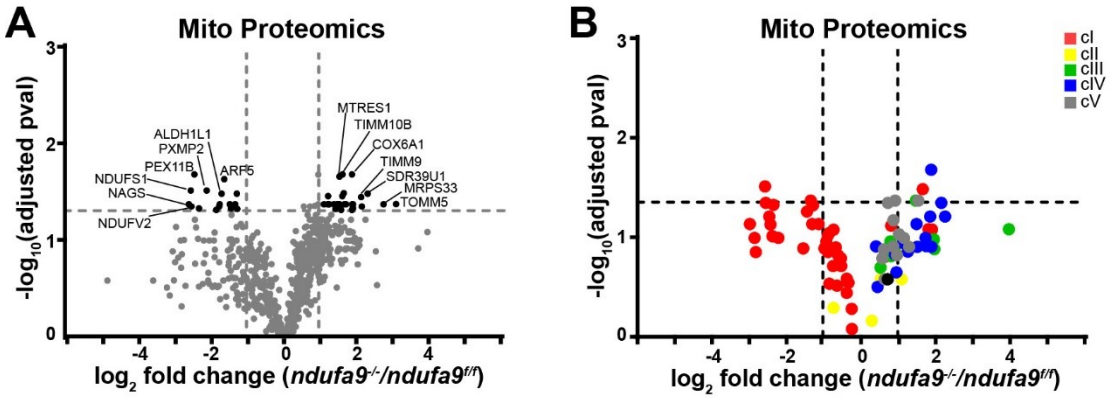

Figure 2 – figure supplement 1. Analysis of mitochondrial proteomes in complex I deficient livers. (A) Volcano plot of protein abundances changes in *ndufa9*$^{-/-}$ vs. *ndufa9*$^{f/f}$ livers, based on proteomics analysis of enriched mitochondria. Mitochondrial proteins (based on MitoCarta 3.0) are shown. Log_2(fold change) is plotted against the –log_{10}(adjusted p-value) for each protein. Significantly changing proteins (log_2(fold change) >1 or < -1; Adjusted p-val<0.05) are colored black. n=3 mice per group; 4 weeks post-AAV administration. **(B)** Volcano plot of abundances for mitochondrial ETC proteins in mitochondria purified from *ndufa9*$^{-/-}$ vs. *ndufa9*$^{f/f}$ livers, based on proteomics analysis.

Figure 2 - figure supplement 2

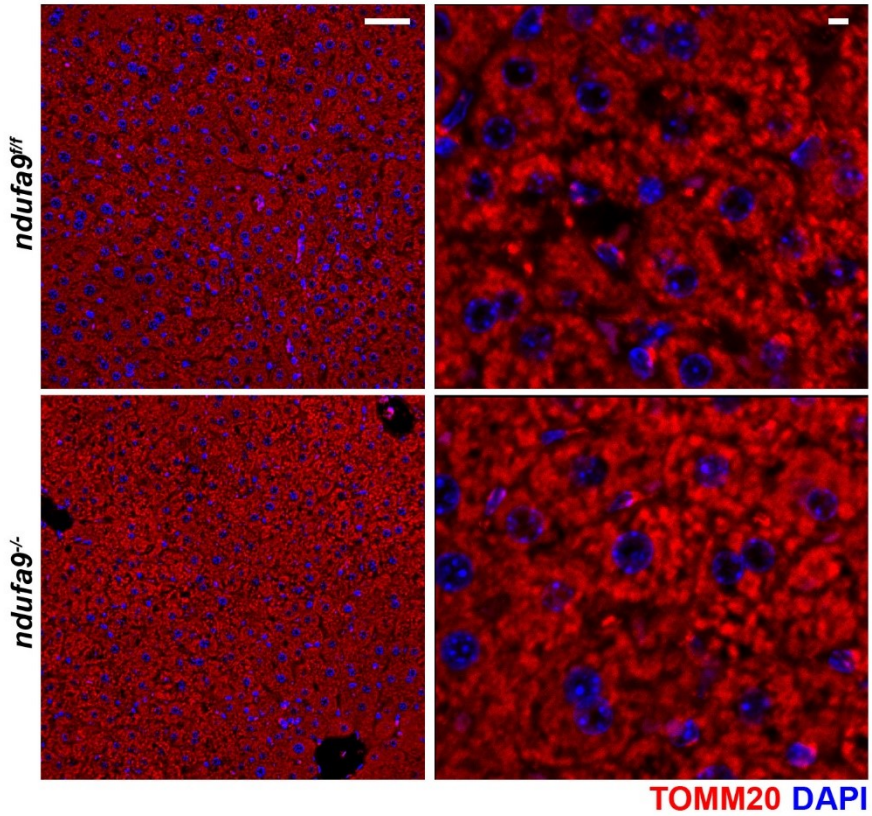

1154

1155 **Figure 2 – figure supplement 2. Immunofluorescence of hepatic sections.**
1156 Representative immunofluorescent images of liver sections at 20x (left; scale bar 50 μm)
1157 and 63x (right; scale bar 5 μm) of the indicated genotype. TOMM20 (mitochondrial)
1158 staining is indicated in red; nuclear staining (DAPI) is indicated in blue. Data was collected
1159 at 4 weeks post-AAV administration.

1160

1161

1162

1163

1164

Figure 3 - figure supplement 1

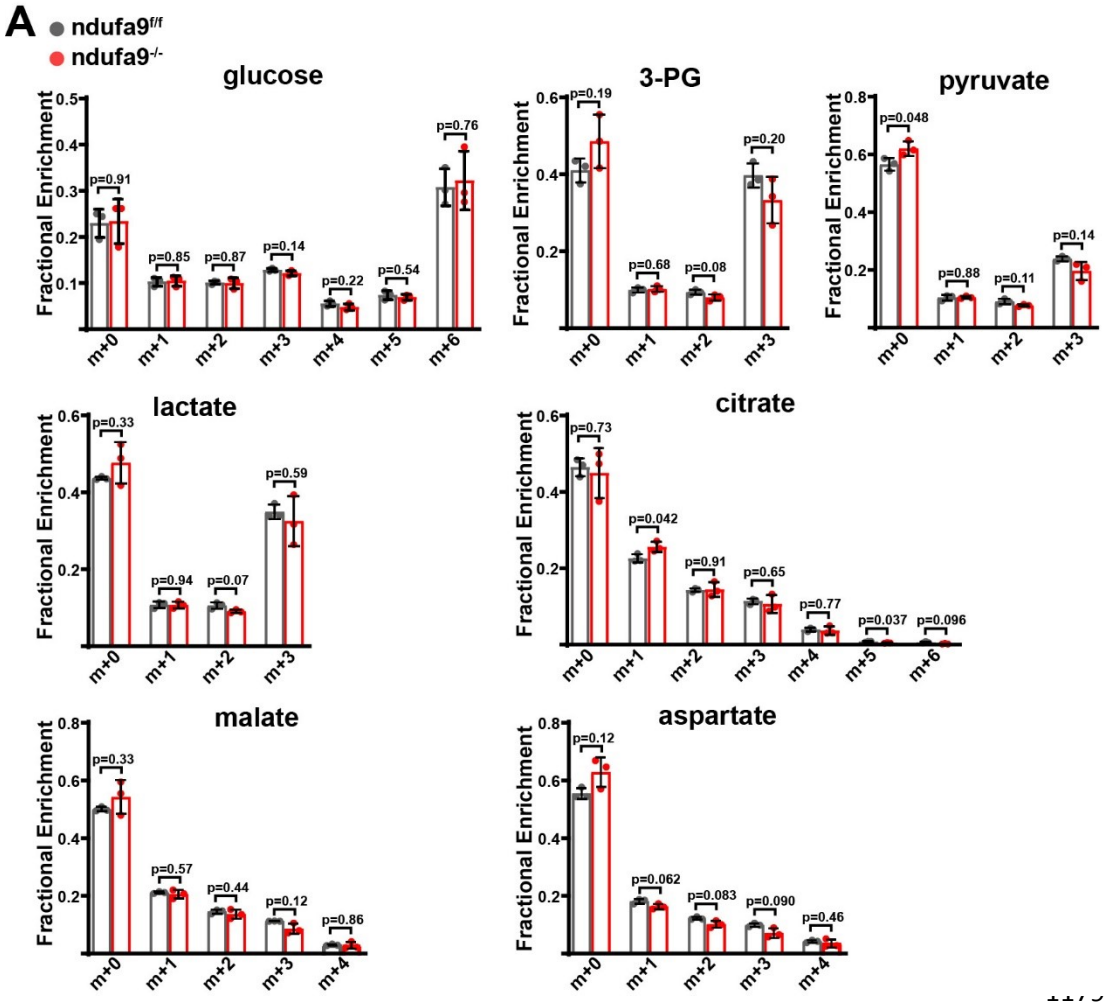

Figure 3 – figure supplement 1. Metabolic analysis of complex I deficient livers. (A) Mass isotopomer distributions in liver tissue from [U-^{13}C]glucose infusions in animals of the indicated genotype. n=3 animals per group; 4 weeks post-AAV administration. Statistical significance was assessed using t-tests (A,B) with adjustments for multiple comparisons. All data represent mean +/- standard deviation from biological replicates.

Figure 4 - figure supplement 1

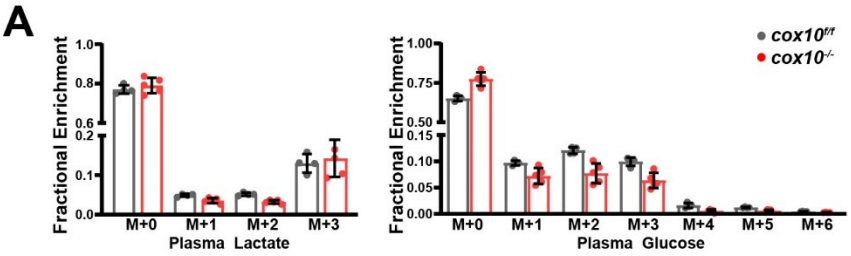

Figure 4 – figure supplement 1. Lactate/pyruvate tolerance test in complex IV deficient livers. (A) Mass isotopomer distributions related to lactate/pyruvate tolerance test (Figure 4H,I), for plasma lactate and glucose. n=4-5 mice per group; 8 weeks post-AAV administration.

Figure 5 - figure supplement 1

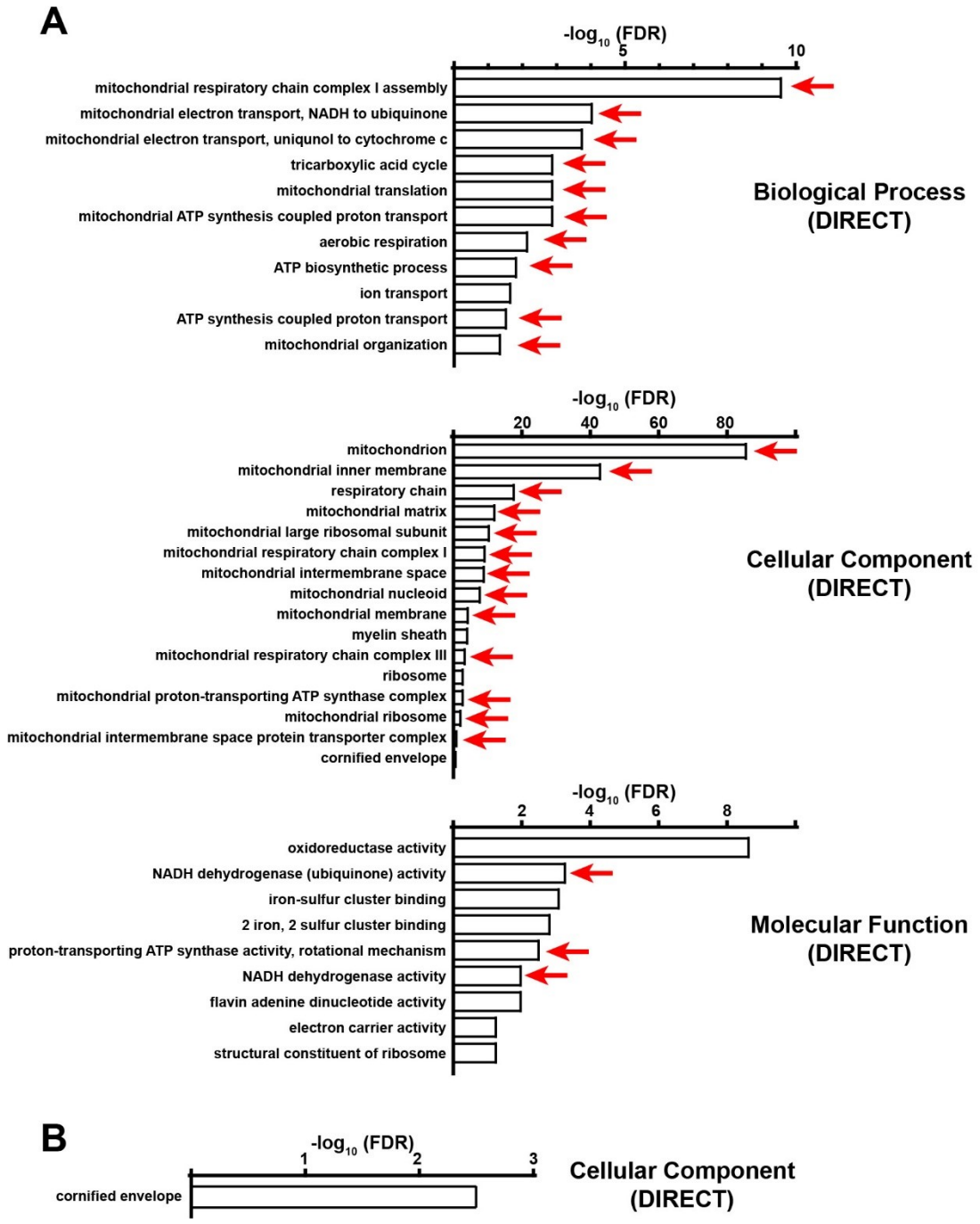

1231 **Figure 5 – figure supplement 1. Functional annotation (DAVID) analysis of**
1232 **upregulated proteins in complex IV deficient livers. (A)** Significantly enriched
1233 biological pathways (FDR<0.05) from gene ontology analysis of all upregulated proteins

1234 ($\log_2$(fold change) > 1; p-value < 0.05) in *cox10*$^{-/-}$ livers, based on proteomic analysis at 8
1235 weeks post-AAV administration. Pathways annotated under Biological Processes
1236 (Direct), Cellular Components (Direct) and Molecular Function (Direct) are shown. Red
1237 arrows highlight pathways related to mitochondrial proteins. **(B)** Same as (A), but for non-
1238 mitochondrial upregulated proteins.
1239
1240
1241
1242

Figure 5 - figure supplement 2

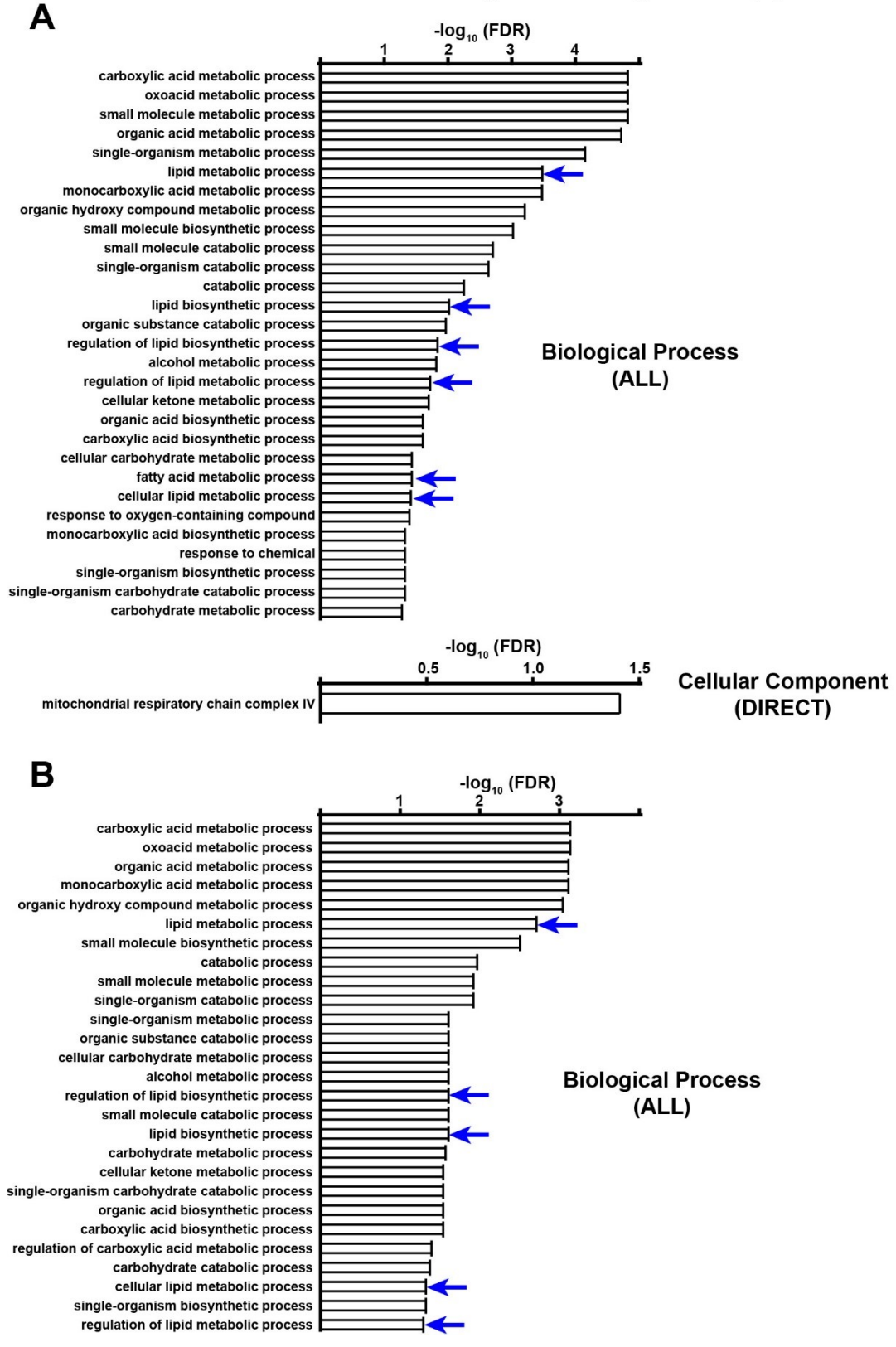

1243

1244 **Figure 5 – figure supplement 2. Functional annotation (DAVID) analysis of**
1245 **downregulated proteins in complex IV deficient livers. (A)** All significantly enriched
1246 biological pathways (FDR<0.05) from gene ontology analysis of all downregulated
1247 proteins ($\log_2$(fold change) < -1; p-value < 0.05) in *cox10*$^{-/-}$ livers, based on proteomic
1248 analysis at 8 weeks post-AAV administration. Blue arrows highlight pathways related to
1249 lipid/fatty acid metabolism. **(B)** Same as (A), but for non-mitochondrial downregulated
1250 proteins.
1251
1252
1253
1254
1255
1256
1257
1258
1259
1260
1261
1262
1263

Figure 5 - figure supplement 3

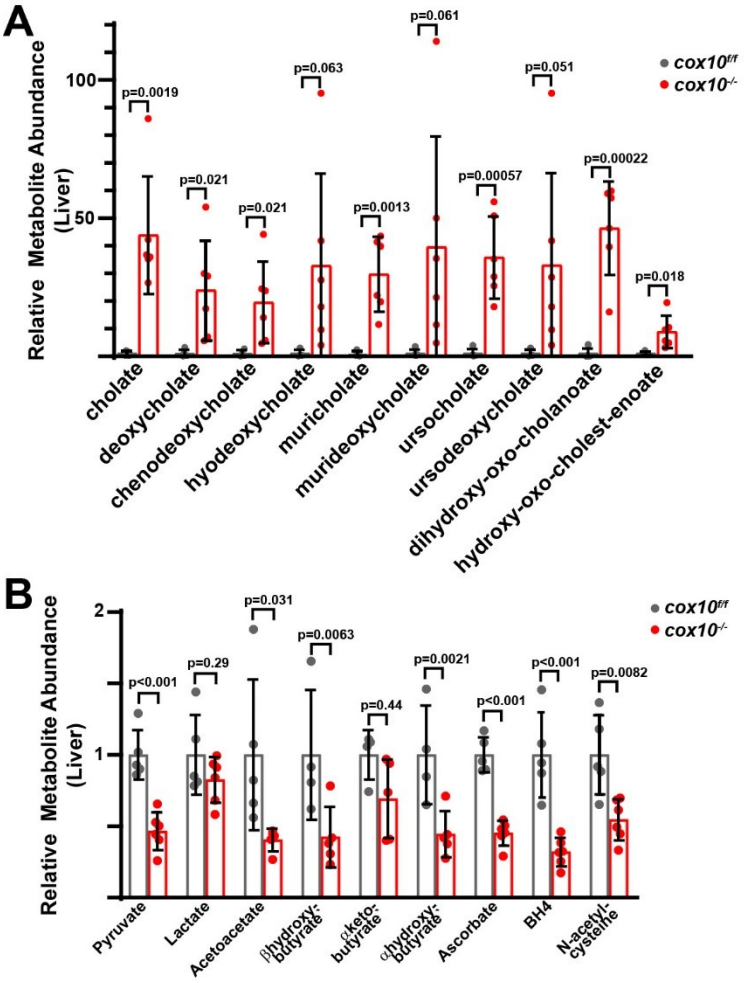

Figure 5 – figure supplement 3. Metabolic analysis of complex IV deficient livers. **(A)** Relative abundance of cholate species in livers of the indicated genotype. n=4-6 mice per group; 8 weeks post-AAV administration. **(B)** Relative abundance of electron acceptors/donors from livers of the indicated genotype. n=4-6 mice per group; 8 weeks post-AAV administration. BH4, tetrahydrobiopterin. Statistical significance was assessed using t-tests (A,B) with adjustments for multiple comparisons. All data represent mean +/- standard deviation from biological replicates.

Figure 5 - figure supplement 4

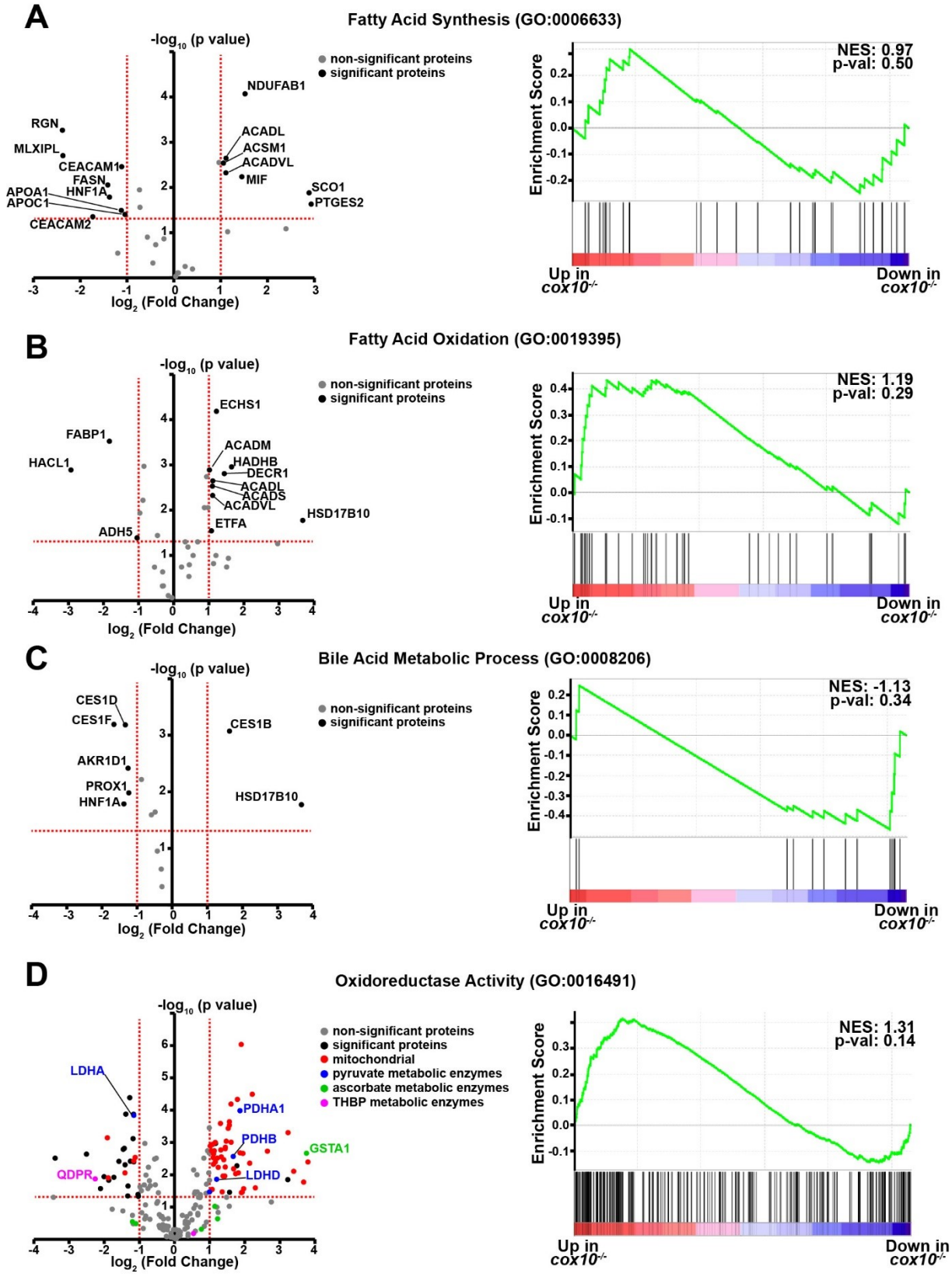

1274

1275 **Figure 5 – figure supplement 4. Metabolic pathway analysis in complex IV deficient**
1276 **livers. (A)** Left, volcano plot of identified proteins from the Fatty Acid Synthesis
1277 (GO:0006633) pathway, based on proteomics performed on *cox10*$^{-/-}$ vs. *cox10*$^{f/f}$ livers at
1278 8 weeks post-AAV administration. Significantly up or downregulated proteins are
1279 indicated in black. Right, GSEA of pathway components; the normalized enrichment
1280 score (NES) and nominal p-value are indicated. **(B)** Same as (A), but for the Fatty Acid
1281 Oxidation (GO:0019395) pathway. **(C)** Same as (A), but for the Bile Acid Metabolic
1282 Process (GO:0008206) pathway. **(D)** Same as (A), but for the Oxidoreductase
1283 (GO:0016491) pathway.
1284
1285
1286
1287
1288
1289
1290
1291
1292
1293
1294
1295
1296
1297

Figure 5 - figure supplement 5

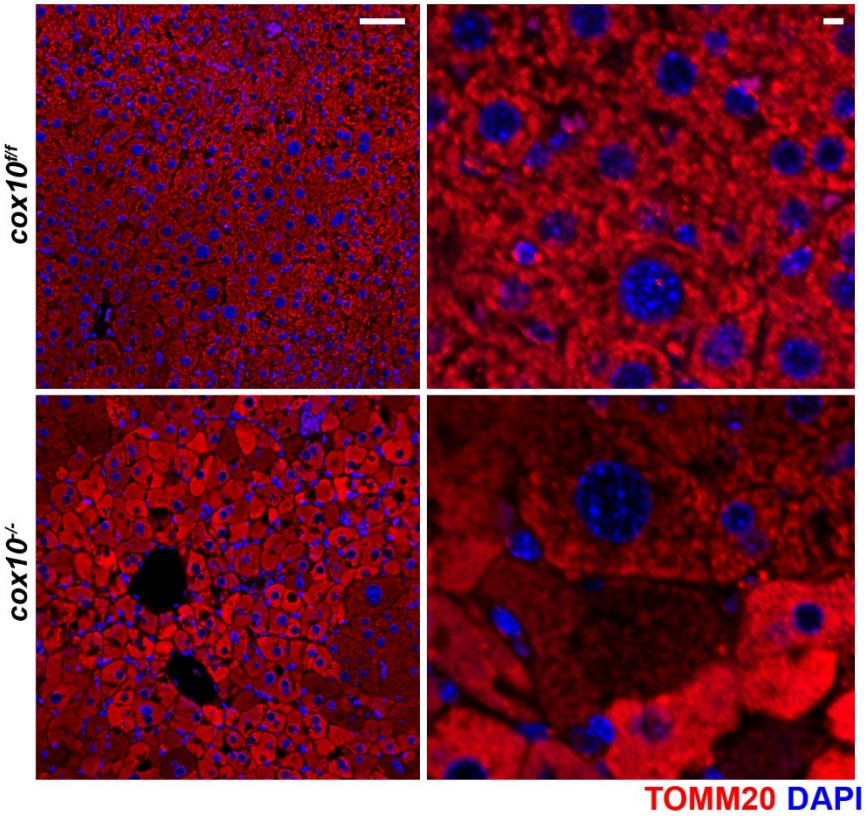

1298

1299 **Figure 5 – figure supplement 5. Immunofluorescence of hepatic sections.**
1300 Representative immunofluorescent images of liver sections at 20x (left; scale bar 50 μm)
1301 and 63x (right; scale bar 5 μm) of the indicated genotype. TOMM20 (mitochondrial)
1302 staining is indicated in red; nuclear staining (DAPI) is indicated in blue. Data was collected
1303 at 8 weeks post-AAV administration.

1304

1305

1306

1307

1308

Figure 6 - figure supplement 1

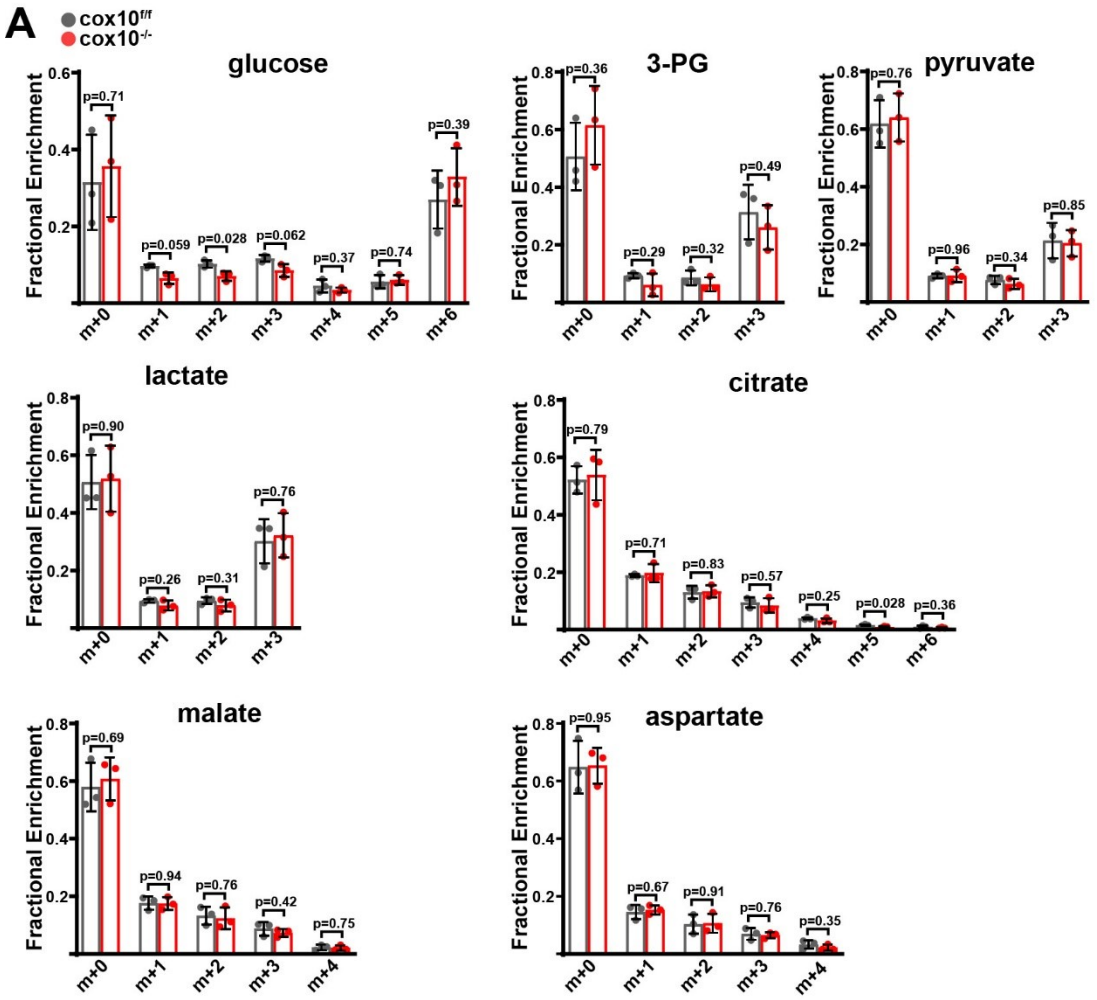

Figure 6 – figure supplement 1. Isotope tracing in complex IV deficient livers. (A) Mass isotopomer distributions in liver tissue from [U-^{13}C]glucose infusions of the indicated genotype. n=3 animals per group; 4 weeks post-AAV administration. Statistical significance was assessed using t-tests (A) with adjustments for multiple comparisons. All data represent mean +/- standard deviation from biological replicates.

1319 **References:**

1320 1. G. S. Gorman, P. F. Chinnery, S. DiMauro, M. Hirano, Y. Koga, R. McFarland, A.
1321 Suomalainen, D. R. Thorburn, M. Zeviani, D. M. Turnbull, Mitochondrial
1322 diseases. *Nature reviews. Disease primers* **2**, 16080 (2016); published online
1323 EpubOct 20 (10.1038/nrdp.2016.80).
1324 2. R. J. Rodenburg, Mitochondrial complex I-linked disease. *Biochimica et*
1325 *biophysica acta* **1857**, 938-945 (2016); published online EpubJul
1326 (10.1016/j.bbabio.2016.02.012).
1327 3. M. A. Martin, A. Blazquez, L. G. Gutierrez-Solana, D. Fernandez-Moreira, P.
1328 Briones, A. L. Andreu, R. Garesse, Y. Campos, J. Arenas, Leigh syndrome
1329 associated with mitochondrial complex I deficiency due to a novel mutation in the
1330 NDUFS1 gene. *Archives of neurology* **62**, 659-661 (2005); published online
1331 EpubApr (10.1001/archneur.62.4.659).
1332 4. F. Distelmaier, W. J. Koopman, L. P. van den Heuvel, R. J. Rodenburg, E.
1333 Mayatepek, P. H. Willems, J. A. Smeitink, Mitochondrial complex I deficiency:
1334 from organelle dysfunction to clinical disease. *Brain : a journal of neurology* **132**,
1335 833-842 (2009); published online EpubApr (10.1093/brain/awp058).
1336 5. S. T. Ahmed, L. Craven, O. M. Russell, D. M. Turnbull, A. E. Vincent, Diagnosis
1337 and Treatment of Mitochondrial Myopathies. *Neurotherapeutics : the journal of*
1338 *the American Society for Experimental NeuroTherapeutics* **15**, 943-953 (2018);
1339 published online EpubOct (10.1007/s13311-018-00674-4).
1340 6. W. S. Lee, R. J. Sokol, Mitochondrial hepatopathies: advances in genetics and
1341 pathogenesis. *Hepatology* **45**, 1555-1565 (2007); published online EpubJun
1342 (10.1002/hep.21710).
1343 7. S. Rahman, Gastrointestinal and hepatic manifestations of mitochondrial
1344 disorders. *Journal of inherited metabolic disease* **36**, 659-673 (2013); published
1345 online EpubJul (10.1007/s10545-013-9614-2).
1346 8. I. Valnot, S. Osmond, N. Gigarel, B. Mehaye, J. Amiel, V. Cormier-Daire, A.
1347 Munnich, J. P. Bonnefont, P. Rustin, A. Rotig, Mutations of the SCO1 gene in
1348 mitochondrial cytochrome c oxidase deficiency with neonatal-onset hepatic

1349 failure and encephalopathy. *American journal of human genetics* **67**, 1104-1109
1350 (2000); published online EpubNov (10.1016/S0002-9297(07)62940-1).
1351 9. J. P. Casey, P. McGettigan, N. Lynam-Lennon, M. McDermott, R. Regan, J.
1352 Conroy, B. Bourke, J. O'Sullivan, E. Crushell, S. Lynch, S. Ennis, Identification of
1353 a mutation in LARS as a novel cause of infantile hepatopathy. *Molecular genetics*
1354 *and metabolism* **106**, 351-358 (2012); published online EpubJul
1355 (10.1016/j.ymgme.2012.04.017).
1356 10. W. S. Lee, R. J. Sokol, Liver disease in mitochondrial disorders. *Seminars in liver*
1357 *disease* **27**, 259-273 (2007); published online EpubAug (10.1055/s-2007-
1358 985071).
1359 11. A. A. Morris, J. W. Taanman, J. Blake, J. M. Cooper, B. D. Lake, M. Malone, S.
1360 Love, P. T. Clayton, J. V. Leonard, A. H. Schapira, Liver failure associated with
1361 mitochondrial DNA depletion. *Journal of hepatology* **28**, 556-563 (1998);
1362 published online EpubApr (10.1016/s0168-8278(98)80278-x).
1363 12. H. Koh, G. S. Park, S. M. Shin, C. E. Park, S. Kim, S. J. Han, H. Q. Pham, J. H.
1364 Shin, D. W. Lee, Mitochondrial Mutations in Cholestatic Liver Disease with Biliary
1365 Atresia. *Scientific reports* **8**, 905 (2018); published online EpubJan 17
1366 (10.1038/s41598-017-18958-8).
1367 13. J. P. Molleston, R. J. Sokol, W. Karnsakul, A. Miethke, S. Horslen, J. C. Magee,
1368 R. Romero, R. H. Squires, J. L. Van Hove, N. Childhood Liver Disease Research
1369 Education, Evaluation of the child with suspected mitochondrial liver disease.
1370 *Journal of pediatric gastroenterology and nutrition* **57**, 269-276 (2013); published
1371 online EpubSep (10.1097/MPG.0b013e31829ef67a).
1372 14. K. Cloots, J. Verbeek, H. Orlent, W. Meersseman, D. Cassiman, Mitochondrial
1373 hepatopathy in adults: a case series and review of the literature. *European*
1374 *journal of gastroenterology & hepatology* **25**, 892-898 (2013); published online
1375 EpubAug (10.1097/MEG.0b013e32835ee629).
1376 15. P. F. Chinnery, S. DiMauro, Mitochondrial hepatopathies. *Journal of hepatology*
1377 **43**, 207-209 (2005); published online EpubAug (10.1016/j.jhep.2005.05.012).
1378 16. L. De Meirleir, S. Seneca, E. Damis, B. Sepulchre, A. Hoorens, E. Gerlo, M. T.
1379 Garcia Silva, E. M. Hernandez, W. Lissens, R. Van Coster, Clinical and

1380 diagnostic characteristics of complex III deficiency due to mutations in the BCS1L
1381 gene. *American journal of medical genetics. Part A* **121A**, 126-131 (2003);
1382 published online EpubAug 30 (10.1002/ajmg.a.20171).
1383 17. P. de Lonlay, I. Valnot, A. Barrientos, M. Gorbatyuk, A. Tzagoloff, J. W.
1384 Taanman, E. Benayoun, D. Chretien, N. Kadhom, A. Lombes, H. O. de Baulny,
1385 P. Niaudet, A. Munnich, P. Rustin, A. Rotig, A mutant mitochondrial respiratory
1386 chain assembly protein causes complex III deficiency in patients with
1387 tubulopathy, encephalopathy and liver failure. *Nature genetics* **29**, 57-60 (2001);
1388 published online EpubSep (10.1038/ng706).
1389 18. L. B. Sullivan, D. Y. Gui, A. M. Hosios, L. N. Bush, E. Freinkman, M. G. Vander
1390 Heiden, Supporting Aspartate Biosynthesis Is an Essential Function of
1391 Respiration in Proliferating Cells. *Cell* **162**, 552-563 (2015); published online
1392 EpubJul 30 (10.1016/j.cell.2015.07.017).
1393 19. L. K. Sharma, J. Lu, Y. Bai, Mitochondrial respiratory complex I: structure,
1394 function and implication in human diseases. *Current medicinal chemistry* **16**,
1395 1266-1277 (2009)10.2174/092986709787846578).
1396 20. S. E. Kruse, W. C. Watt, D. J. Marcinek, R. P. Kapur, K. A. Schenkman, R. D.
1397 Palmiter, Mice with mitochondrial complex I deficiency develop a fatal
1398 encephalomyopathy. *Cell metabolism* **7**, 312-320 (2008); published online
1399 EpubApr (10.1016/j.cmet.2008.02.004).
1400 21. S. Peralta, A. Torraco, T. Wenz, S. Garcia, F. Diaz, C. T. Moraes, Partial
1401 complex I deficiency due to the CNS conditional ablation of Ndufa5 results in a
1402 mild chronic encephalopathy but no increase in oxidative damage. *Human*
1403 *molecular genetics* **23**, 1399-1412 (2014); published online EpubMar 15
1404 (10.1093/hmg/ddt526).
1405 22. B. X. Ke, S. Pepe, D. R. Grubb, J. C. Komen, A. Laskowski, F. A. Rodda, B. M.
1406 Hardman, J. J. Pitt, M. T. Ryan, M. Lazarou, J. Koleff, M. M. Cheung, J. J.
1407 Smolich, D. R. Thorburn, Tissue-specific splicing of an Ndufs6 gene-trap
1408 insertion generates a mitochondrial complex I deficiency-specific
1409 cardiomyopathy. *Proceedings of the National Academy of Sciences of the United*

1410 *States of America* **109**, 6165-6170 (2012); published online EpubApr 17
1411 (10.1073/pnas.1113987109).
1412 23. L. Yang, J. C. Garcia Canaveras, Z. Chen, L. Wang, L. Liang, C. Jang, J. A.
1413 Mayr, Z. Zhang, J. M. Ghergurovich, L. Zhan, S. Joshi, Z. Hu, M. R. McReynolds,
1414 X. Su, E. White, R. J. Morscher, J. D. Rabinowitz, Serine Catabolism Feeds
1415 NADH when Respiration Is Impaired. *Cell metabolism* **31**, 809-821 e806 (2020);
1416 published online EpubApr 7 (10.1016/j.cmet.2020.02.017).
1417 24. C. V. Pereira, S. Peralta, T. Arguello, S. R. Bacman, F. Diaz, C. T. Moraes,
1418 Myopathy reversion in mice after restauration of mitochondrial complex I. *EMBO*
1419 *molecular medicine* **12**, e10674 (2020); published online EpubFeb 7
1420 (10.15252/emmm.201910674).
1421 25. N. Li, K. Ragheb, G. Lawler, J. Sturgis, B. Rajwa, J. A. Melendez, J. P. Robinson,
1422 Mitochondrial complex I inhibitor rotenone induces apoptosis through enhancing
1423 mitochondrial reactive oxygen species production. *The Journal of biological*
1424 *chemistry* **278**, 8516-8525 (2003); published online EpubMar 7
1425 (10.1074/jbc.M210432200).
1426 26. R. Fato, C. Bergamini, M. Bortolus, A. L. Maniero, S. Leoni, T. Ohnishi, G. Lenaz,
1427 Differential effects of mitochondrial Complex I inhibitors on production of reactive
1428 oxygen species. *Biochimica et biophysica acta* **1787**, 384-392 (2009); published
1429 online EpubMay (10.1016/j.bbabio.2008.11.003).
1430 27. R. P. Goodman, A. L. Markhard, H. Shah, R. Sharma, O. S. Skinner, C. B. Clish,
1431 A. Deik, A. Patgiri, Y. H. Hsu, R. Masia, H. L. Noh, S. Suk, O. Goldberger, J. N.
1432 Hirschhorn, G. Yellen, J. K. Kim, V. K. Mootha, Hepatic NADH reductive stress
1433 underlies common variation in metabolic traits. *Nature* **583**, 122-126 (2020);
1434 published online EpubJul (10.1038/s41586-020-2337-2).
1435 28. N. P. Lesner, A. S. Gokhale, K. Kota, R. J. DeBerardinis, P. Mishra, alpha-
1436 ketobutyrate links alterations in cystine metabolism to glucose oxidation in
1437 mtDNA mutant cells. *Metabolic engineering* **60**, 157-167 (2020); published online
1438 EpubJul (10.1016/j.ymben.2020.03.010).
1439 29. D. A. Cappel, S. Deja, J. A. G. Duarte, B. Kucejova, M. Inigo, J. A. Fletcher, X.
1440 Fu, E. D. Berglund, T. Liu, J. K. Elmquist, S. Hammer, P. Mishra, J. D. Browning,

1441 S. C. Burgess, Pyruvate-Carboxylase-Mediated Anaplerosis Promotes
1442 Antioxidant Capacity by Sustaining TCA Cycle and Redox Metabolism in Liver.
1443 *Cell metabolism* **29**, 1291-1305 e1298 (2019); published online EpubJun 4
1444 (10.1016/j.cmet.2019.03.014).
1445 30. M. E. Merritt, C. Harrison, A. D. Sherry, C. R. Malloy, S. C. Burgess, Flux through
1446 hepatic pyruvate carboxylase and phosphoenolpyruvate carboxykinase detected
1447 by hyperpolarized 13C magnetic resonance. *Proceedings of the National*
1448 *Academy of Sciences of the United States of America* **108**, 19084-19089 (2011);
1449 published online EpubNov 22 (10.1073/pnas.1111247108).
1450 31. S. G. Kim, N. V. Tsekos, Perfusion imaging by a flow-sensitive alternating
1451 inversion recovery (FAIR) technique: application to functional brain imaging.
1452 *Magnetic resonance in medicine* **37**, 425-435 (1997); published online EpubMar
1453 (10.1002/mrm.1910370321).
1454 32. H. Barash, E. Gross, I. Matot, Y. Edrei, G. Tsarfaty, G. Spira, I. Vlodavsky, E.
1455 Galun, R. Abramovitch, Functional MR imaging during hypercapnia and
1456 hyperoxia: noninvasive tool for monitoring changes in liver perfusion and
1457 hemodynamics in a rat model. *Radiology* **243**, 727-735 (2007); published online
1458 EpubJun (10.1148/radiol.2433060433).
1459 33. K. Wengler, J. Wang, M. Serrano Sosa, S. Gumus, A. He, S. Hussain, C. Huang,
1460 K. Tae Bae, X. He, Mapping hepatic blood oxygenation by quantitative BOLD
1461 (qBOLD) MRI. *Magnetic resonance in medicine* **81**, 3272-3282 (2019); published
1462 online EpubMay (10.1002/mrm.27642).
1463 34. R. R. Hallac, H. Zhou, R. Pidikiti, K. Song, S. Stojadinovic, D. Zhao, T. Solberg,
1464 P. Peschke, R. P. Mason, Correlations of noninvasive BOLD and TOLD MRI with
1465 pO2 and relevance to tumor radiation response. *Magnetic resonance in medicine*
1466 **71**, 1863-1873 (2014); published online EpubMay (10.1002/mrm.24846).
1467 35. E. Tadamura, H. Hatabu, W. Li, P. V. Prasad, R. R. Edelman, Effect of oxygen
1468 inhalation on relaxation times in various tissues. *Journal of magnetic resonance*
1469 *imaging : JMRI* **7**, 220-225 (1997); published online EpubJan-Feb
1470 (10.1002/jmri.1880070134).

1471 36. F. Diaz, C. K. Thomas, S. Garcia, D. Hernandez, C. T. Moraes, Mice lacking
1472 COX10 in skeletal muscle recapitulate the phenotype of progressive
1473 mitochondrial myopathies associated with cytochrome c oxidase deficiency.
1474 *Human molecular genetics* **14**, 2737-2748 (2005); published online EpubSep 15
1475 (10.1093/hmg/ddi307).
1476 37. F. Diaz, S. Garcia, D. Hernandez, A. Regev, A. Rebelo, J. Oca-Cossio, C. T.
1477 Moraes, Pathophysiology and fate of hepatocytes in a mouse model of
1478 mitochondrial hepatopathies. *Gut* **57**, 232-242 (2008); published online EpubFeb
1479 (10.1136/gut.2006.119180).
1480 38. S. Ghavami, M. Eshragi, S. R. Ande, W. J. Chazin, T. Klonisch, A. J. Halayko, K.
1481 D. McNeill, M. Hashemi, C. Kerkhoff, M. Los, S100A8/A9 induces autophagy and
1482 apoptosis via ROS-mediated cross-talk between mitochondria and lysosomes
1483 that involves BNIP3. *Cell research* **20**, 314-331 (2010); published online
1484 EpubMar (10.1038/cr.2009.129).
1485 39. S. Ghavami, C. Kerkhoff, W. J. Chazin, K. Kadkhoda, W. Xiao, A. Zuse, M.
1486 Hashemi, M. Eshraghi, K. Schulze-Osthoff, T. Klonisch, M. Los, S100A8/9
1487 induces cell death via a novel, RAGE-independent pathway that involves
1488 selective release of Smac/DIABLO and Omi/HtrA2. *Biochimica et biophysica acta*
1489 **1783**, 297-311 (2008); published online EpubFeb
1490 (10.1016/j.bbamcr.2007.10.015).
1491 40. N. Mazurek, J. C. Byrd, Y. Sun, M. Hafley, K. Ramirez, J. Burks, R. S. Bresalier,
1492 Cell-surface galectin-3 confers resistance to TRAIL by impeding trafficking of
1493 death receptors in metastatic colon adenocarcinoma cells. *Cell death and*
1494 *differentiation* **19**, 523-533 (2012); published online EpubMar
1495 (10.1038/cdd.2011.123).
1496 41. J. Kobayashi, H. Fujimoto, J. Sato, I. Hayashi, S. Burma, S. Matsuura, D. J.
1497 Chen, K. Komatsu, Nucleolin participates in DNA double-strand break-induced
1498 damage response through MDC1-dependent pathway. *PloS one* **7**, e49245
1499 (2012)10.1371/journal.pone.0049245).
1500 42. M. Goldstein, F. A. Derheimer, J. Tait-Mulder, M. B. Kastan, Nucleolin mediates
1501 nucleosome disruption critical for DNA double-strand break repair. *Proceedings*

1502 *of the National Academy of Sciences of the United States of America* **110**,
1503 16874-16879 (2013); published online EpubOct 15 (10.1073/pnas.1306160110).
1504 43. C. Yang, D. A. Maiguel, F. Carrier, Identification of nucleolin and nucleophosmin
1505 as genotoxic stress-responsive RNA-binding proteins. *Nucleic acids research* **30**,
1506 2251-2260 (2002); published online EpubMay 15 (10.1093/nar/30.10.2251).
1507 44. M. K. Singh, B. Sharma, P. K. Tiwari, The small heat shock protein Hsp27:
1508 Present understanding and future prospects. *Journal of thermal biology* **69**, 149-
1509 154 (2017); published online EpubOct (10.1016/j.jtherbio.2017.06.004).
1510 45. R. J. Hunt, L. Granat, G. S. McElroy, R. Ranganathan, N. S. Chandel, J. M.
1511 Bateman, Mitochondrial stress causes neuronal dysfunction via an ATF4-
1512 dependent increase in L-2-hydroxyglutarate. *The Journal of cell biology* **218**,
1513 4007-4016 (2019); published online EpubDec 2 (10.1083/jcb.201904148).
1514 46. M. G. Traber, J. F. Stevens, Vitamins C and E: beneficial effects from a
1515 mechanistic perspective. *Free radical biology & medicine* **51**, 1000-1013 (2011);
1516 published online EpubSep 1 (10.1016/j.freeradbiomed.2011.05.017).
1517 47. S. Kojima, S. Ona, I. Iizuka, T. Arai, H. Mori, K. Kubota, Antioxidative activity of
1518 5,6,7,8-tetrahydrobiopterin and its inhibitory effect on paraquat-induced cell
1519 toxicity in cultured rat hepatocytes. *Free radical research* **23**, 419-430 (1995);
1520 published online EpubNov (10.3109/10715769509065263).
1521 48. F. E. Frerman, S. I. Goodman, Deficiency of electron transfer flavoprotein or
1522 electron transfer flavoprotein:ubiquinone oxidoreductase in glutaric acidemia type
1523 II fibroblasts. *Proceedings of the National Academy of Sciences of the United*
1524 *States of America* **82**, 4517-4520 (1985); published online EpubJul
1525 (10.1073/pnas.82.13.4517).
1526 49. S. C. Grunert, Clinical and genetical heterogeneity of late-onset multiple acyl-
1527 coenzyme A dehydrogenase deficiency. *Orphanet journal of rare diseases* **9**, 117
1528 (2014); published online EpubJul 22 (10.1186/s13023-014-0117-5).
1529 50. M. A. Siano, C. Mandato, L. Nazzaro, G. Iannicelli, G. P. Ciccarelli, F. Barretta,
1530 C. Mazzaccara, M. Ruoppolo, G. Frisso, C. Baldi, S. Tartaglione, F. Di Salle, D.
1531 Melis, P. Vajro, Hepatic Presentation of Late-Onset Multiple Acyl-CoA

1532 Dehydrogenase Deficiency (MADD): Case Report and Systematic Review.
1533 *Frontiers in pediatrics* **9**, 672004 (2021)10.3389/fped.2021.672004).
1534 51. J. Xu, D. Li, J. Lv, X. Xu, B. Wen, P. Lin, F. Liu, K. Ji, J. Shan, H. Li, W. Li, Y.
1535 Zhao, D. Zhao, J. Y. Pok, C. Yan, ETFDH Mutations and Flavin Adenine
1536 Dinucleotide Homeostasis Disturbance Are Essential for Developing Riboflavin-
1537 Responsive Multiple Acyl-Coenzyme A Dehydrogenation Deficiency. *Annals of*
1538 *neurology* **84**, 659-673 (2018); published online EpubNov (10.1002/ana.25338).
1539 52. L. Stiburek, K. Vesela, H. Hansikova, H. Hulkova, J. Zeman, Loss of function of
1540 Sco1 and its interaction with cytochrome c oxidase. *American journal of*
1541 *physiology. Cell physiology* **296**, C1218-1226 (2009); published online EpubMay
1542 (10.1152/ajpcell.00564.2008).
1543 53. E. Lapuente-Brun, R. Moreno-Loshuertos, R. Acin-Perez, A. Latorre-Pellicer, C.
1544 Colas, E. Balsa, E. Perales-Clemente, P. M. Quiros, E. Calvo, M. A. Rodriguez-
1545 Hernandez, P. Navas, R. Cruz, A. Carracedo, C. Lopez-Otin, A. Perez-Martos, P.
1546 Fernandez-Silva, E. Fernandez-Vizarra, J. A. Enriquez, Supercomplex assembly
1547 determines electron flux in the mitochondrial electron transport chain. *Science*
1548 **340**, 1567-1570 (2013); published online EpubJun 28
1549 (10.1126/science.1230381).
1550 54. P. Jha, X. Wang, J. Auwerx, Analysis of Mitochondrial Respiratory Chain
1551 Supercomplexes Using Blue Native Polyacrylamide Gel Electrophoresis (BN-
1552 PAGE). *Current protocols in mouse biology* **6**, 1-14 (2016); published online
1553 EpubMar 1 (10.1002/9780470942390.mo150182).
1554 55. X. Wang, S. D. Shelton, B. Bordieanu, A. R. Frank, Y. Yi, S. S. K. Venigalla, Z.
1555 Gu, N. P. Lenser, M. Glogauer, N. S. Chandel, H. Zhao, Z. Zhao, D. G.
1556 McFadden, P. Mishra, Scinderin promotes fusion of electron transport chain
1557 dysfunctional muscle stem cells with myofibers. *Nature aging* **2**, 155-169
1558 (2022)10.1038/s43587-021-00164-x).
1559 56. G. W. Rogers, M. D. Brand, S. Petrosyan, D. Ashok, A. A. Elorza, D. A. Ferrick,
1560 A. N. Murphy, High throughput microplate respiratory measurements using
1561 minimal quantities of isolated mitochondria. *PloS one* **6**, e21746
1562 (2011)10.1371/journal.pone.0021746).

1563 57. J. M. Ubellacker, A. Tasdogan, V. Ramesh, B. Shen, E. C. Mitchell, M. S. Martin-
1564 Sandoval, Z. Gu, M. L. McCormick, A. B. Durham, D. R. Spitz, Z. Zhao, T. P.
1565 Mathews, S. J. Morrison, Lymph protects metastasizing melanoma cells from
1566 ferroptosis. *Nature* **585**, 113-118 (2020); published online EpubSep
1567 (10.1038/s41586-020-2623-z).
1568 58. A. Tasdogan, B. Faubert, V. Ramesh, J. M. Ubellacker, B. Shen, A. Solmonson,
1569 M. M. Murphy, Z. Gu, W. Gu, M. Martin, S. Y. Kasitinon, T. Vandergriff, T. P.
1570 Mathews, Z. Zhao, D. Schadendorf, R. J. DeBerardinis, S. J. Morrison, Metabolic
1571 heterogeneity confers differences in melanoma metastatic potential. *Nature* **577**,
1572 115-120 (2020); published online EpubJan (10.1038/s41586-019-1847-2).
1573 59. W. Lu, L. Wang, L. Chen, S. Hui, J. D. Rabinowitz, Extraction and Quantitation of
1574 Nicotinamide Adenine Dinucleotide Redox Cofactors. *Antioxidants & redox*
1575 *signaling* **28**, 167-179 (2018); published online EpubJan 20
1576 (10.1089/ars.2017.7014).
1577 60. J. T. Aguilan, K. Kulej, S. Sidoli, Guide for protein fold change and p-value
1578 calculation for non-experts in proteomics. *Molecular omics* **16**, 573-582 (2020);
1579 published online EpubDec 1 (10.1039/d0mo00087f).
1580 61. S. E. Calvo, K. R. Clauser, V. K. Mootha, MitoCarta2.0: an updated inventory of
1581 mammalian mitochondrial proteins. *Nucleic acids research* **44**, D1251-1257
1582 (2016); published online EpubJan 4 (10.1093/nar/gkv1003).
1583 62. A. Subramanian, P. Tamayo, V. K. Mootha, S. Mukherjee, B. L. Ebert, M. A.
1584 Gillette, A. Paulovich, S. L. Pomeroy, T. R. Golub, E. S. Lander, J. P. Mesirov,
1585 Gene set enrichment analysis: a knowledge-based approach for interpreting
1586 genome-wide expression profiles. *Proceedings of the National Academy of*
1587 *Sciences of the United States of America* **102**, 15545-15550 (2005); published
1588 online EpubOct 25 (10.1073/pnas.0506580102).
1589 63. V. K. Mootha, C. M. Lindgren, K. F. Eriksson, A. Subramanian, S. Sihag, J.
1590 Lehar, P. Puigserver, E. Carlsson, M. Ridderstrale, E. Laurila, N. Houstis, M. J.
1591 Daly, N. Patterson, J. P. Mesirov, T. R. Golub, P. Tamayo, B. Spiegelman, E. S.
1592 Lander, J. N. Hirschhorn, D. Altshuler, L. C. Groop, PGC-1alpha-responsive
1593 genes involved in oxidative phosphorylation are coordinately downregulated in

1594 human diabetes. *Nature genetics* **34**, 267-273 (2003); published online EpubJul
1595 (10.1038/ng1180).
1596 64. B. Faubert, A. Tasdogan, S. J. Morrison, T. P. Mathews, R. J. DeBerardinis,
1597 Stable isotope tracing to assess tumor metabolism in vivo. *Nature protocols* **16**,
1598 5123-5145 (2021); published online EpubNov (10.1038/s41596-021-00605-2).
1599 65. S. M. Davidson, T. Papagiannakopoulos, B. A. Olenchock, J. E. Heyman, M. A.
1600 Keibler, A. Luengo, M. R. Bauer, A. K. Jha, J. P. O'Brien, K. A. Pierce, D. Y. Gui,
1601 L. B. Sullivan, T. M. Wasylenko, L. Subbaraj, C. R. Chin, G. Stephanopolous, B.
1602 T. Mott, T. Jacks, C. B. Clish, M. G. Vander Heiden, Environment Impacts the
1603 Metabolic Dependencies of Ras-Driven Non-Small Cell Lung Cancer. *Cell*
1604 *metabolism* **23**, 517-528 (2016); published online EpubMar 8
1605 (10.1016/j.cmet.2016.01.007).
1606 66. C. A. Fernandez, C. Des Rosiers, S. F. Previs, F. David, H. Brunengraber,
1607 Correction of 13C mass isotopomer distributions for natural stable isotope
1608 abundance. *Journal of mass spectrometry : JMS* **31**, 255-262 (1996); published
1609 online EpubMar (10.1002/(SICI)1096-9888(199603)31:3<255::AID-
1610 JMS290>3.0.CO;2-3).
1611 67. J. K. Kelleher, Estimating gluconeogenesis with [U-13C]glucose: molecular
1612 condensation requires a molecular approach. *The American journal of physiology*
1613 **277**, E395-400 (1999); published online EpubSep
1614 (10.1152/ajpendo.1999.277.3.E395).
1615 68. G. Helms, H. Dathe, P. Dechent, Quantitative FLASH MRI at 3T using a rational
1616 approximation of the Ernst equation. *Magnetic resonance in medicine* **59**, 667-
1617 672 (2008); published online EpubMar (10.1002/mrm.21542).

1618

Figure 1

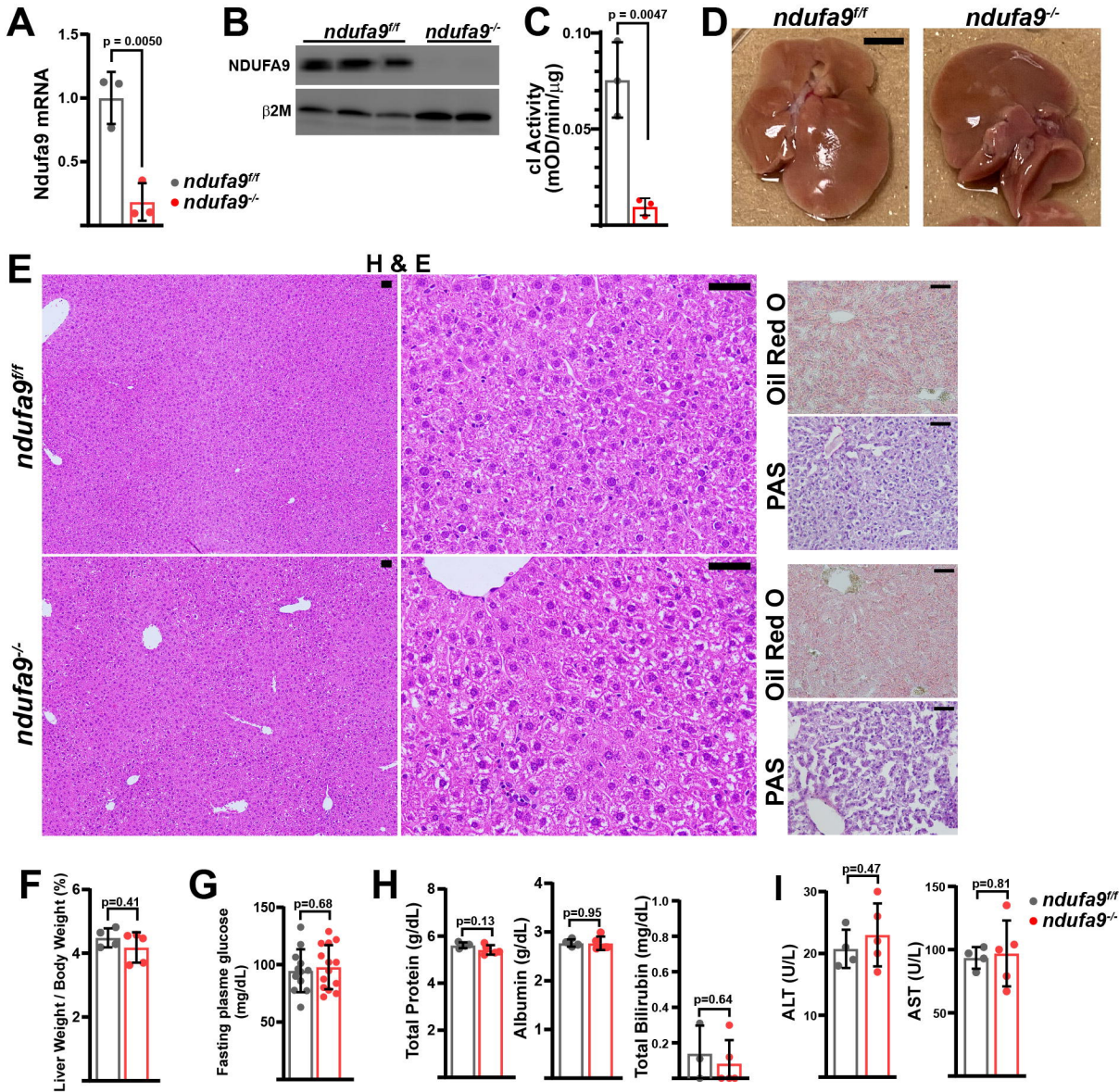
A
Ndufa9 mRNA
p = 0.0050
ndufa9f/f
ndufa9-/-
B
ndufa9f/f
ndufa9-/-
NDUFA9
β2M
C
cI Activity (mOD/min/μg)
p = 0.0047
D
ndufa9f/f
ndufa9-/-
E
H & E
ndufa9f/f
ndufa9-/-
Oil Red O
PAS
Oil Red O
PAS
F
Liver Weight / Body Weight (%)
p=0.41
G
Fasting plasme glucose (mg/dL)
p=0.68
H
Total Protein (g/dL)
p=0.13
Albumin (g/dL)
p=0.95
Total Bilirubin (mg/dL)
p=0.64
I
ALT (U/L)
p=0.47
AST (U/L)
p=0.81
ndufa9f/f
ndufa9-/-

Figure 2

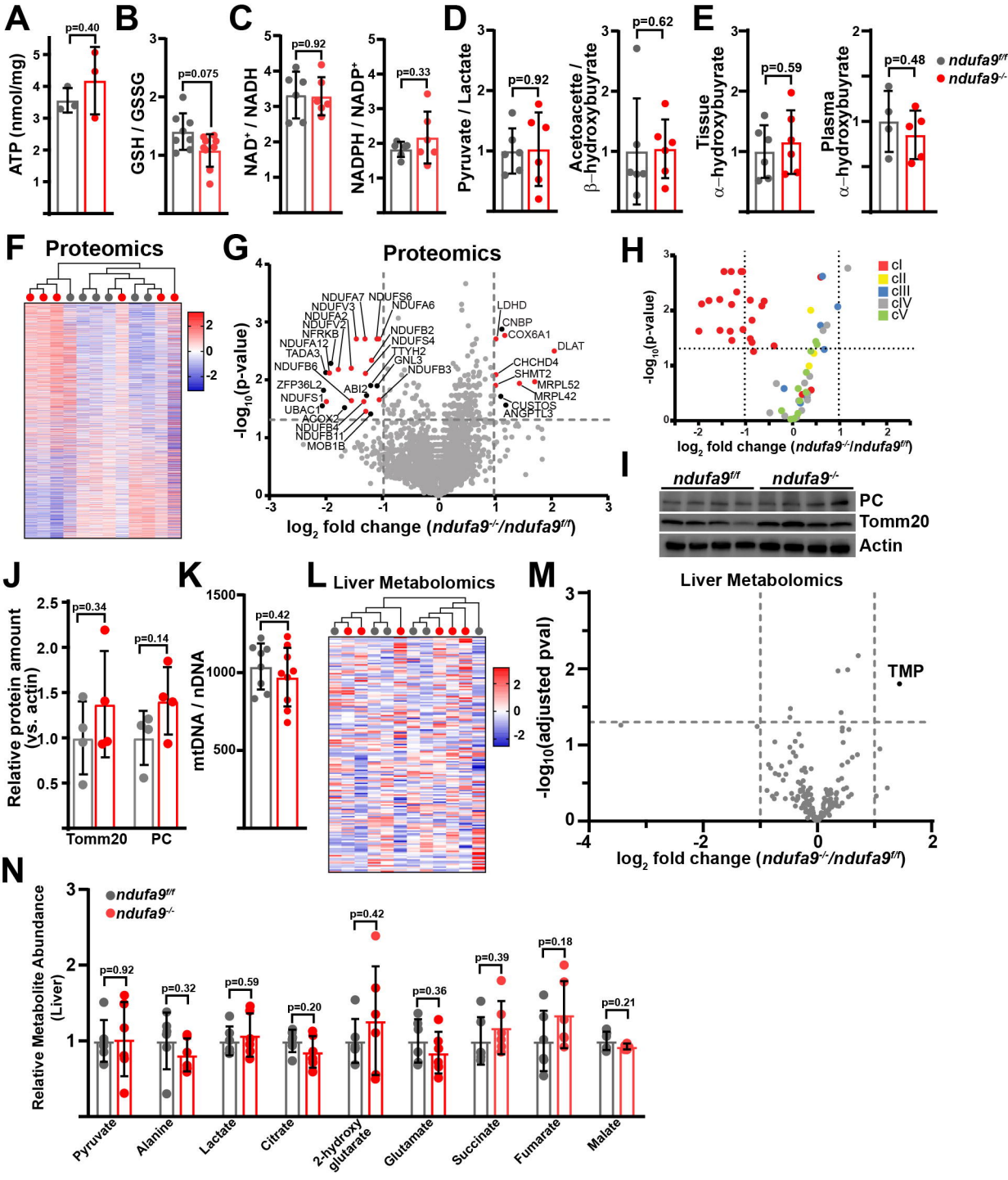
A
ATP (nmol/mg)
p=0.40
B
GSH / GSSG
p=0.075
C
NAD+ / NADH
p=0.92
NADPH / NADP+
p=0.33
D
Pyruvate / Lactate
p=0.92
Acetoacette / β–hydroxybuyrate
p=0.62
E
Tissue α–hydroxybuyrate
p=0.59
Plasma α–hydroxybuyrate
p=0.48
ndufa9f/f
ndufa9-/-
F
Proteomics
G
Proteomics
-log10(p-value)
log2 fold change (ndufa9-/-/ndufa9f/f)
NDUFA7
NDUFS6
NDUFV3
NDUFA6
NDUFA2
NDUFV2
NFRKB
NDUFB2
NDUFS4
NDUFA12
TTYH2
TADA3
GNL3
NDUFB6
NDUFB3
ZFP36L2
ABI2
NDUFS1
UBAC1
ACOX2
NDUFB4
NDUFB11
MOB1B
LDHD
CNBP
COX6A1
DLAT
CHCHD4
SHMT2
MRPL52
MRPL42
CUSTOS
ANGPTL3
H
cI
cII
cIII
cIV
cV
-log10(p-value)
log2 fold change (ndufa9-/-/ndufa9f/f)
I
ndufa9f/f
ndufa9-/-
PC
Tomm20
Actin
J
Relative protein amount (vs. actin)
p=0.34
p=0.14
Tomm20
PC
K
mtDNA / nDNA
p=0.42
L
Liver Metabolomics
M
Liver Metabolomics
-log10(adjusted pval)
TMP
log2 fold change (ndufa9-/-/ndufa9f/f)
N
Relative Metabolite Abundance (Liver)
ndufa9f/f
ndufa9-/-
p=0.92
p=0.32
p=0.59
p=0.20
p=0.42
p=0.36
p=0.39
p=0.18
p=0.21
Pyruvate
Alanine
Lactate
Citrate
2-hydroxy glutarate
Glutamate
Succinate
Fumarate
Malate

Figure 3

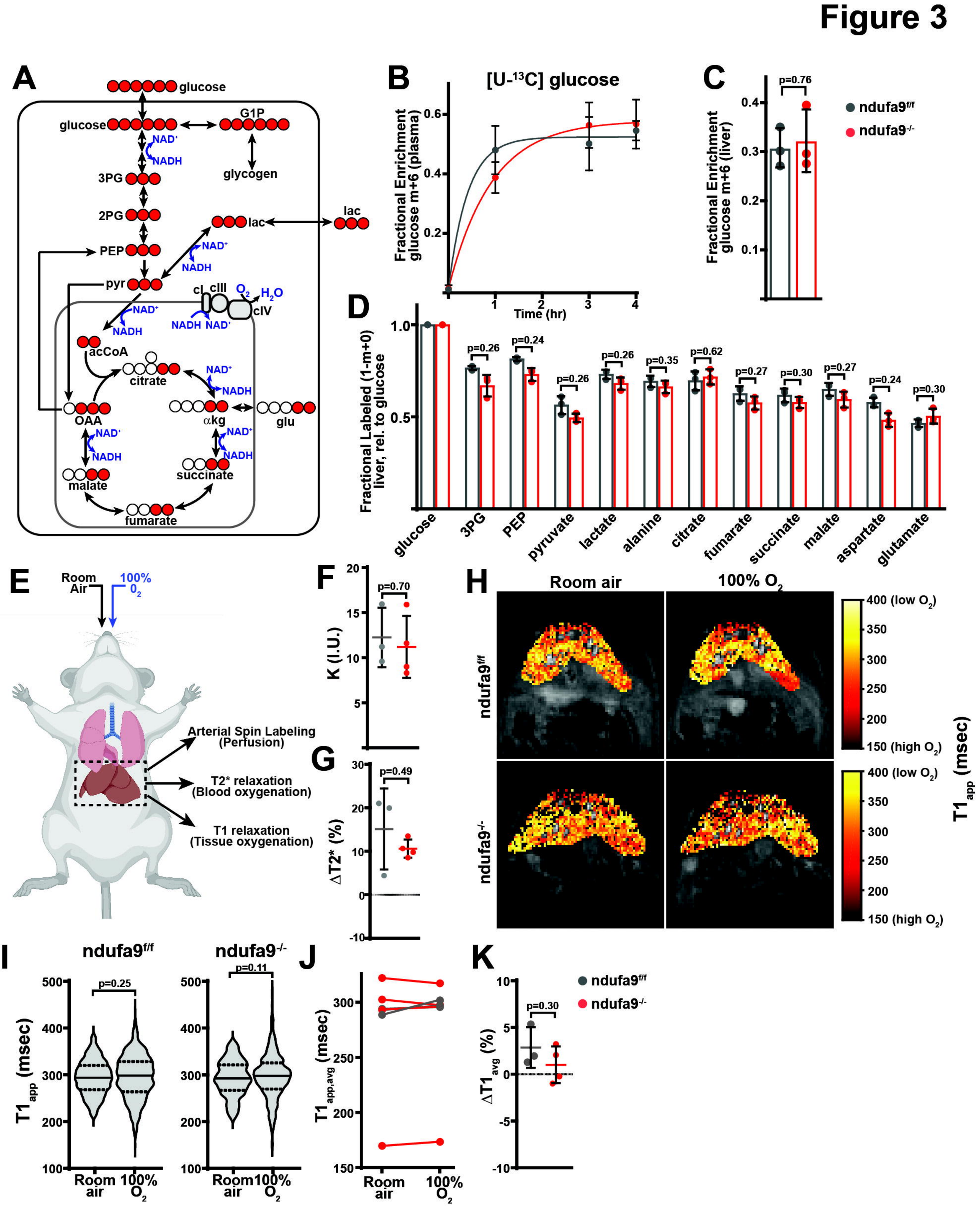
A
glucose
G1P
glucose
NAD+
NADH
glycogen
3PG
2PG
lac
lac
PEP
NAD+
NADH
pyr
cI
cIII
O2
H2O
cIV
NAD+
NADH
NADH
NAD+
acCoA
citrate
NAD+
NADH
OAA
αkg
glu
NAD+
NADH
NAD+
NADH
malate
succinate
fumarate
B
[U-13C] glucose
Fractional Enrichment glucose m+6 (plasma)
Time (hr)
C
p=0.76
Fractional Enrichment glucose m+6 (liver)
ndufa9f/f
ndufa9-/-
D
Fractional Labeled (1-m+0) liver, rel. to glucose
p=0.26
p=0.24
p=0.26
p=0.26
p=0.35
p=0.62
p=0.27
p=0.30
p=0.27
p=0.24
p=0.30
glucose
3PG
PEP
pyruvate
lactate
alanine
citrate
fumarate
succinate
malate
aspartate
glutamate
E
Room Air
100% O2
Arterial Spin Labeling (Perfusion)
T2* relaxation (Blood oxygenation)
T1 relaxation (Tissue oxygenation)
F
p=0.70
K (I.U.)
G
p=0.49
ΔT2* (%)
H
Room air
100% O2
ndufa9f/f
ndufa9-/-
400 (low O2)
150 (high O2)
T1app (msec)
I
ndufa9f/f
ndufa9-/-
p=0.25
p=0.11
T1app (msec)
Room air
100% O2
J
T1app,avg (msec)
Room air
100% O2
K
p=0.30
ΔT1avg (%)
ndufa9f/f
ndufa9-/-

Figure 4

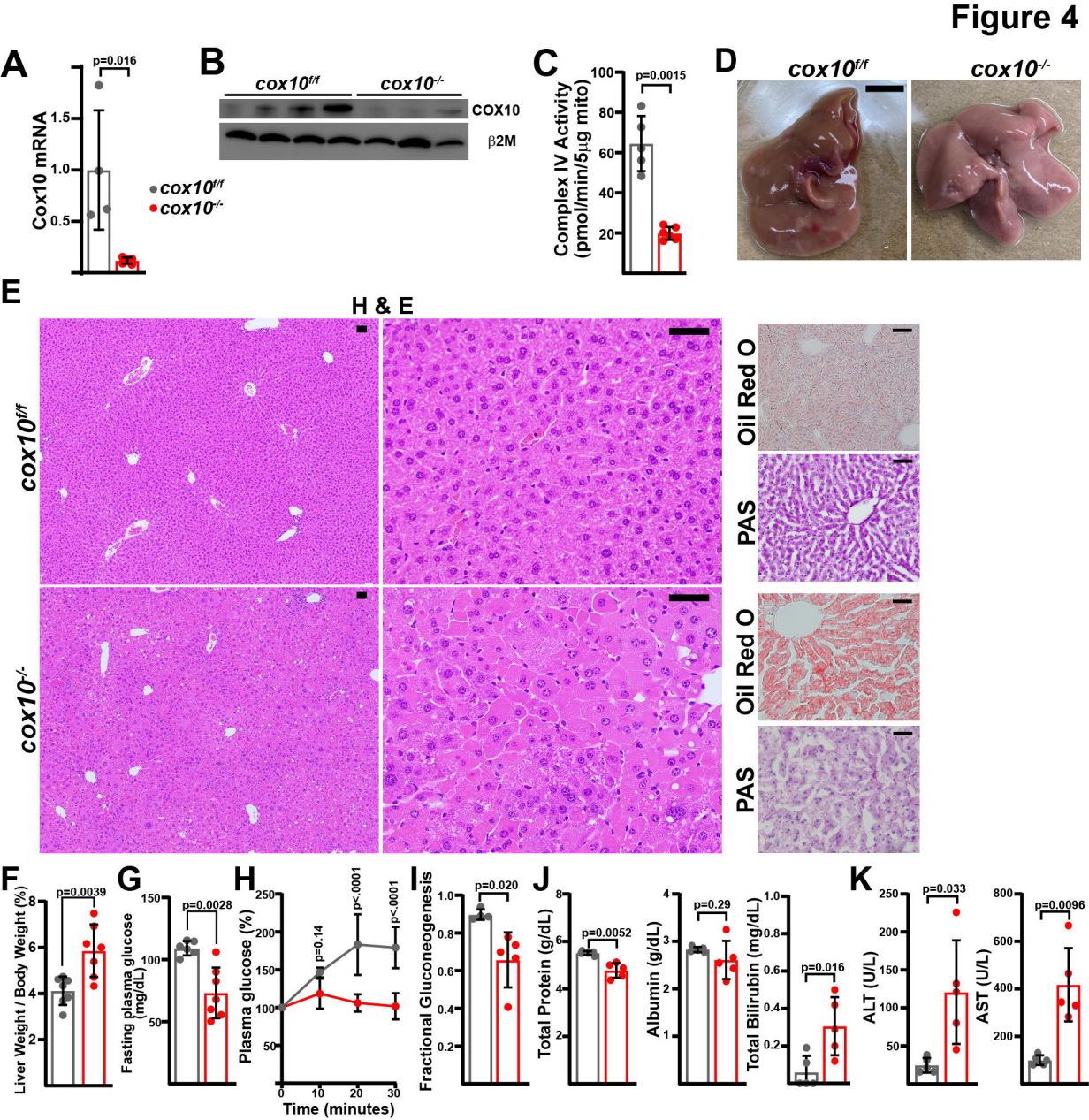
A
p=0.016
Cox10 mRNA
1.5
1.0
0.5
cox10f/f
cox10-/-
B
cox10f/f
cox10-/-
COX10
β2M
C
p=0.0015
Complex IV Activity (pmol/min/5μg mito)
100
80
60
40
20
D
cox10f/f
cox10-/-
E
H & E
cox10f/f
cox10-/-
Oil Red O
PAS
Oil Red O
PAS
F
p=0.0039
Liver Weight / Body Weight (%)
8
6
4
2
G
p=0.0028
Fasting plasma glucose (mg/dL)
150
100
50
H
p=0.14
p<.0001
p<.0001
Plasma glucose (%)
250
200
150
100
50
0
10
20
30
Time (minutes)
I
p=0.020
Fractional Gluconeogenesis
1.0
0.8
0.6
0.4
0.2
J
p=0.0052
Total Protein (g/dL)
8
6
4
2
p=0.29
Albumin (g/dL)
4
3
2
1
p=0.016
Total Bilirubin (mg/dL)
1.0
0.8
0.6
0.4
0.2
K
p=0.033
ALT (U/L)
250
200
150
100
50
p=0.0096
AST (U/L)
800
600
400
200

Figure 5

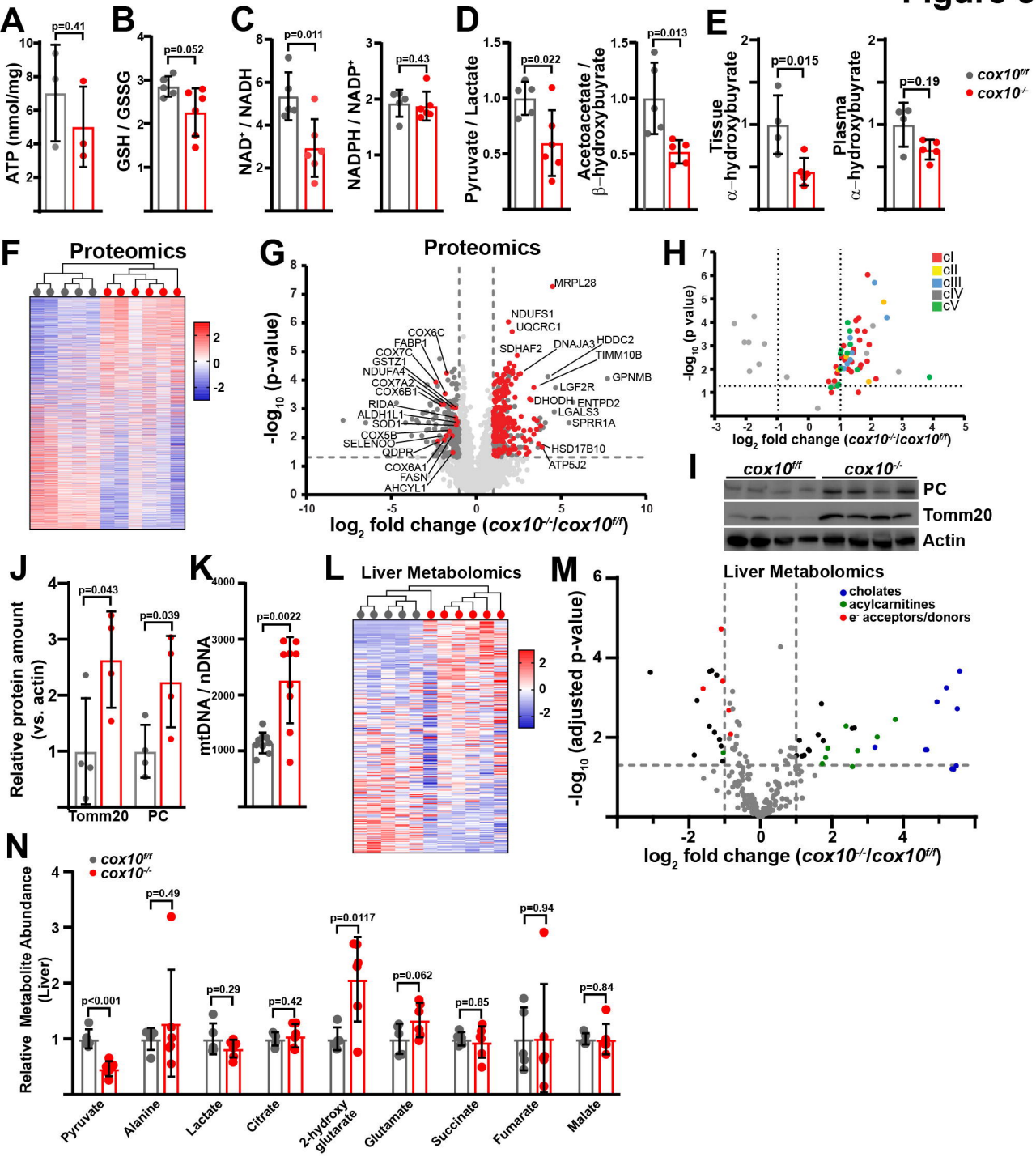
A
ATP (nmol/mg)
p=0.41
B
GSH / GSSG
p=0.052
C
NAD+ / NADH
p=0.011
NADPH / NADP+
p=0.43
D
Pyruvate / Lactate
p=0.022
Acetoacetate / β–hydroxybuyrate
p=0.013
E
Tissue α–hydroxybuyrate
p=0.015
Plasma α–hydroxybuyrate
p=0.19
cox10f/f
cox10-/-
F
Proteomics
G
Proteomics
-log10 (p-value)
log2 fold change (cox10-/-/cox10f/f)
MRPL28
NDUFS1
UQCRC1
SDHAF2
DNAJA3
HDDC2
TIMM10B
GPNMB
LGF2R
DHODH
ENTPD2
LGALS3
SPRR1A
HSD17B10
ATP5J2
COX6C
FABP1
COX7C
GSTZ1
NDUFA4
COX7A2
COX6B1
RIDA
ALDH1L1
SOD1
COX5B
SELENOO
QDPR
COX6A1
FASN
AHCYL1
H
-log10 (p value)
log2 fold change (cox10-/-/cox10f/f)
cI
cII
cIII
cIV
cV
I
cox10f/f
cox10-/-
PC
Tomm20
Actin
J
Relative protein amount (vs. actin)
p=0.043
p=0.039
Tomm20
PC
K
mtDNA / nDNA
p=0.0022
L
Liver Metabolomics
M
Liver Metabolomics
-log10 (adjusted p-value)
log2 fold change (cox10-/-/cox10f/f)
cholates
acylcarnitines
e- acceptors/donors
N
Relative Metabolite Abundance (Liver)
cox10f/f
cox10-/-
p<0.001
p=0.49
p=0.29
p=0.42
p=0.0117
p=0.062
p=0.85
p=0.94
p=0.84
Pyruvate
Alanine
Lactate
Citrate
2-hydroxy glutarate
Glutamate
Succinate
Fumarate
Malate

Figure 6

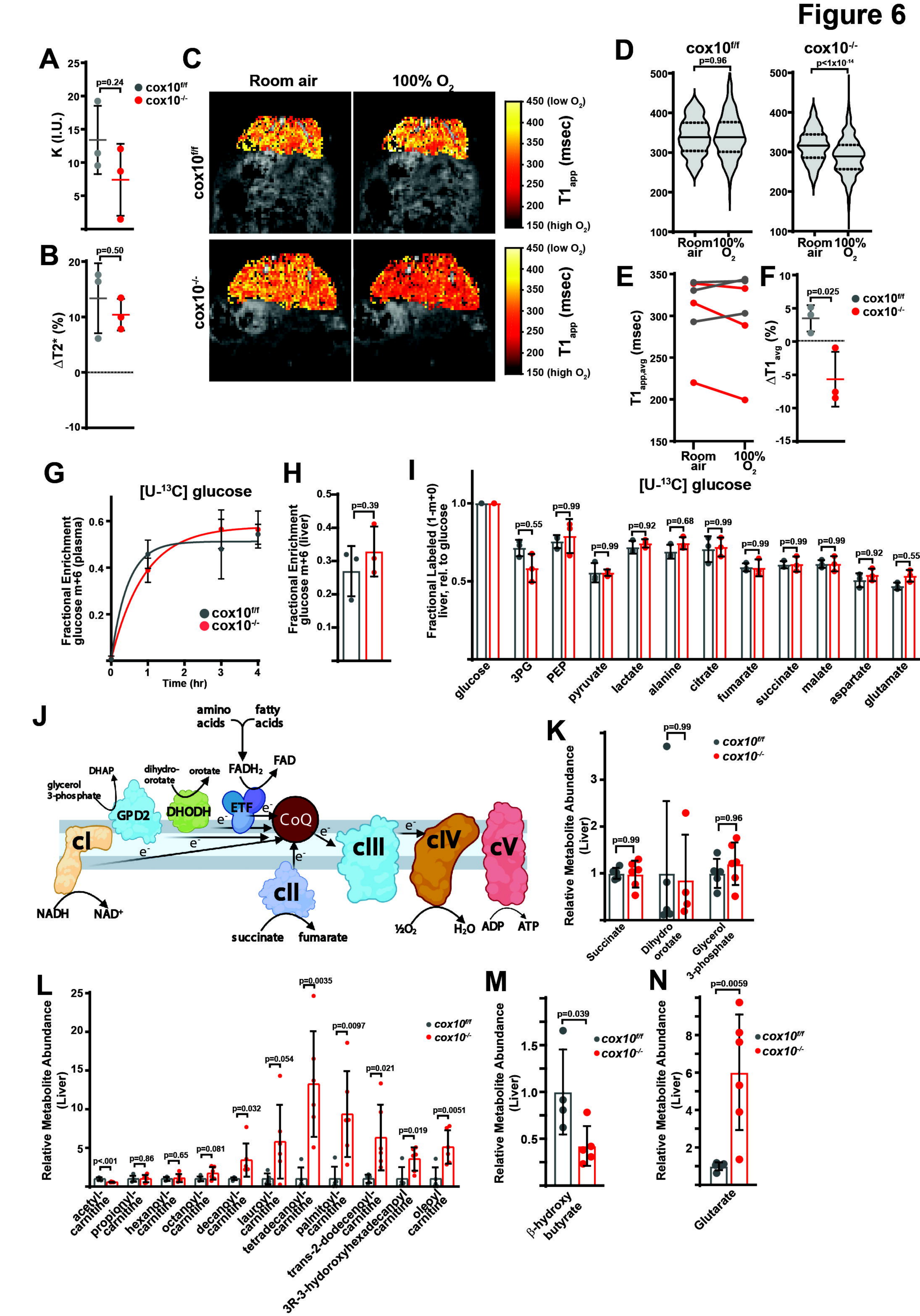
A
K (I.U.)
p=0.24
cox10f/f
cox10-/-
B
ΔT2* (%)
p=0.50
C
Room air
100% O2
cox10f/f
cox10-/-
T1app (msec)
450 (low O2)
150 (high O2)
D
cox10f/f
cox10-/-
p=0.96
p<1x10-14
Room air
100% O2
E
T1app,avg (msec)
F
ΔT1avg (%)
p=0.025
G
[U-13C] glucose
Fractional Enrichment glucose m+6 (plasma)
Time (hr)
H
Fractional Enrichment glucose m+6 (liver)
p=0.39
I
[U-13C] glucose
Fractional Labeled (1-m+0) liver, rel. to glucose
glucose
3PG
PEP
pyruvate
lactate
alanine
citrate
fumarate
succinate
malate
aspartate
glutamate
J
amino acids
fatty acids
FADH2
FAD
DHAP
glycerol 3-phosphate
dihydro-orotate
orotate
GPD2
DHODH
ETF
CoQ
cI
cII
cIII
cIV
cV
NADH
NAD+
succinate
fumarate
½O2
H2O
ADP
ATP
K
Relative Metabolite Abundance (Liver)
p=0.99
p=0.96
Succinate
Dihydro orotate
Glycerol 3-phosphate
L
Relative Metabolite Abundance (Liver)
p<.001
p=0.86
p=0.65
p=0.081
p=0.032
p=0.054
p=0.0035
p=0.0097
p=0.021
p=0.019
p=0.0051
acetyl-carnitine
propionyl-carnitine
hexanoyl-carnitine
octanoyl-carnitine
decanoyl-carnitine
lauroyl-carnitine
tetradecanoyl-carnitine
palmitoyl-carnitine
trans-2-dodecenoyl-carnitine
3R-3-hydoroxyhexadecanoyl carnitine
oleoyl carnitine
M
Relative Metabolite Abundance (Liver)
p=0.039
β-hydroxy butyrate
N
Relative Metabolite Abundance (Liver)
p=0.0059
Glutarate

Figure 1 - figure supplement 1

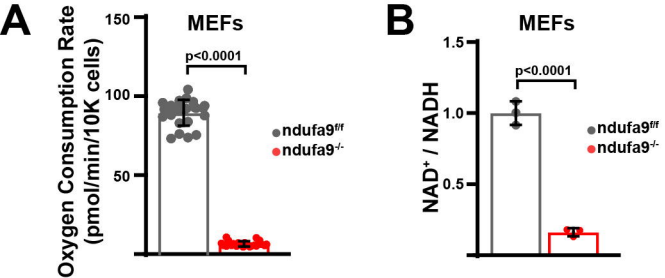

Figure 1 - figure supplement 2

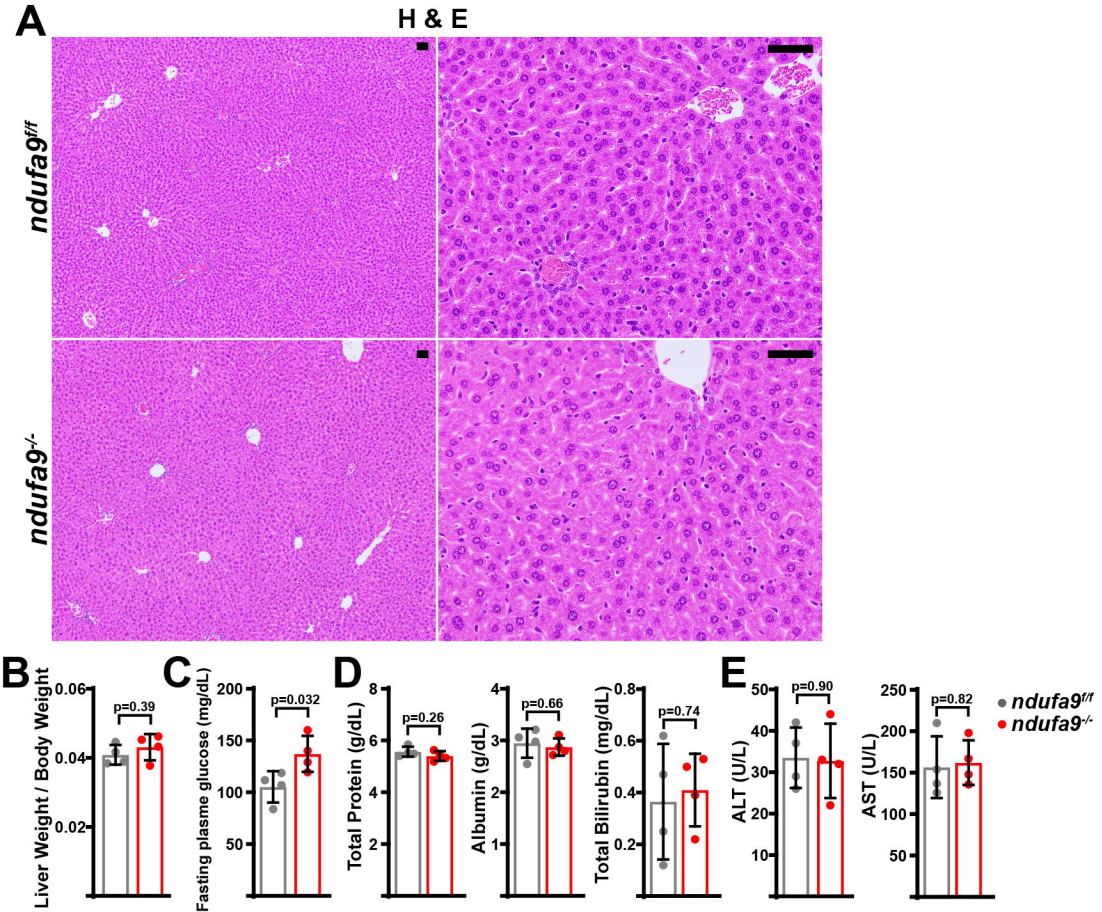

Figure 1 - figure supplement 3

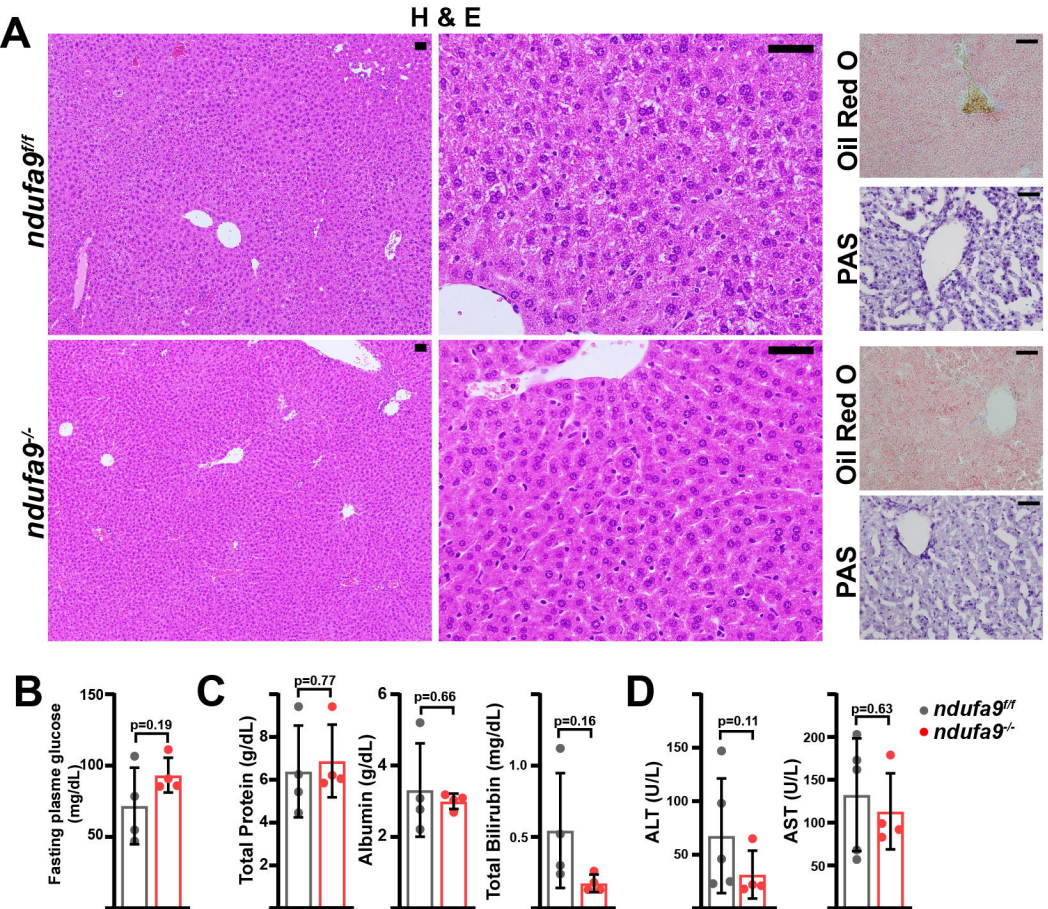

Figure 2 - figure supplement 1

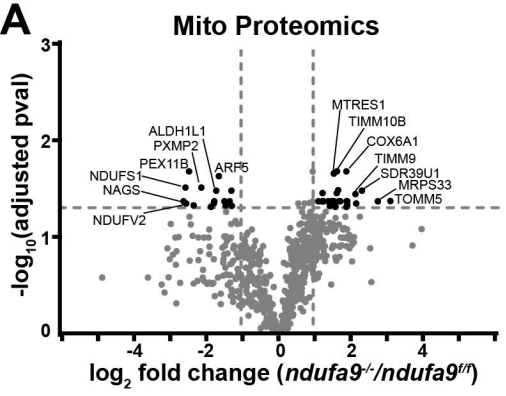

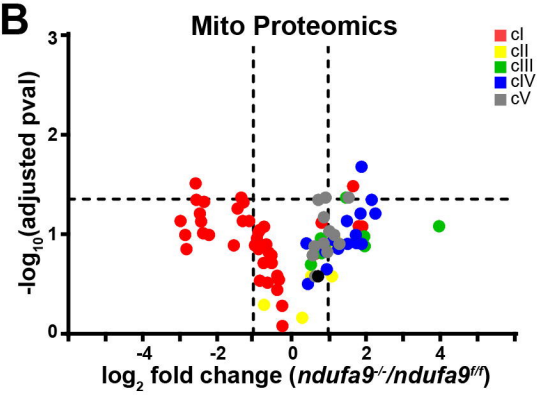

Figure 2 - figure supplement 2

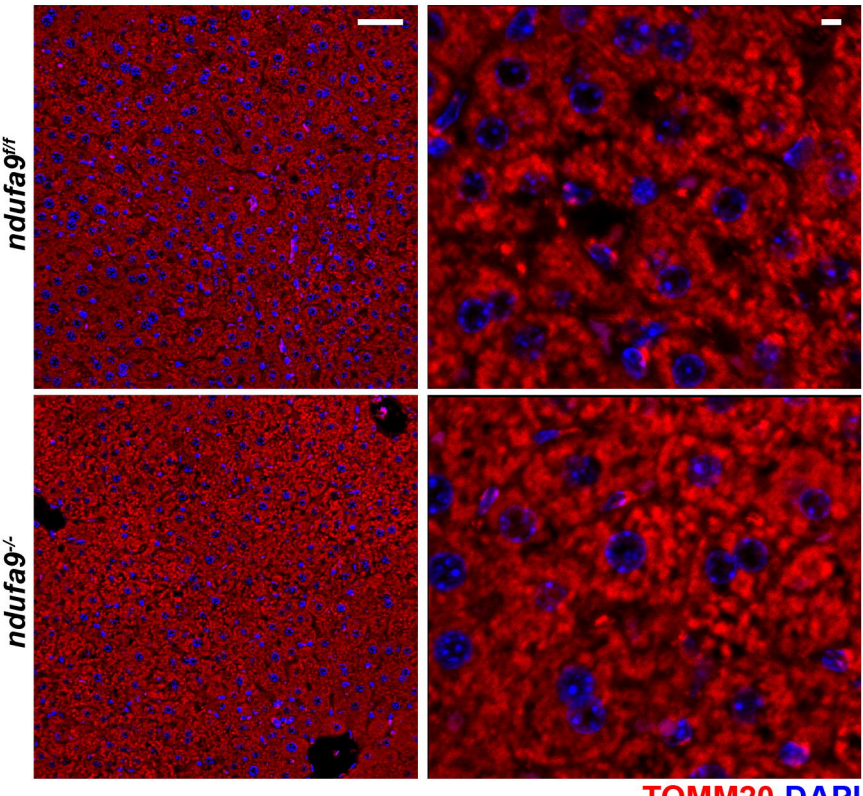

Figure 3 - figure supplement 1

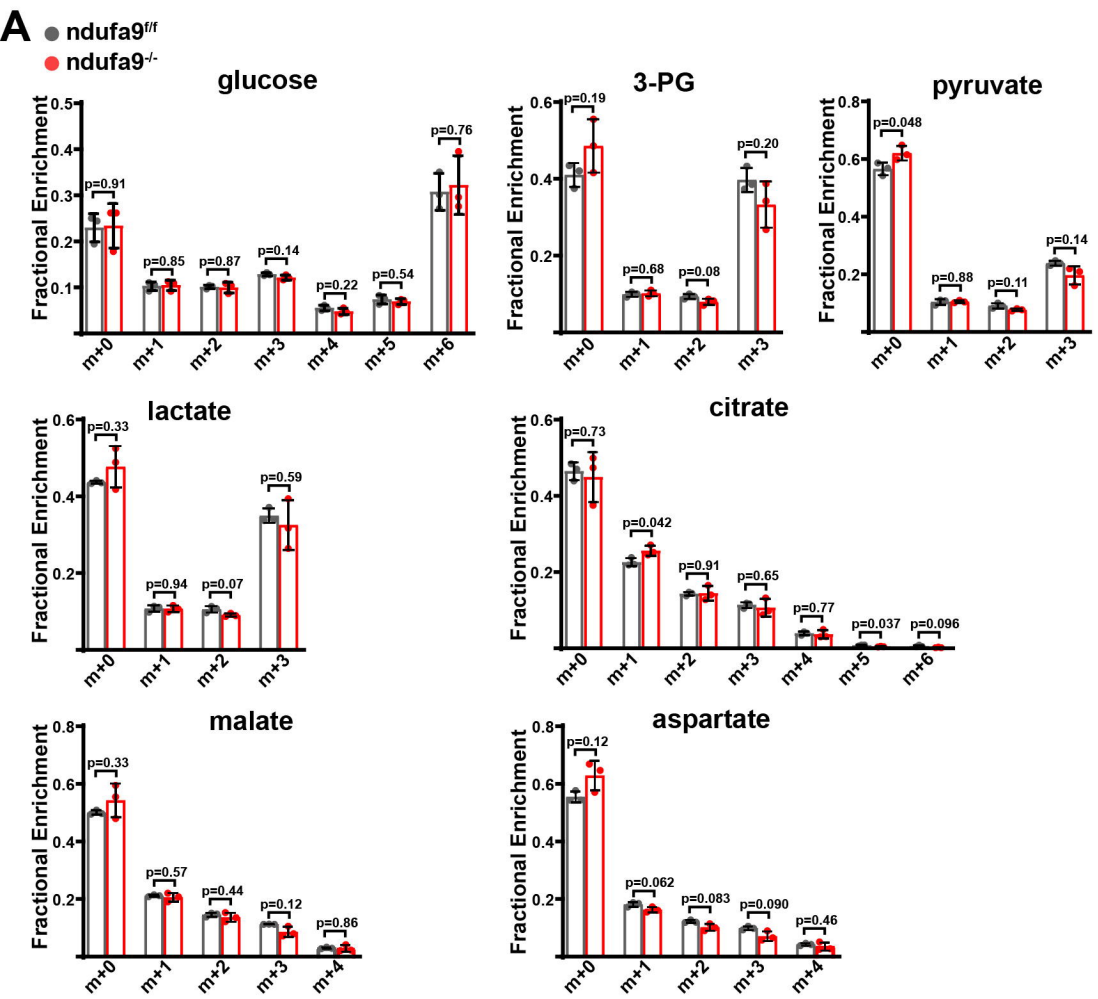

Figure 4 - figure supplement 1

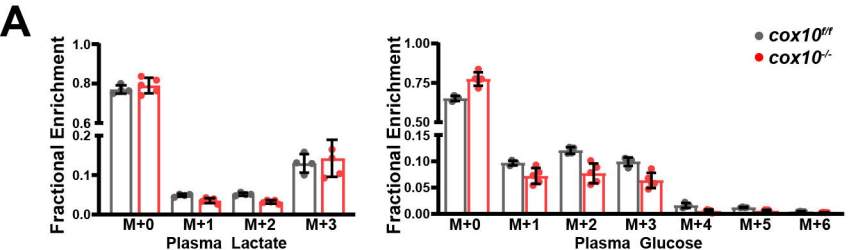

Figure 5 - figure supplement 1

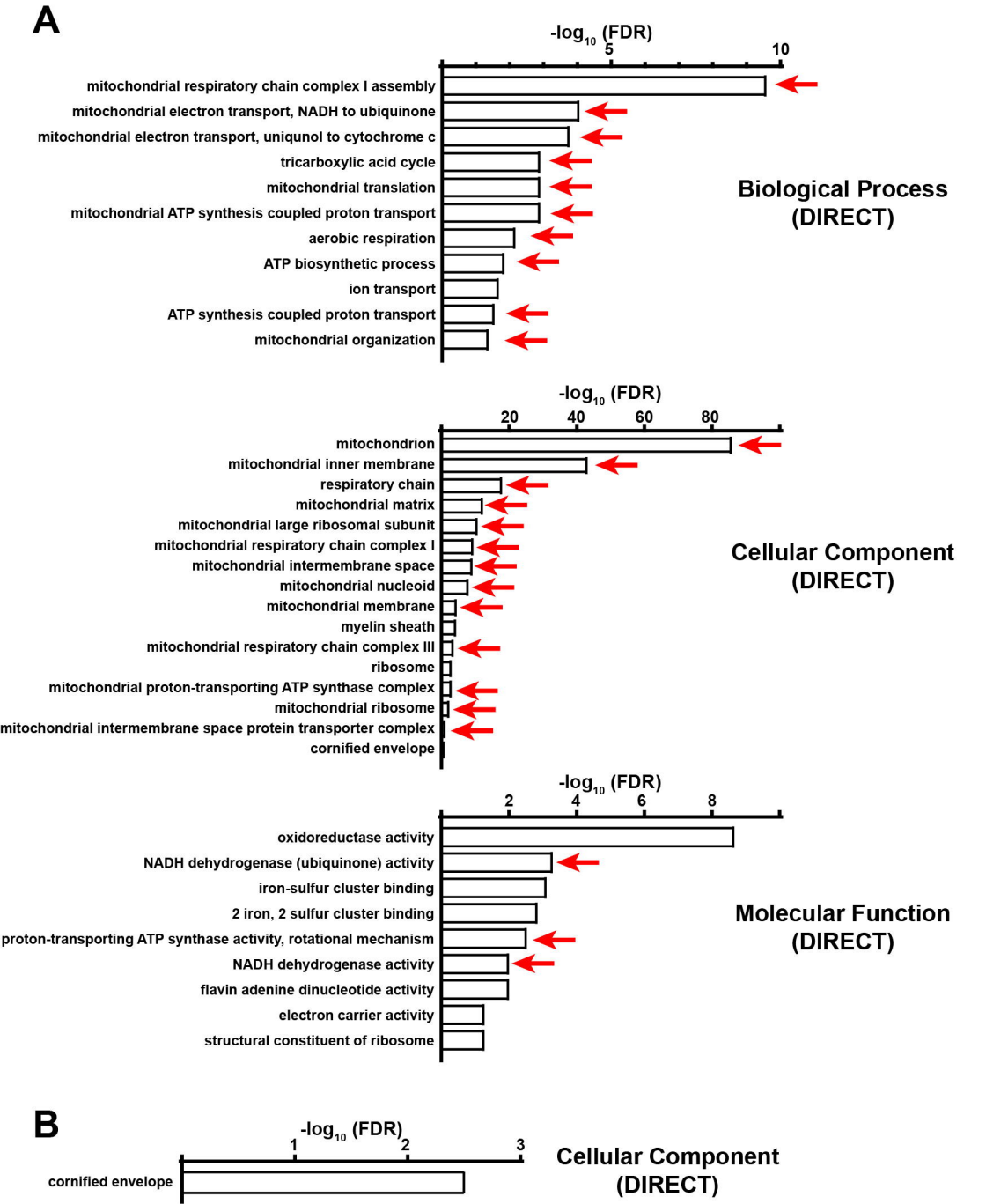

Figure 5 - figure supplement 2

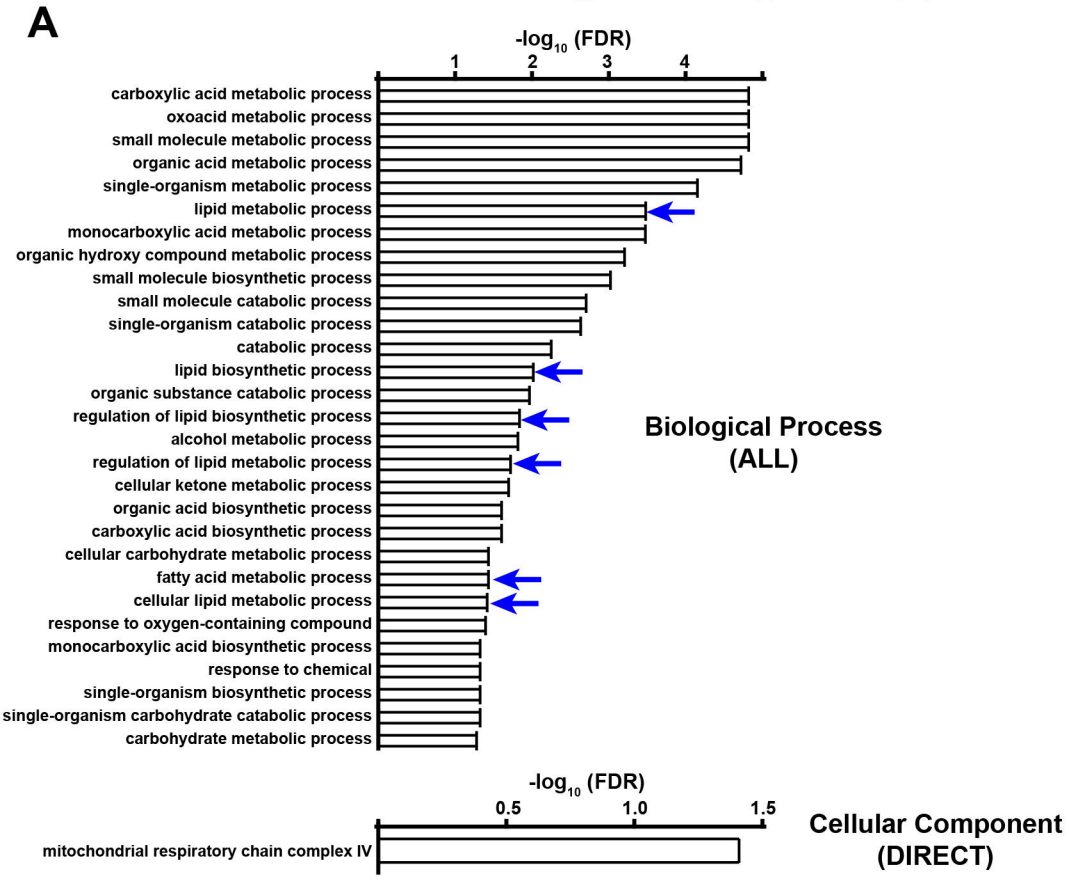

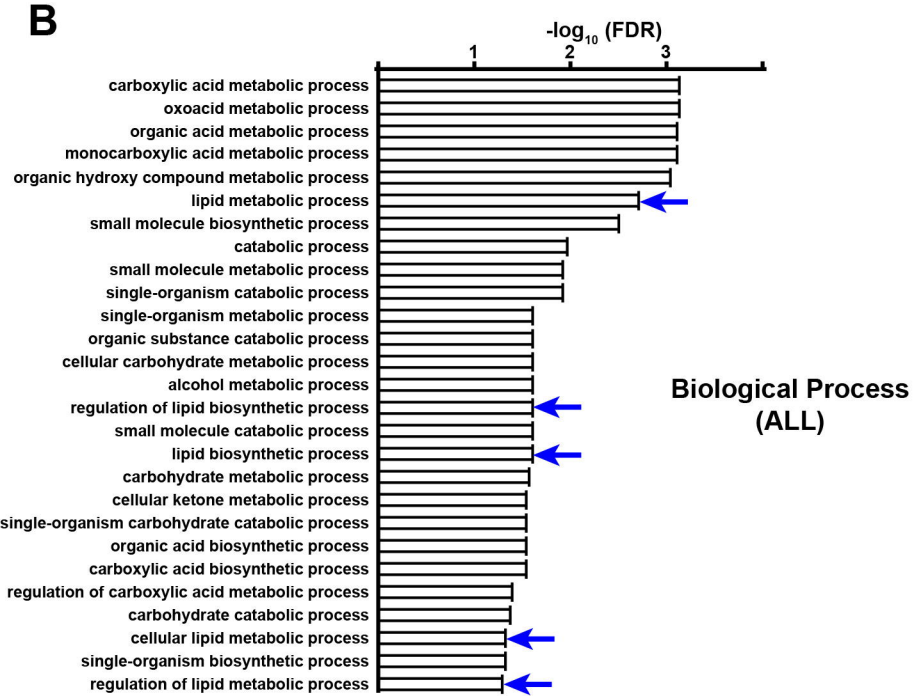

Figure 5 - figure supplement 3

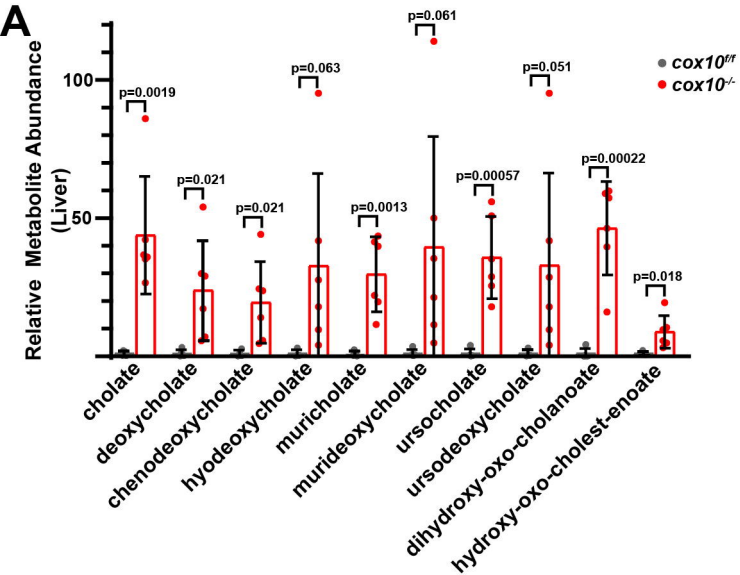

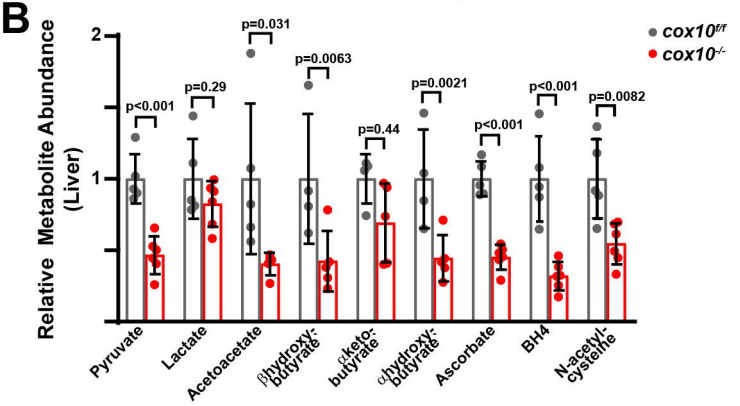

Figure 5 - figure supplement 4

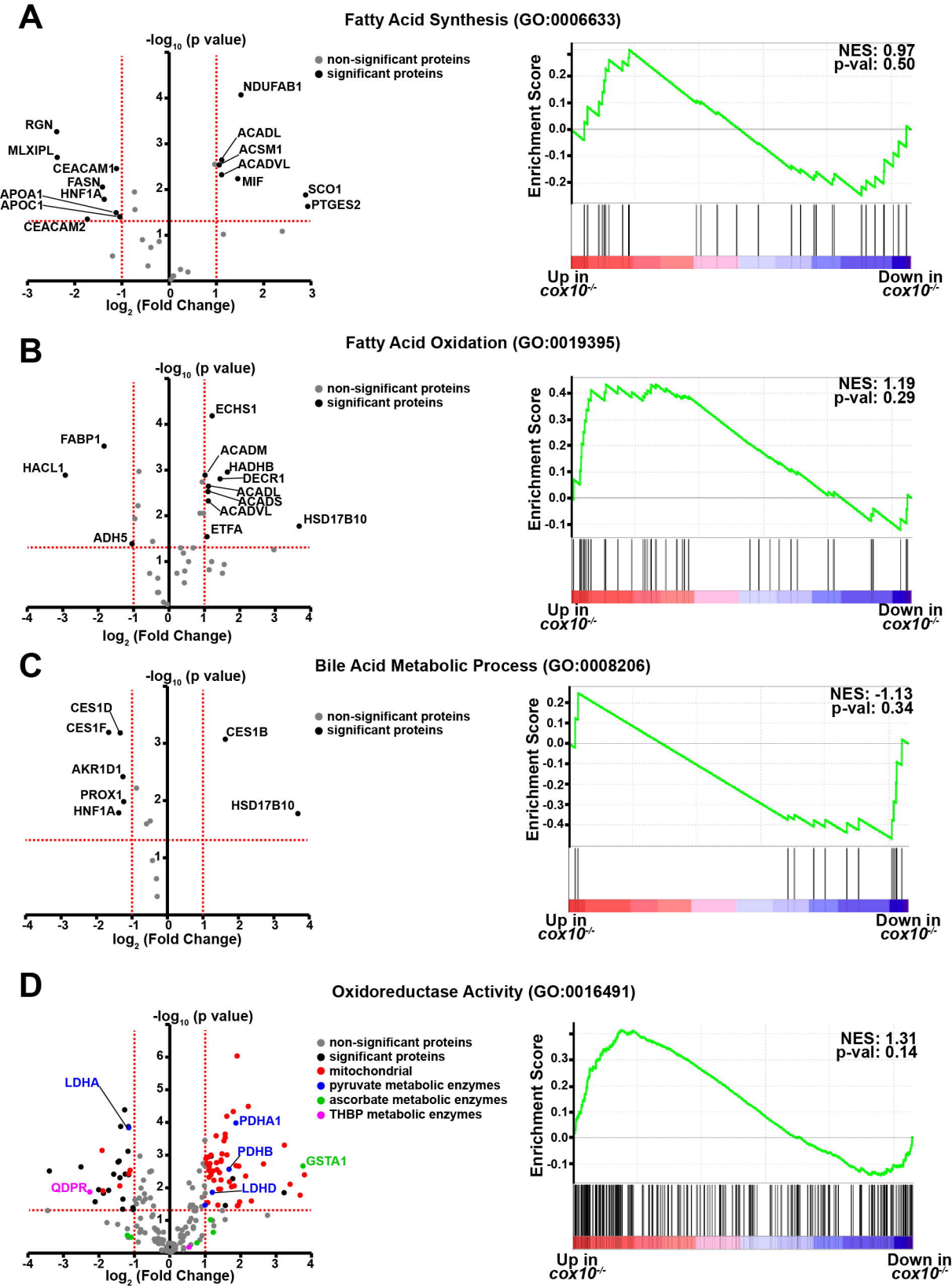

Figure 5 - figure supplement 5

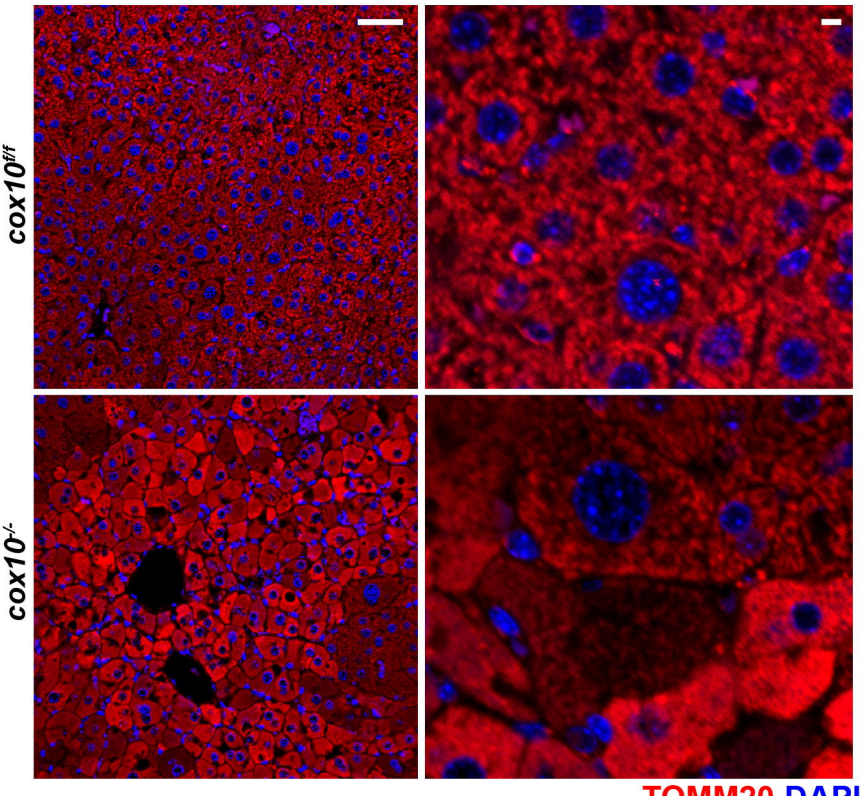
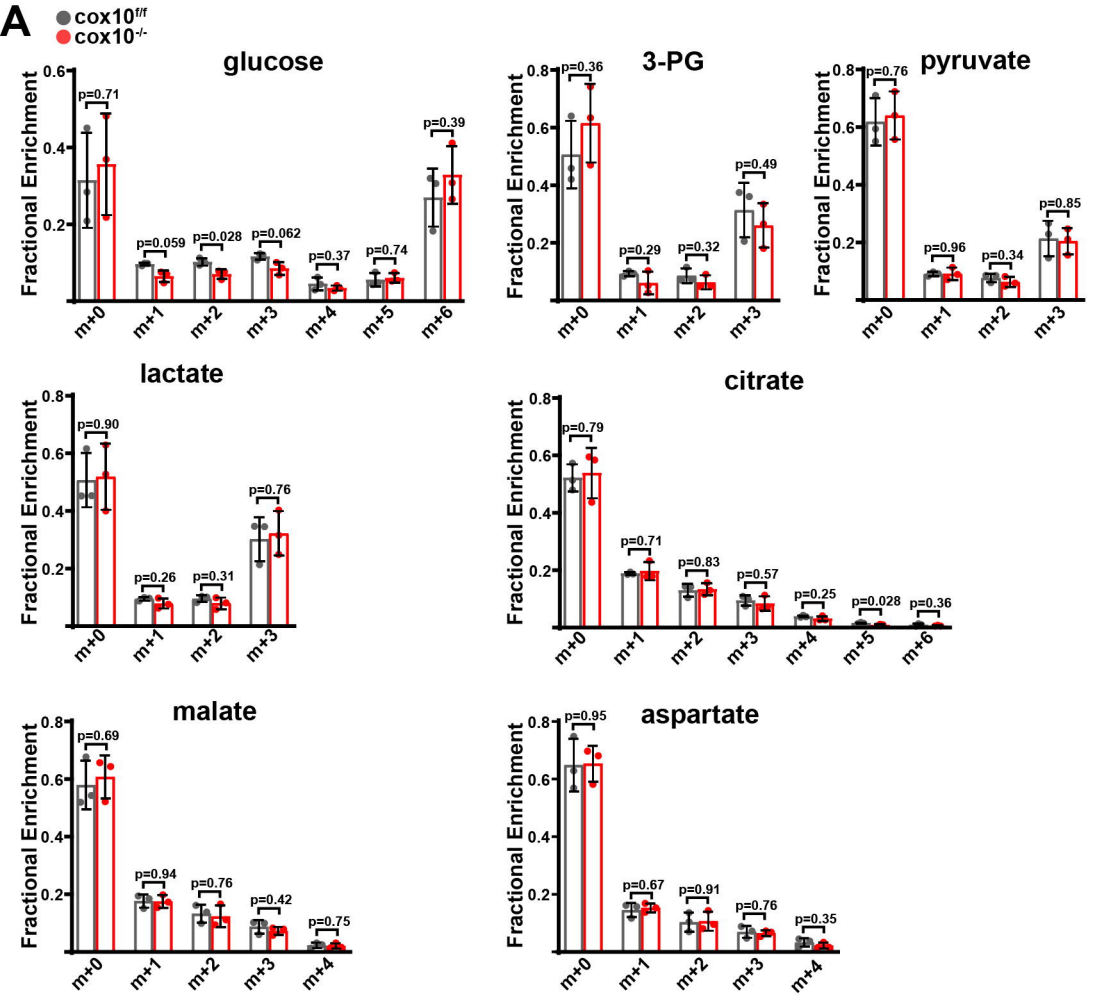
Figure 6 - figure supplement 1